

UNIVERSITY OF STIRLING

*Thesis  
2298*

ZAHOOR AHMAD SHEIKH

M.Sc. (PHYSICS), P. U. LAHORE, PAKISTAN

ATOMIC PHYSICS LABORATORY  
UNIVERSITY OF STIRLING, FK9 4LA, SCOTLAND.

MEASUREMENT OF THE COHERENCE LENGTH  
OF ATOMIC TWO-PHOTON RADIATION

SUBMITTED FOR THE DEGREE OF DOCTOR OF PHILOSOPHY



"MEASUREMENTS ARE THE ONLY WINDOWS,  
WE HAVE, THROUGH WHICH  
TO LOOK AT THE PHYSICAL WORLD"

(Niels Bohr)

06/9/88

#### ABSTRACT

We report a novel method of determining the coherence length of photons produced in the two-photon decay of metastable atomic deuterium by observing the depolarization of the photons in what is essentially a true single-photon interference experiment. In the Stirling source two photons propagating in the  $\pm z$  directions are detected in coincidence. The degree of polarization of the radiation emerging from a multiwave plate placed on one side of the source as a function of the optical path difference  $\delta$  introduced by the multiwave plate between the orthogonally polarized components is determined by measuring the Stokes' parameters. The results confirm the dependence of the depolarizing effect of the multiwave plate on  $\delta$ , agree with the quantum mechanical predictions and allow a measurement to be made of the coherence length of single photons of the two-photon pair.

We also report the results of an experiment which, for the first time, demonstrates the action of an achromatic half-wave plate on the polarization state of the two-photon radiation emitted by atomic deuterium in the metastable  $2S_{1/2}$  state. The results agree with the quantum mechanical predictions and confirm the hypothesis of Breit and Teller that the fine and hyperfine interaction play no role in the emission process.

#### ACKNOWLEDGEMENT

I want to gratefully acknowledge my supervisors Professor H.Kleinpoppen (FRSE) and Dr.A.J.Duncan (FRSE) for their suggestion of this project to me. I am highly indebted to Dr.A.J.Duncan for his constant encouragement and enthusiasm throughout the project and helping me to overcome many obstacles.

I also want to express my deep appreciation to Dr.H.J.Beyer and Dr.H.Hamdy who were always willing to discuss difficulties, and able to solve many of them.

The project could not have been brought to so successful a conclusion without the technical assistance of chief technician Mr.A.Sherman.

Finally, I am thankful to the Ministry of Education, Government of Pakistan and B.Z.University, Multan, Pakistan for granting me a scholarship and study leave to enable me to work for this project up to its successful completion.

## CONTENTS

	Page
Abstract	i
Acknowledgement	ii
Illustrations	ix
Preface	xiii
CHAPTER I	
REVIEW OF PRESENT AND PAST WORK	
1.1: Introduction	1
1.2: Copenhagen interpretation	4
1.2.1: <i>Uncertainty relations</i>	6
1.2.2: <i>Measurements and the collapse of the wavefunction</i>	7
1.3: Von Neumann's catastrophe	9
1.4: The Einstein-Podolsky-Rosen Paradox(EPR)	10
1.5: Bell's theorem	13
1.6: A brief survey of experimental work on Bell's inequality and the EPR paradox using an atomic source	18
1.6.1: <i>Cascade sources</i>	18
1.6.2: <i>Atomic Hydrogen two-photon source</i>	21
1.7: A brief survey of fourth order optical interference experiments using the two photon entangled state	22
1.7.1: <i>Single photon interference experiment</i>	22
1.7.2: <i>Fourth order interference experiments</i>	22
1.8: Proposed experiment	30

## CHAPTER II

## THEORY

2: Introduction	37
2.1: Theory of spontaneous radiation	39
2.1.1: <i>Two-photon radiation</i>	41
2.1.2: <i>Theory of two-photon transition</i>	43
2.2: State vector representation of two-photon pairs	46
2.3: Density matrix representation of the two-photon pair	49
2.4: Quantum mechanical description of analyzers	51
2.5: Relationship between density matrix and Stokes' parameters	54
2.6: Analysis of the polarization state vector of the emitted two-photon pair by two linear polarizers	57
2.7: Analysis of the two-photon polarization state vector modified by the insertion of an achromatic half wave plate	59
2.8: Retarders	61
2.8.1: <i>Matrix representation of a retarder</i>	64
2.8.2: <i>Relationship between the Stokes' parameters and the variable retardance <math>\phi</math> of a retarder</i>	65
2.8.3: <i>Attainment of variable retardance (non-achromatic)</i>	67
2.8.4: <i>Delay and Displacement of "e" and "o" ray wavepackets by a birefringent plate</i>	70

## CHAPTER III

## EXPERIMENTAL SET UP

3: Introduction	73
3.1:Description and operation of ion source	75
3.2:Caesium charge exchange cell	78
3.3:Vacuum system	80
3.4:Quenching arrangement	81
3.5:Neutral beam detector	82
3.6:Photomultiplier tube	83
3.6.1:Lyman alpha photomultiplier	84
3.7: Pile of plates polarizers	84
3.8: Transmittances of the linear polarizers	89
3.9: Retarders	91
3.10:Symmetrical optical system	91
3.11:System interlock	92
3.12:Coincidence electronics	93

## CHAPTER IV

## EXPERIMENTAL PROCEDURE AND TECHNIQUES

4: Introduction	96
4.1: Background radiation	96
4.2: Metastable atomic beam of deuterium	98
4.3: Beam analysis by a magnet	99
4.4: Alignment of the optical system	100

4.5: Coincidence technique	102
4.5.1: <i>Photon-photon coincidence</i>	102
4.6: Cosmic rays coincidence rate	104
4.6.1: <i>Pre-quench field method with beam present</i>	105
4.6.2: <i>Closing gate valve method</i>	106
4.7: Signal optimization	107
4.8: Measurement method	110
4.9: Normalization procedure	110
4.10: Choice of retarders	110
4.11: Procedure for checking the optic axis and retardation of a given retarder	127

## CHAPTER V

## MEASUREMENTS AND RESULTS

5. Introduction	133
5.1: Experiment using two linear polarizers and a two-photon pair from a metastable atomic deuterium	134
5.1.1: <i>Linear polarization correlation measurements</i>	134
5.1.2: <i>Circular polarization correlation measurements</i>	136
5.1.3: <i>Quantum mechanical prediction for the photon "2" seen by the polarizer A</i>	138
5.2: Experiment using two linear polarizers, an achromatic half-wave plate and a two-photon pair	141
5.2.1: <i>Measurements</i>	141

5.2.2: Quantum mechanical prediction for the modified two-photon polarization state vector produced by insertion of an achromatic half wave plate	144
5.2.3 Result	144
5.3: Experiment using two linear polarizers,a multi-order plate at $\lambda=694$ nm and a two-photon pair	146
5.4: Experiment using two linear polarizers,a multiwave plate(zero-order) and a two-photon pair	147
5.4.1: Measurements	149
5.4.2: Quantum mechanical prediction of the coherence length of two-photon radiation	154

## CHAPTER VI

DISCUSSION:	160
-------------	-----

## APPENDICES

A: Photon polarization	164
A.1: State vector of the photon polarization	167
B: Density operator	171
B.1: The concept of a statistical mixture	172
B.2: The density operator(pure case)	174
B.3: Description by a state vector	174
B.4: Description by a density operator	175
C: A statistical mixture of states(non-pure case)	180
C.1: Definition of the density operator	180

CONTENTS

C.2: General properties of the density operator	182
C.3: Populations:coherences	183
D: Polarization density matrices	185
E: Polarized light and Stokes' parameters	187
<b>REFERENCES</b>	<b>188</b>

## ILLUSTRATIONS

### CHAPTER I

Fig(1.1). Plot of  $|\cos\theta + \cos 2\theta| + \cos\theta$ . The dashed line is the upper limit set by Bell's inequality.

Fig.(1.2). Outline of the experimental set up.

Fig.(1.3). The measured number of coincidences as a function of beam-splitter displacement  $c\delta\tau$ , superimposed on the solid theoretical curve.

Fig.(1.4). A polarization interferometer using polarizing beam splitters.

Fig.(1.5). A polarization interferometer using a multiwave plate.

Fig.(1.6). Notional variation of degree of polarization with optical path difference.

### CHAPTER II

Fig(2.1). Level diagram for atomic deuterium, neglecting hyperfine structure (not to scale). The two photons, frequency  $\nu_1$  and  $\nu_2$ , can have any energy provided  $h\nu_1 + h\nu_2 = 10.2$  eV ( $h$  is Planck's constant).

Fig(2.2). Feynman diagrams for two-photon decay.

Fig(2.3). Bi-refringence ( $n_o, n_e$ ) analysis with respect to wavelength  $\lambda$ .

Fig(2.4). Minimum uncertainty packet representing a two-photon pair.

## CHAPTER III

- Fig(3.1). Schematic diagram of the apparatus.
- Fig(3.2). Ion source and power supplies.
- Fig(3.3). Cesium charge-exchange cell
- Fig(3.4). Reflection( $r$ ) and transmission( $t$ ) coefficients for the case of external reflection, with  $n = n_1/n_2 = 1.50$
- Fig(3.5). Reflectance for both external and internal reflection when  $n=1$  and  $n=1.50$ .
- Fig(3.6). Experimental set up for the calibration of the polarizer.
- Fig(3.7). Schematic diagram of the detection system.

## CHAPTER IV

- Fig(4.1). Mass analysis of the beam.
- Fig(4.2). Data acquisition for coincidence analysis.
- Fig(4.3). Variation of bi-refringence ( $n_o, n_e$ ) of quartz versus wavelength  $\lambda$ .
- Fig(4.4). Spectral distribution function  $A(\lambda)$  of two photons versus wavelength  $\lambda$ .
- Fig(4.5). The wavelength dependence of the transmission efficiencies  $\epsilon_{\parallel}$  and  $\epsilon_{\perp}$  for light polarized, respectively, parallel to and perpendicular to the transmission axes of the linear polarizers.
- Fig(4.6). Retardation analysis of HWP(quartz) of  $\lambda=200$  nm.
- Fig(4.7). Retardation analysis of HWP (quartz) of  $\lambda=243$  nm
- Fig(4.8). Retardation analysis of HWP(quartz) of  $\lambda =300$  nm.
- Fig(4.9). Retardation analysis of HWP (quartz) of  $\lambda = 486$  nm.

Fig.(4.10). Graphical determination of wavelength at which half-wave plate will act as quarter-wave plate.

Fig.(4.11). Experimental set up for checking the optic axis of a given retarder.

Fig.(4.12). Experimental set up for measuring the retardation of a given retarder.

## CHAPTER V

Fig.(5.1). A typical experimental arrangement used for two-photon polarization correlation measurements  $D_1$  and  $D_2$  are photomultipliers.

Fig.(5.2). Schematic diagram of the typical ideal experimental arrangement using two linear polarizers A & B, two detectors  $D_1$  and  $D_2$ . The transmission axis of the polarizer B is rotated through angles  $\theta$  while that of A is oriented vertical parallel to the x-axis. The fast axis of the  $\lambda/4$  plate is set at  $\pm 45^\circ$  relative to the x-axis to obtain left-hand and right-hand circular polarization.

Fig.(5.3). Schematic diagram of the typical ideal experimental arrangement using two linear polarizers A & B, two detectors  $D_1$  and  $D_2$ . The transmission axis of the polarizer B is rotated through angle  $\theta$  while that of A is oriented vertical parallel to the x-axis. The fast axis of the  $\lambda/2$  plate is set at  $45^\circ$  relative to the x-axis.

Fig.(5.4). Schematic diagram of the typical ideal experimental arrangement using two linear polarizers A & B, two detectors  $D_1$  and  $D_2$ . The transmission axis of the polarizer B is rotated through angles  $\theta$  while that of A is oriented vertical parallel to the x-axis. The fast axis of the  $\lambda/2$  plate is set at  $45^\circ$  relative

to the x-axis. The fast axis of the  $\lambda/4$  plate is set at  $\pm 45^\circ$  relative to the x-axis to obtain left-hand and right-hand circular polarization.

Fig.(5.5). Schematic diagram of the typical ideal experimental arrangement using two linear polarizers A & B, two detectors  $D_1$  and  $D_2$ . The transmission axis of the polarizer B is rotated through angle  $\theta$  while that of A is oriented vertical parallel to the x-axis. The fast axis of the  $\lambda/2$  plate (multiwave) is set at  $45^\circ$  relative to the x-axis.

Fig.(5.6). Schematic diagram of the typical ideal experimental arrangement using two linear polarizers A & B, two detectors  $D_1$  and  $D_2$ . The transmission axis of the polarizer B is rotated through angle  $\theta$  while that of A is oriented vertical parallel to the x-axis. The fast axis of the  $\lambda/2$  plate (multiwave) is set at  $45^\circ$  relative to the x-axis. The fast axis of the  $\lambda/4$  plate is set at  $\pm 45^\circ$  relative to the x-axis to obtain left-hand and right-hand circular polarization.

Fig.(5.7). Variation of the Stokes' parameter  $P_1$  with respect to relative displacement of wave packet  $\delta$ .

Fig.(5.8). Variation of the Stokes' parameter  $P_2$  with respect to relative displacement of wave packet  $\delta$ .

Fig.(5.9). Variation of total Polarization with respect to relative displacement of wave packet  $\delta$ .

## PREFACE

Hydrogen was news. Hydrogen is news and it will be news in future too. The reason, surely, is that the apparent simplicity of the hydrogen atom invites meticulous scrutiny of its very depths, yet these depths are sufficiently impenetrable to present a challenge both for the exercise of the unbelievably sharp experimental tools which are now in use and being contemplated, and for the exercise of the enormous computing power now available to theorists<sup>1</sup>. Our experiment also uses hydrogen, in practice deuterium as an experimental tool to study the polarization correlation properties of two photons emitted simultaneously during the decay of metastable atomic hydrogen. The aim of this new experiment is to resolve the controversy surrounding the correct coherence length to be associated with these photons and in the process to allow, in a novel way the measurement of the coherence length of photons using a method in which one of the photons is deliberately depolarized.

---

<sup>1</sup>Extracts from "The Spectrum of Atomic Hydrogen:ADVANCES" edited by G.W.Series(world Scientific).Oxford university press 1988.

## CHAPTER 1

### REVIEW OF PRESENT AND PAST WORK

#### §1.1: INTRODUCTION

Niels Bohr once remarked that anybody who is not shocked by quantum theory has not understood it. Certainly a powerful sense of shock and bewilderment reverberated among his contemporaries in the 1920's when the full implications of the theory began to emerge. Not only did quantum theory fly in the face of classical physics but it also radically transformed scientists' outlook on our relationship with the material world. For, according to Bohr's interpretation of the theory, the existence of the world 'out there' is not something that enjoys an independence of its own, but is inextricably tied up with our perception of it.

Having played a significant part in the early development of quantum theory, Albert Einstein became its foremost critic. In 1912, Einstein wrote to a friend, "the more success the quantum theory has, the sillier it looks"[1]. Albert Einstein's comment that "God does not play dice" summed up the way many people reacted when they first encountered the ideas of the Copenhagen interpretation (discussed in §1.2). How can it be that future events are not completely determined by the way things are at present? How can a cause have two or more possible effects? If the choice of future events is not determined by natural laws, does it mean that some supernatural force (God?) is involved whenever a quantum event occurs. Until his death, he was

convinced that an essential ingredient was missing from the formulation of quantum theory; without this ingredient, he argued, our description of matter on the atomic scale would inevitably remain intrinsically uncertain and therefore incomplete. To demonstrate the incompleteness of quantum theory, he produced a number of highly ingenious arguments, some of which (especially the EPR experiment described in §1.4) caused considerable concern among scientists. But each time Bohr quickly managed to find an elegant and persuasive refutation.

The traditional interpretation of quantum mechanical formalism is usually known as the Copenhagen interpretation. Because this interpretation provides us with only probabilistic information about the state of a quantum-mechanical system, and because this interpretation has some weird aspects that go counter to our intuition, its adequacy has often been challenged.

Critics of the Copenhagen interpretation do not challenge the accuracy of the numerical results calculated from quantum mechanics. At a pragmatic level, quantum mechanics works perfectly—the numerical results for, say, the eigenvalues of the angular momentum and energy of the hydrogen atom are found to be in perfect agreement with experiment. But critics challenge whether the Copenhagen interpretation really gives us the most complete, most exhaustive knowledge of a quantum system we can hope for. For instance, is it really impossible to say anything about the precise instantaneous position of the electron in the hydrogen atom and its motion as a function of time? Or is the inability of quantum mechanics to provide this information an

indication of some deficiency of the theory?. In the view of some critics the probabilistic character of the predictions of quantum mechanics is held to reflect our ignorance of the details of the underlying dynamics. Theories that attempt to provide a more detailed knowledge than provided by the Copenhagen interpretation are said to contain hidden variables.

The discussion of the interpretation of quantum mechanics and of hidden-variables theories has received a fresh stimulus in recent years, because it has become possible to perform an experiment originally conceived as a Gedanken experiment by Einstein, Podolsky and Rosen in 1935[2].

A new theoretical analysis of this Gedanken experiment by Bell in 1964 established that it could be used to discriminate between the Copenhagen interpretation and a wide class of theories with hidden variables, and this encouraged experimenters to attempt some actual version of the experiment. The experimental results fully support the Copenhagen interpretation and contradict theories with hidden variables. Our present experiment (described in chapter III) is in the direction of the above mentioned attempts and fully qualifies as a litmus test of the violation of Bell's inequality (discussed in §1.5).

## §1.2: COPENHAGEN INTERPRETATION

The main features of the Copenhagen interpretation can be summarized as follows:

- The state vector  $|\psi\rangle$  provides a complete characterization of the state of the system.
- The state vector tells us the probability amplitude for the result of the measurement of any observable quantity. This probability amplitude applies to each individual quantum particle or quantum system.
- The uncertainty relations indicate the intrinsic spreads in the values of complementary observables for the individual quantum particle or quantum system. These uncertainty relations deny the existence of sharp values of complementary observables.
- Measurements produce unpredictable, discontinuous changes in the state vector which do not obey the Schrödinger equation. The outcome of a single measurement of an observable is unpredictable — the outcome can be any of the eigenvalues within the spread of the probability distribution. During the measurement, the state of the system collapses into an eigenstate of the observable.

The quantum-mechanical wavefunction makes no assertion about the instantaneous position of the electron or about the instantaneous charge distribution in the atom. It merely provides us with the means of calculating expectation values e.g. the expectation value of energy.

$$H\psi = E\psi$$

(1-1)

where  $H$  is the energy operator.

Quantum mechanics does not supply us with a concrete mental picture of the behaviour of atoms and subatomic particles. It does not tell us what atoms and subatomic particles are like; it merely tells us what happens when we perform measurements. As Heisenberg[3] said; "The conception of objective reality---- evaporated into the ----mathematics that represents no longer the behaviour of elementary particles but rather our knowledge of this behaviour."

According to the Copenhagen interpretation the only meaningful quantities are those that are measurable.

In classical statistical mechanics the probability distribution for molecular speeds in a gas reflects the ignorance of the observer of the precise microscopic conditions. This kind of probability distribution is called the ENSEMBLE distribution, since it describes the average conditions for a large number of molecules of a gas. In contrast, the quantum mechanical probability distribution does not reflect our ignorance of the instantaneous position and momentum, but rather the non-existence of any well defined position and momentum. The quantum-mechanical system does not consist of particles with well-defined albeit unknown positions and momenta, but of "particles" with intrinsically indeterminate positions and momenta. **Thus the Q.Mechanical probability distribution refers to an individual particle, not to an ensemble**

of particles.

### 1.2.1: Uncertainty relations:

For complementary observables, such as the position  $x$  and the momentum  $p_x$ , whose commutator has the canonical form  $[x, p_x] = i\hbar$ , there are no simultaneous eigenvectors, and the certainty in one of these observables implies total uncertainty in the other in accord with the Heisenberg uncertainty relations

$$\Delta x \Delta p_x \geq \hbar/2. \quad (1-2)$$

The uncertainties  $\Delta x$ ,  $\Delta p_x$ , and other such quantum-mechanical uncertainties refer to an individual particle, not to an ensemble of particles. These quantum mechanical uncertainties do not arise from our ignorance of some underlying details of the state of the particle or from inadequacy of our measuring devices. Instead, the uncertainties reflect the non-existence of such details; they reflect an intrinsic spread in the position and the momentum of the particle. The position and momentum are not sharply defined, they are indeterminate.

The Heisenberg uncertainty relation for the position and momentum of a particle implies that classical determinism fails since the initial values of the position and the momentum of a particle cannot be used to predict the position and momentum at a later time. In general, the future behaviour of a physical system cannot be predicted however accurately the present state is known. However, although quantum mechanics lacks the simple determinism of classical physics, it retains a form of determinism in the state vector  $|\psi\rangle$ , which evolves in time according to the (general) Schrödinger

equation

$$\frac{\hbar}{i} \frac{d}{dt} |\psi\rangle = H |\psi\rangle.$$

(1-3)

This equation expresses determinism and causality, since it permits us to predict the state vector at any later time from a given state vector at the initial time. Thus in the words of Born[4]: "The motion of particles is subject [only] to probabilistic laws, but the probability itself evolves in accord with causal laws".

### 1.2.2: Measurements and the collapse of the wavefunction

The Copenhagen interpretation requires that the wavefunction suffers a discontinuous, unpredictable change during the measurement. Consider, for instance, the impact of an electron on the fluorescent screen in an electron-diffraction experiment. The flash of light released by this impact constitutes an approximate measurement of the position of the electron. Just before this measurement, the wavefunction was spread out all over the screen; immediately after the measurement, the electron position is known to lie within some small spot on the screen and the wavefunction must therefore have an extent no greater than this spot. Thus, during the measurement, the wavefunction suffers an unpredictable collapse or reduction. The collapse is unpredictable, since we have no way of knowing on to what part of the screen the wavefunction will collapse — we know only the probability distribution of positions for the electron on the screen.

In general, a precise measurement of an observable collapses the wavefunction into an eigenstate of that observable. A measurement of the energy of an electron collapses the wavefunction into an eigenstate of energy. A measurement of the spin collapses the wavefunction into an eigenstate of spin, and so on. The apparatus plays a crucial role in selecting the kind of eigenstate into which the wavefunction collapses. The apparatus dictates whether the system will collapse into some eigenstate of position, or of momentum, or of spin. But, of course, the apparatus does not dictate which specific eigenstate of position, or of energy or of spin, the system will collapse into; this aspect of the collapse is unpredictable.

Bohr has emphasised that quantum mechanics does not describe quantum systems per se, instead it describes a whole phenomenon, which includes, in an inextricable way, both the quantum system and the apparatus to measure it:[5] "—an independent reality in the ordinary physical sense can neither be ascribed to the phenomenon nor to the agencies of observation." According to the Copenhagen interpretation, the quantum systems in themselves do not have sharply defined attributes only diffused potentialities, which are capable of being sharply defined when we perform suitable measurements. The attributes of a quantum system depend on the apparatus used to measure them and they exist only in relation to this apparatus. **Thus, the attributes are a joint property of the system and the apparatus.** The Copenhagen interpretation extends only to the attributes of the physical system, not to the physical systems themselves. It boldly postulates that the

collapse of the wavefunction is merely a mathematical procedure, not a physical process.

The theoretical evolution of the joint system-apparatus state vector has been examined in detail by Bohr [5] in relation to the measurement of the vertical component of the spin of an atom with the Stern-Gerlach apparatus, and it has been seen that, as long as the atom, the apparatus and their interaction are governed by the Schrödinger equation, a collapse of the state vector is not possible. This raises the question as to when or under what circumstances a collapse of the state vector is possible.

### §1.3: VON NEUMANN'S CATASTROPHE

The absence of collapse in any system governed by the Schrödinger equation—and the concomitant impossibility of bringing a measurement to completion, no matter how many apparatus are stacked one on top of another—is called the Von Neumann's catastrophe of infinite regression. This absence of collapse was established by Von Neumann, who made the first rigorous examination of the mathematical foundation of quantum mechanics. Von Neumann decided that the collapse of the state vector during measurement must be inserted into quantum mechanics as a separate axiom. "If we arrange any number of apparatus in a sequential stack, in which each apparatus checks on the apparatus ranking below it, we must postulate that the collapse of the state vector occurs somewhere in this stack."

**§1.4: THE EINSTEIN—PODOLSKY—ROSEN PARADOX (EPR)**

As said earlier in §1.2, Einstein challenged the completeness assumption of the Copenhagen interpretation by a variety of clever Gedanken experiments. At first, the thrust of these was directed at the uncertainty relations, by contriving some measurement procedure that would simultaneously determine the co-ordinate and momentum of a particle. One such Gedanken experiment proposed by Einstein in a discussion with Bohr at the 1928 Solvay meeting was based on discussion of the momentum exchange between the incident particle and a slotted plate. He proposed to measure the momentum by the recoil suffered by the plate. He suggested that the plate be loosely suspended (by the springs) so it can move and its recoil motion can be determined. Since the recoil momentum of the plate, which is a large macroscopic body for which the laws of classical mechanics ought to hold, can presumably be measured with arbitrary precision, it should be possible to violate the uncertainty relations. But Bohr was quick to notice that the plate is itself subject to the uncertainty principle and hence refuted the argument of Einstein. Blocked in his direct attacks on the uncertainty relations, Einstein, in a joint venture with Podolsky and Rosen[2] launched a more subtle attack on the completeness assumptions on which the uncertainty relations are based.

The EPR paradox, begins with the hypothesis that the quantum mechanical predictions for the results are correct and tries to show, by means of a Gedanken experiment, **that the quantum mechanical description of the state of the system is incomplete, that is, the system is endowed with**

**physical properties that go beyond those permitted by quantum mechanics.** The EPR paradox examines the joint quantum-mechanical state of two particles that are initially correlated in such perfect way that a measurement performed on one of the particles immediately tells us the state of the other particle, without any need to measure or disturb this other particle.

According to Bohm, the EPR paradox can be stated in terms of two particles of spin  $\frac{1}{2}$  in a state of net spin zero, that is, in a state in which their spins are opposite. Suppose that the particles are initially close together, but then they move apart to a large distance, while they remain in the original state of net spin zero. Once they are widely separated we measure the spin of one of these particles. Since the net spin is zero, the measurement of the spin of the first particle immediately allows us to infer the spin of the other particle— it must always be opposite to the spin of the first particle.

The crucial step in the argument of the EPR paradox is this: since our measurement did not affect this second particle, its state before the measurement ought to be the same as after, and therefore this second particle must have had a well defined spin ( $z$ -component) before we performed the measurement. The same argument can be extended to measure components of spin of the second particle in any direction. Thus, all of the components of the spin of the 2nd particle ought to be well defined, in contradiction to quantum mechanics, which asserts that if one component is well defined, then the others are indeterminate. Accordingly, EPR claimed that the quantum mechanical description provided by the state vector cannot be complete. In

their view, the state vector must be supplemented or replaced by some extra "hidden variables".

**The EPR argument hinges on the reality of the attributes of the particles and on the locality of the measurement procedure.** The spin of the second particle is supposed to exist, in itself, even if we do not measure it; and the measurement performed on the first particle is supposed to produce no effect on the second, distant particle. Quantum mechanics refutes this paradox by denying both of these suppositions. **The Copenhagen interpretation tells us that the particles do not have attributes in themselves, but only in relation to a measurement procedure. Furthermore, it tells us that a measurement procedure on one portion of a wavefunction, at one place, affects the entire wavefunction, even its very distant portions.** According to quantum mechanics, the state vectors of the two particles are so intimately intertwined that it makes no sense to speak of the state vector of each individual particle. The particles are in an **entangled state**

The expression for the eigenstate of net spin zero ( $s=0, m_s=0$ ) formed from two states of spin  $\frac{1}{2}$  can be written as

$$|0, 0\rangle = \frac{1}{\sqrt{2}} (|+\rangle|-\rangle - |-\rangle|+\rangle) .$$

(1-4)

Here, the first ket in each term indicates the spin state of the first particle, and the second ket that of the second. For each individual particle, this state  $|0,0\rangle$  is neither an eigenstate of the individual z-component of spin, nor even a

simple superposition of eigenstates  $|\uparrow\rangle|\downarrow\rangle$ ). There is no definite state vector for the incident particle — only a joint state vector for the system. Thus it is not surprising that a measurement of the spin of one particle affects the other particle. The measurement of the spin of one particle changes the whole state.

Although quantum mechanics gives a perfectly logical answer to the EPR paradox, it does not give an answer that satisfies our intuition. Quantum mechanics asks us to ignore our intuition and to accept the weird intertwined non-local behaviour of the particles in this Gedanken experiment.

### §1.5: BELL'S THEOREM

Einstein and other physicists who favoured the existence of hidden variables took it for granted that the predictions of quantum mechanics could be duplicated by adopting some sufficiently large set of hidden variables with a sufficiently complicated ensemble distribution. However, in 1964, Bell[6] demonstrated that not all of the subtleties of the probabilistic predictions of quantum mechanics can be duplicated by hidden variables. He demonstrated that the correlations among spin measurements on two particles of spin  $\frac{1}{2}$  in a state of zero net spin can not be duplicated by local hidden variables.

If  $\mathbf{a}$  and  $\mathbf{b}$  are the two unit vectors in different directions along which the spin of the two particles, referred to in section §1.4, can be measured, then the CORRELATION COEFFICIENT  $C(\mathbf{a}, \mathbf{b})$  is defined as the average value of the product  $(\hbar/\hbar)S_{a1} S_{b2}$ :

$$C(\mathbf{a}, \mathbf{b}) = \frac{4}{\hbar^2} [S_{\mathbf{a}_1} S_{\mathbf{b}_2}]_{\mathbf{a}, \mathbf{b}} \quad (1-5)$$

where,

$S_{\mathbf{a}_1}$  = spin component of particle 1 along  $\mathbf{a} = \pm \hbar/2$

$S_{\mathbf{b}_2}$  = spin component of particle 2 along  $\mathbf{b} = \pm \hbar/2$

If the directions  $\mathbf{a}$  and  $\mathbf{b}$  are the same, measurements on the quantum mechanical spin state exhibit a perfect correlation, or rather, a perfect anticorrelation.

For each paired spin measurement, the value of  $(4/\hbar^2) S_{\mathbf{a}_1} S_{\mathbf{b}_2}$  is either +1 or -1; hence  $C(\mathbf{a}, \mathbf{b})$  is the average of a sequence of +1's and -1's and necessarily falls within the range

$$-1 \leq C(\mathbf{a}, \mathbf{b}) \leq +1 \quad (1-6)$$

If for each paired spin measurement, the observed values of  $S_{\mathbf{a}_1}$  and  $S_{\mathbf{b}_2}$  are exactly opposite, then

$$C(\mathbf{a}, \mathbf{b}) = \frac{4}{\hbar^2} S_{\mathbf{a}_1} S_{\mathbf{b}_2} = \frac{4}{\hbar^2} \left( +\frac{\hbar}{2} \right) \left( -\frac{\hbar}{2} \right) = -1 \quad (1-7)$$

this characterizes a perfect anticorrelation.

If for each paired spin measurement, the observed values of  $S_{\mathbf{a}_1}$  and  $S_{\mathbf{b}_2}$  are exactly the same, then  $C(\mathbf{a}, \mathbf{b}) = +1$ , a perfect correlation.

The  $C(\mathbf{a}, \mathbf{b})$  will fall between extreme values +1 and -1 if some pairs of measurement yield opposite spins and some pairs equal spins.

In quantum mechanics, over a long sequence of repeated measurements,  $C(\mathbf{a}, \mathbf{b})$  is predicted to be given by

$$C(\mathbf{a}, \mathbf{b}) = \left( \frac{4}{\hbar^2} S_{\mathbf{a}} S_{\mathbf{b}} \right) = \cos \theta \quad (1-8)$$

where  $\theta$  is the angle between the directions of  $\mathbf{a}$  and  $\mathbf{b}$ .

For  $\theta=0^\circ$ ,  $C(\mathbf{a}, \mathbf{b}) = -1$ ,  $\theta=180^\circ$ ,  $C(\mathbf{a}, \mathbf{b}) = +1$  as expected.

For  $\theta=90^\circ$ ,  $C(\mathbf{a}, \mathbf{b}) = 0$  since the second spin is always opposite the first, and therefore has equal probabilities for the two possible eigenstates ( $S_{z_2} = \pm \hbar/2$ ) of spin at right angles; consequently, there is no correlation between  $S_{z_2}$  and  $S_{z_1}$ . Eq.(1-8) can be derived by assuming that  $\mathbf{a}$  is along  $+z$ -axis and  $\mathbf{b}$  is in the  $z$ - $x$  plane at an angle  $\theta$  with  $x$ -axis.

The eigenstate for the zero spin state is

$$|0, 0\rangle = \frac{1}{\sqrt{2}} (|+\rangle|-\rangle - |-\rangle|+\rangle) \quad (1-9)$$

Since  $C(\mathbf{a}, \mathbf{b})$  is the expectation value of  $4/\hbar^2 S_{z_1} S_{z_2}$ , therefore

$$C(\mathbf{a}, \mathbf{b}) = \langle 0, 0 | \frac{4}{\hbar^2} S_{z_1} S_{z_2} | 0, 0 \rangle \quad (1-10)$$

Expressing  $S_{z_2}$  as a superposition of  $S_{z_1}$  and  $S_{z_2}$  and then simplifying, eq.(1-10) reduces to eq.(1-8).

Bell examined the correlation coefficients for measurements of the spin

components along three(or more) different directions. **He proved that in any local hidden-variable theory, the correlation coefficients are restricted by an inequality and this inequality is not satisfied by the correlation coefficient predicted by quantum mechanics.**

Consider three different directions specified by the unit vectors  $\mathbf{a}, \mathbf{b}, \mathbf{c}$  and suppose that we perform paired measurements of the spin components of the two particles along these directions, taking two directions at a time. We begin with a sequence of paired measurements along the directions  $\mathbf{a}$  (for particle 1) and  $\mathbf{b}$  (for particle 2); then a sequence of measurements along the directions  $\mathbf{a}$  and  $\mathbf{c}$ ; and finally a sequence of measurements along the directions  $\mathbf{b}$  and  $\mathbf{c}$ . The correlation coefficients for sequences of measurements are  $C(\mathbf{a}, \mathbf{b})$ ,  $C(\mathbf{a}, \mathbf{c})$ ,  $C(\mathbf{b}, \mathbf{c})$ , respectively.

According to hidden variable theory, the predicted values of these correlations are ensemble averages over the hidden variables. But Bell proved that in any local hidden variable theory, the correlation coefficients necessarily obey the inequality

$$\eta = |C(\mathbf{a}, \mathbf{b}) - C(\mathbf{a}, \mathbf{c})| - C(\mathbf{b}, \mathbf{c}) \leq 1 \quad (1-11)$$

This result, known as BELL'S THEOREM, is independent of the details of hidden variable theory. The inequality eq.(1-11), called BELL'S INEQUALITY, is obeyed by every local hidden variable theory. **But this inequality is not obeyed by quantum mechanics.**

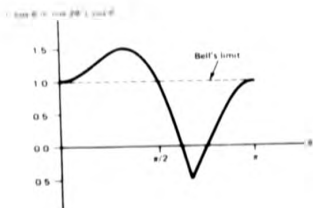
For the sake of simplicity, let us consider the special case with  $a, b, c$  in the same plane, say, the  $z$ - $x$  plane and with  $a$  along the  $+z$ -axis,  $b$  at an angle  $\theta$  with respect to  $+z$  axis, and let,  $c$  be at angle of  $2\theta$  w.r.t the  $+z$ -axis. The quantum mechanical correlation coefficients are then given by (using eq (1-8))

$$C(a,b) = -\cos\theta, C(a,c) = -\cos 2\theta, C(b,c) = -\cos\theta \quad (1-12)$$

Thus the quantum-mechanical expression for the left side of the inequality eq (1-11) is

$$C(a,b) - C(a,c) + C(b,c) = -\cos\theta + \cos 2\theta + \cos\theta$$

(1-13)



Fig(1.1) Plot of  $-\cos\theta + \cos 2\theta + \cos\theta$ . The dashed line is the upper limit set by Bell's inequality

Fig.(1.1) shows a plot of this expression as a function of  $\theta$ . We see that in the interval  $0 < \theta < \pi/2$ , the quantum-mechanical result is inconsistent with all local hidden-variable theories.

Bell's inequality eq.(1-11) provides us with a way to discriminate experimentally between the predictions of quantum mechanics and those of local hidden variables theories. Before Bell's theorem, such a discrimination was thought to be impossible, since hidden-variable theories are designed to mimic the results of quantum mechanics as best they can.

### §1.6: A BRIEF SURVEY OF EXPERIMENTAL WORK ON BELL'S INEQUALITY AND THE EPR PARADOX USING AN ATOMIC SOURCE.

#### 1.6.1: CASCADE SOURCES

The early measurements [7] of the linear polarization correlation of the two photons produced in the annihilation of para-positronium gave the interest to study the polarization correlation of photon. These measurements were carried out as a result of a suggestion by Wheeler [8] that these photons, when detected, have orthogonal polarization. But it was pointed out by Yang [9] that these measurements only gave the information on the parity state of nuclear particles that decay into two photons. The main stimulus to the performance of polarization correlation measurements came first from the Gedankenexperiment of Bohm [10] and the paper of Bohm and Aharonov [11] in which the so-called paradox of Einstein, Podolsky, and Rosen (EPR) [2] was put in terms of the polarization of photons and subsequently from the work

of Bell.

The original analysis of Bell assumed ideal systems and therefore could not be tested in a real experimental situation. Such a test, however, was made possible by Clauser, Horne, Shimony, Holt [12] and Clauser and Horne [13]. They made the crucial assumption that the photons that are detected have the same properties as those that are not detected. This assumption known as no-enhancement hypothesis, was experimentally tested by T.Haji-Hassan et al [14] and found to be valid.

According to Bohm(1951) [10] both the experimental measurements and theoretical predictions about particle spin are practically identical to those relating to photon polarization. Inequalities similar to Bell's inequality were derived for the correlation of the polarization of paired photons of net spin zero emitted by an atom. Essentially the inequality, eq.(1-11), was also derived by Clauser, Horne, Shimony and Holt [12] and it is sometime referred to as the Bell, Clauser, Horne, Shimony, and Holt(BCHSH) inequality. Its importance lies in the fact that it represents a general restriction on the predictions of theories based on local realism. The BCHSH inequality  $\eta$ , defined in [12], is given by

$$-1 \leq \eta \leq 0 \quad (1-14)$$

A number of experiments [15-23] have been conducted in an attempt to compare the quantum mechanical prediction for correlation coefficients with those predicted by the hidden variable theories. Most of these experiments studied the correlations of the polarizations of paired photons of net spin zero

emitted by an atom. The pairs of photons used in experimental tests of Bell's inequality are emitted in a cascade process in which an atom quickly makes two transitions from an upper state of  $j=0$ , to an intermediate state of  $j=1$ , and finally to a lower state of  $j=0$ . Since the initial and final states have angular momenta zero, the net angular momentum carried away by the two photons emitted in these two transitions must be zero, and their polarizations are therefore perfectly correlated.

The various experiments that have been carried out differ mainly in their choice of source and type of polarizers used. Because of the angular correlation of the photon pairs emitted in the two photon decay processes from an atom, the finite solid angle of detection, and the low detection efficiency of the photodetectors in practice, only a very small portion of the photon pairs emitted by the source is actually detected.

With one exception [17], attributed to systematic experimental error or possibly some other effects due to the use of a calcite polarizer, all these experiments found a correlation that agreed with the prediction of quantum mechanics and that exceeded the upper limit demanded by Bell's inequality. The inequalities tested in these experiments actually were in the BCHSH forms [12] and its simplified version given by Freedman [16].

The most successful of the above mentioned experiments was reported by A. Aspect, J. Dalibard and G. Roger [23]. The experimental results exceeded the Bell's limit by more than 40 standard deviations. Experimentally, it was found that

$$\eta = 0.101 \pm 0.020$$

in violation of Bell's inequalities for which  $-1 \leq \eta \leq 0$ , on the other hand, taking into account the solid angle of detection and the efficiencies of the polarizers, gave the quantum mechanical prediction

$$\eta_{QM} = 0.112$$

Fig(5.1) in chap.V typifies the experimental arrangement for these experiments.

### 1.6.2: ATOMIC HYDROGEN TWO-PHOTON SOURCE

Perrie, Duncan, Beyer, and Kleinpopp[24] measured for the first time the polarization correlation of the two photons emitted simultaneously by metastable atomic deuterium in a true second-order decay process and used the results to test the BCHSH inequality. Single-photon decay from the  $2S_{1/2}$  state of deuterium is forbidden and, as illustrated in Fig.(2.1), in chap.II, the main channel for the spontaneous deexcitation of this state is by the emission of two photons, which can have any wavelength consistent with conservation of energy for the pair, the most probable occurrence being the emission of two photons each of wavelength 243 nm. Since the decay proceeds through virtual intermediate states, the effects of hyperfine structure can be neglected, and hence the angular and polarization correlations are predicted to be identical to those resulting from a 0-1-0 cascade in an atom with zero nuclear spin.

The results of measurements clearly agree with the quantum mechanical prediction. In addition, using the results at  $22.5^\circ$  and  $67.5^\circ$  gave  $\eta = 0.268 \pm 0.010$ , in violation of the BCHSH inequality but in agreement with the quantum mechanical result  $\eta_{QM} = 0.272 \pm 0.008$ .

## §1.7: A BRIEF SURVEY OF FOURTH ORDER OPTICAL INTERFERENCE EXPERIMENTS USING THE TWO-PHOTON ENTANGLED STATE

### 1.7.1: SINGLE PHOTON INTERFERENCE EXPERIMENT

By using a two-photon radiative cascade described elsewhere [20], emitting pairs of photons with different frequencies  $\nu_1$  and  $\nu_2$ , and a triggered detection scheme for the second photon of the cascade, P. Grangier et al [25] successfully demonstrated the strong anti-correlation between the triggered detection on both sides of a beam splitter used in their experiment. This result was found to be in contradiction with any classical wave model of light, but agreed with a quantum description involving single-photon states. Using the same source and detection scheme as mentioned above, they also observed interference with a visibility over 98% by building a Mach-Zehnder interferometer around the beam splitter. The results of the first experiment were interpreted using a particle picture, on the contrary a wave picture was used to interpret the second (interference) experiment. Thus wave-particle duality is illustrated by these experiments.

### 1.7.2: FOURTH ORDER INTERFERENCE EXPERIMENTS

Parametric down-conversion [26] is a process in which a pump photon is incident on a crystal, and an idler and a signal photon are produced at frequencies compatible with energy conservation i.e.,

$$\hbar\omega_p = \hbar\omega_s + \hbar\omega_i$$

(1-15)

where  $\omega_p$ ,  $\omega_s$ , and  $\omega_i = \omega_p - \omega_s$  are the frequencies of the pump, signal and idler photons respectively. It is not possible to interpret these photons as localized owing to relativistic constraints [27]. In other words, each photon is broad band. The non-linear susceptibility of the crystal responsible for this process is very weak and consequently, to a good approximation, just these two correlated single photons are found in the output light field. These photons are in the entangled state, given by

$$|\psi\rangle_s = \int d\omega_s \varphi(\omega_s) |\omega_s\rangle |\omega_p - \omega_s\rangle$$

(1-16)

Here  $\varphi(\omega_s)$  is the probability amplitude for production of a signal photon at  $\omega_s$ , while  $|\omega_s\rangle$ ,  $|\omega_p - \omega_s\rangle$  represent monochromatic single photon states at frequencies  $\omega_s$  and  $\omega_p$ , respectively. An important example of such an entangled state is the Einstein-Podolsky-Rosen-Bohm singlet state which produces a violation of Bell's inequalities [28].

A number of fourth-order optical interference experiments [29-39, and some of the references therein ] have been carried out in recent years. Unlike conventional second-order interference experiments, these depend on the detection of photon pairs and in the interference of two two-photon probability amplitudes [40]. It is an interesting features of these experiments that quantum mechanics allows the visibility of the interference to be larger for a two-photon

state than is allowed by classical electromagnetic theory.

A brief outline of some of these experiments, demonstrating the properties of the entangled two-photon state produced in parametric down-conversion, is given below:

#### 1.7.2.1: Experiment of C.K.Hong, Z.Y.Ou, and L.Mandel [30]

The coherence length of the light generated in the process of parametric down-conversion was measured [40] by making use of the technique in which two similar pulses were superposed and the overlap was measured with a device having a non-linear response. The coherence time was found to be of sub-picosecond duration, as predicted theoretically [41]. But the technique suffered the drawback of using very intense light pulses which were of no use for the measurement of single photons. On the other hand, one is usually limited by the resolving time of the photodetectors ( $\approx 100$  ps or longer [42]) while determining the time interval between two photons.

The above mentioned limitations were overcome by C.K.Hong et al (1987)[30] in an experiment in which a fourth-order interference technique was used to measure the time interval between signal and idler photons, and by implication the length of the photon wavepacket, produced in the process of parametric down-conversion.

An outline of the experiment is shown in Fig.(1.2). A coherent beam of light of frequency  $\omega_0$ , from an argon-ion laser oscillating on the 351.1-nm line falls on an 8-cm-long non-linear crystal of potassium dihydrogen phosphate, where some of the incident photons split into two lower-frequencies

$\omega_1$  and  $\omega_2$ , such that  $\omega_0 = \omega_1 + \omega_2$ . The signal and idler photons are directed by mirrors  $M_1$  and  $M_2$  to pass through a beam splitter BS as shown, and the superposed beams interfere and are detected by photodetectors  $D_1$  and  $D_2$ . The coincidence rate of the photons was measured by displacing the beamsplitter from its symmetry position by various small distances  $\pm c\delta\tau$ . True photon coincidences were plotted as a function of the displacement of the beam splitters and the width of the dip, shown in Fig.(1.3), provided the length of the photon wavepacket. The width of the time interval distribution, which was largely determined by an interference filter, was found to be 100 fs within the experimental error of 1 fs. This experiment has some similarities with the two-photon interference experiment [29] in which fringes were observed and measured but without the use of a beamsplitter.

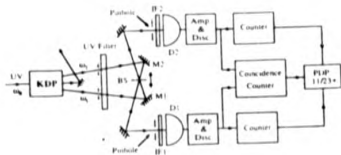


Fig.(1.2).Outline of the experimental set up.

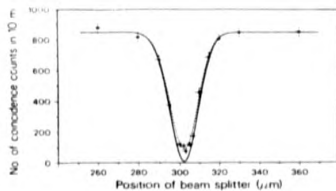


Fig.(1.3).The measured number of coincidences as a function of beam-splitter displacement  $c\delta r$ ,superimposed on the solid theoretical curve.

**1.7.2.2: Experiment of P.G.Kwiat et al [33]**

An interference effect, arising from a two-photon entangled state produced in a potassium dihydrogen phosphate (KDP) crystal pumped by an ultraviolet argon-ion laser, was observed in this experiment. Two conjugate beams of signal and idler photons were injected in a parallel configuration into a single Michelson interferometer, and detected separately by two photomultipliers, while the difference in its armlength was slowly scanned. The signals from the photomultipliers were amplified in a standard manner.

The coherence lengths of the signal and idler photons were measured to be  $\Delta L_s = \Delta L_i = 50 \mu\text{m}$ , which were consistent with the 10-nm bandwidth of filters, used in the experiment, centred at 7.2 nm. The visibility of the fringes in the coincidence count rate was found to be 52.6%  $\pm$  3.0% agreeing, within the experimental error, with the classical predicted value of 50%.

Because of the low percentage of observed visibility, no claim could be made about the existence of any non-classical effect. The classical explanation would be no longer possible in this case if they had succeeded in obtaining visibility greater than 50%.

**1.7.2.3: Experiment of Z.Y.Ou et al [34]**

A simple form of fourth-order interference with two photons was proposed by Franson [43] as a test for locality violation without spin or polarization, giving a fringe visibility greater than 71%. Franson supposed that the two photons might be produced by the cascade decay of an atom in which the initial excited state is very long lived. But Z.Y.Ou et al [34] supposed that

the two photons arose from the down-conversion of a highly monochromatic beam, of long coherence time, in a non-linear crystal.

Despite the fact that the two detectors were widely separated and the trajectories of the two photons never mixed, they looked for the simultaneous detection by both the detectors and were successful in observing that the two-photon probability amplitude for the shorter paths interfered with the two-photon probability amplitude for the longer paths involving the two mirrors. The coincidence rate was found to exhibit a cosine variation with variation in path difference as predicted.

#### 1.7.2.4: Experiment of J.G.Rarity et al [35]

In this experiment, pairs of 826.8-nm correlated photons, generated by parametrically down-converting 413.4-nm Krypton-ion laser light, were directed into a single Mach-Zehnder interferometer such that each photon of the pair enters a different input port. The rate of coincidence at the two output ports displayed oscillations (as the path-length difference is swept) with a spatial period equal to the 413-nm wavelength of the pump photon, and with a visibility of 62% when the path length difference exceeded the coherence length of the individual photon beam. This experiment unequivocally demonstrated the non-classical and entangled nature of the two-photon state.

#### 1.7.2.5: Experiment of P.G.Kwiat et al [36]

Whenever a quantum system evolves adiabatically and cyclically and goes back to its initial state, it develops a certain amount of phase, called Berry's phase [44]. There has been a controversy as to whether one should view

optical Berry's phases as originating from the quantum or classical level. P.C. Kwiat et al [36] resolved this controversy by observing on the quantum level one form of Berry's phase, Pancharatnam phase, which was generated after a cycle of polarization states. In their experiment they detected the coincidence of photon pairs, produced in parametric down-conversion process, in conjunction with a Michelson interferometer in which one member of each pair acquired a geometrical phase due to a cycle in polarization states. The visibility of the coincidence fringes was found to be quite high, viz, 60 %  $\pm$  5%. These results were interpreted in terms of a non-local collapse of the wavefunction.

#### 1.7.2.6: Experiment of L.J. Wang et al [37]

According to the de-Broglie guided-wave theory, which is a hybrid of classical and quantum concepts, there exist waves as well as particle-like photons, the former serving as a guide for the latter. A two-photon interference experiment, proposed by Croca et al [45], suggested that interference effects were expected classically but not on the basis of quantum mechanics. They analyzed their experiment within the framework of the de-Broglie Guided wave theory.

A two-photon interference experiment was carried out, based on an idea proposed by Croca et al, by Wang et al [37] to test the prediction of the de-Broglie guided wave theory. The experimental results contradicted what was expected on the basis of the de-Broglie guided wave theory, but were in good agreement with the prediction of standard quantum theory.

### 1.7.2.7: Experiment of A.M.Steinberg et al [38]

In classical physics, there exist important distinctions between various velocities of propagation of waves i.e., the phase,group,front,signal,and energy velocities. Since the advent of quantum mechanics,the question naturally arises:At which of these velocities does the photon propagate?. One might guess that the photon travels at the group velocity in region of normal dispersion and negligible absorption, but there existed no justification for this guess. Hence a need was there to establish the above mentioned guess experimentally.

A.M.Steinberg et al (1992) [38] demonstrated for the first time that single photons in glass travel at the group velocity and observed a novel, non-local dispersion-cancelling effect. They used a two-photon interferometer in which a conjugate pair of photons produced in parametric fluorescence travelled separate paths and were detected in coincidence after being recombined at a beamsplitter. A piece of glass was placed in the path of one of the photons, and a variable delay was adjusted to precisely compensate for it. The single-photon propagation time was measured to within approximately 4 fs. This kind of measurement was an interesting manifestation of non-local correlations in quantum optics.

### §1.8: PROPOSED EXPERIMENT

As has been discussed above there has been considerable recent interest, on the one hand, in the coherence properties of two-photon radiation produced, for example, in the parametric down conversion process [29-39] and, on the

other hand, in so-called true single-photon interference experiments [25]. It is proposed here to carry out a single photon interference experiment using the polarization properties of the two photons produced in the decay of metastable atomic hydrogen. Previously, investigation of the polarization properties of these two photons has resulted in a particularly fruitful and successful series of experiments [14, 24] to test Bell's inequality and other aspects of the debate between local realism and quantum mechanics. This new experiment will resolve the controversy surrounding the correct coherence length to be associated with these photons and will allow, in a novel way, the measurement of the coherence length of the single photons of the pair, which, from bandwidth considerations, is predicted to correspond to less than two optical cycles at the centre frequency.

A conventional interferometer (Michelson, Mach-Zehnder) consists of a method of splitting a beam of light, introducing a phase shift by varying the optical path length in one arm and then recombining the beam. A maximum or minimum intensity is transmitted depending on the amount of phase shift introduced, but there will be no interference if the coherence length of the light is less than the difference in the optical path length.

It is also possible to construct what would be called a "polarization interferometer" by replacing the usual beam splitters by polarizing beam splitters as shown in Fig.(1.4). If the input beam is, say, linearly polarized at  $45^\circ$  to the polarizer axis then the emerging light will be in a state of pure elliptical polarization the characteristics of which depend on the optical path

difference. If, however, the optical path difference is greater than the coherence length of the light, the emerging orthogonally polarized components will not interfere with each other and the emerging light will appear to be unpolarized. An interferometer of this kind could, therefore, be used to measure the coherence length of the light by observing the variation of the degree of polarization of the emerging radiation rather than the modulation of the intensity used in a conventional interferometer.

To construct a polarization interferometer along the lines described above in the ultraviolet for a low intensity source of the kind used in our two-photon experiment at Stirling is difficult. However, essentially the same action can be provided by a multiwave plate made from uniaxial material as shown in Fig.(1.5). The first surface of the plate acts as a polarizing beam splitter, the two orthogonally polarized components travelling at different speeds through the material introduces a phase shift and the components recombine on emerging from the second surface.

The behaviour of single photons in such an interferometer can be examined in our two-photon source [24] in which the photon pair is in the polarization state described by the entangled state

$$|\Psi\rangle = \frac{1}{\sqrt{2}} (|x_1\rangle \otimes |x_2\rangle + |y_1\rangle \otimes |y_2\rangle)$$

(1.16)

Then, in an arrangement in which an x-polarized photon is detected on one side of the source, we can be sure that the correlated photon on the other side

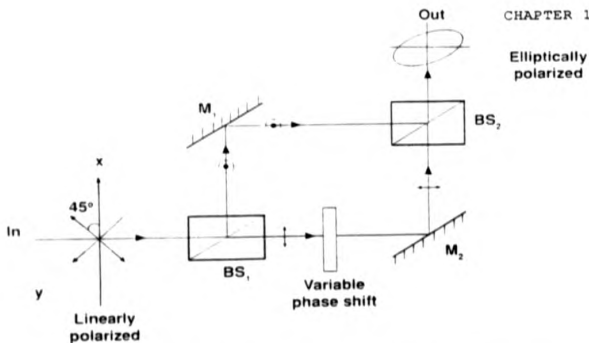


Fig.(1.4).A polarization interferometer using polarizing beam splitters.

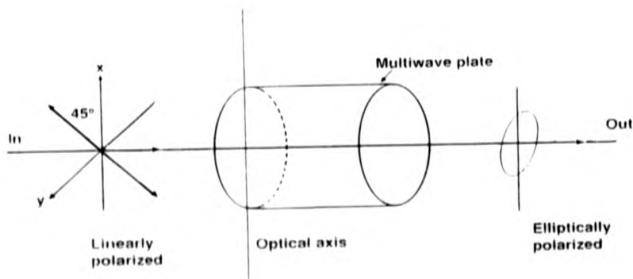


Fig.(1.5).A polarization interferometer using a multiwave plate.

is also polarized in the x direction. A single photon polarization interferometer can thus be constructed as shown in Fig.(5.5) in chap.V; the outputs of the photomultipliers  $D_1$  and  $D_2$  being detected in coincidence in the usual manner.

As the optical path difference  $\delta$  is increased (by, for example, varying the thickness of the multiwave plate) the degree of polarization  $P$ , given by,

$$P = \sqrt{P_1^2 + P_2^2 + P_3^2} \quad (1.17)$$

of the emerging radiation will decrease [45] because of the finite coherence length  $L_c$  of the photon. In eq.(1.17),  $P_1$ ,  $P_2$  and  $P_3$  are the Stokes' parameters [46].

A measurement of the coherence length  $L_c$  can then be made from the variation of  $P$  with  $\delta$  as indicated in Fig.(1.6). In the case of the photons emitted in the decay of metastable atomic hydrogen the coherence length, based on the experimentally observed bandwidth from 185 nm to 355 nm, is expected to be of the order of 350 nm, i.e. of the order of the wavelength of the radiation itself.

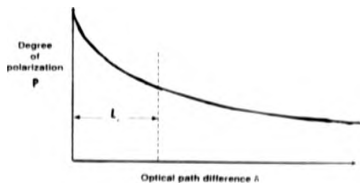


Fig.(1.6) Notional variation of degree of polarization with optical path difference

It is interesting to note that if  $\delta \gg L$ , then two peaks will, in principle, be observable in the coincidence spectrum with time separation  $\delta/c$  and we would conclude that the photon "came through" the multiwave plate linearly polarized along the optic axis or at right angles to it. Thus, as we should expect, the condition  $\delta \gg L$ , resulting in no interference between components, corresponds to the situation where we "know" through which arm of the "interferometer" the photon has passed. If the incident photon is in the state  $(|x\rangle + |y\rangle)/\sqrt{2}$  then, in the experiment, for each event we have made a measurement "forcing" the photon to be in either the  $|x\rangle$  or  $|y\rangle$  polarization state. On the other hand, if  $\delta \ll L$ , the components recombine on emerging from the multiwave plate to give an elliptically polarized photon and no time separation will occur in the coincidence time spectrum. In this case we do not "know" through which arm of the "interferometer" the photon has passed.

The above discussion, of course, implicitly assumes that a single photon of a pair, following a quantum measurement on the other correlated photon of the pair, possesses a bandwidth-determined coherence length which can be measured. In this case it seems reasonable to assume that the single photon can be represented by a single photon wavepacket with very short coherence length. However, as pointed out, for example, by Franson[42], the two photons, before detection of either one, must initially be described by wavepackets of a different nature. Since, in fact, the lifetime of the metastable state is about  $1/7$  second the coherence length to be associated with the two-photon excitation is extremely large and, if it is this coherence length which

determines the interference properties of single photon in its passage through the multiwave plate, the variation of the degree of polarization with optical path difference described above will not be observed.

Using the experimental arrangement shown in Fig.(1.8) the Stokes' parameters of the radiation on the right (in Fig.1.8) will be measured,with the polarizer on the left set with its transmission axis parallel to the x-axis,for various values of optical path difference in the multiwave plate. From these measurements,a value for the coherence length will be found as discussed above and the controversy surrounding the coherence length to be associated with single photons of a two-photon pair will be resolved.

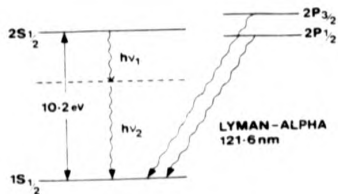
## CHAPTER II

### THEORY

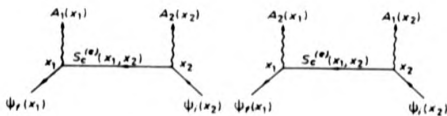
#### §2:INTRODUCTION

A wide variety of experiments [47-49] on atomic radiation and the interaction of atoms with external fields is made possible by the fact that the  $2S_{1/2}$  state of hydrogen and hydrogenic ions is metastable. It has long been known that the  $2S_{1/2}$  state is rapidly quenched to the ground state by the application of a modest electric field with the emission of Lyman-alpha ( $L_{\alpha}$ ) photons. However, as shown in Fig.(2.1), a careful study of the quenching reveals that a rich diversity of interference effects and quantum beat phenomenon are possible. High precision measurements of these effects provide a unique opportunity to test the theory of the radiation process in one electron ions where accurate theoretical predictions are easily possible, and to look for exotic effects such as parity non conservation.

The aim of this chapter is to discuss briefly in section § 2.1 the theory of the spontaneous radiation from the  $2S_{1/2}$  state of hydrogen and then to present very briefly the theory of the two photon transition in section § 2.3 and finally in sections § 2.3-2.8, the quantum mechanical description of two photons and their interaction with polarizers,retarders etc



Fig(2.1).Level diagram for atomic deuterium,neglecting hyperfine structure(not to scale).The two photons,frequency  $\nu_1$  and  $\nu_2$ ,can have any energy provided  $h\nu_1 + h\nu_2 = 10.2\text{eV}$ ( $h$  is Planck's constant).



Fig(2.2). Feynman diagrams for two-photon decay.

## §2.1: THEORY OF SPONTANEOUS RADIATION

A convenient starting point for the theory of the radiative transitions is Fermi's Golden Rule for the transition probability per unit time from state  $|i\rangle$  to state  $|f\rangle$

$$P_{i \rightarrow f} = \frac{2\pi}{\hbar} |\langle f | V_i | i \rangle|^2 \rho_f \quad (2-1)$$

where  $V_i$  is an interaction energy operator and  $\rho_f$  is the number of final states per unit energy interval. For the emission of a photon of frequency  $\omega$ , polarization  $\hat{e}$  and propagation vector  $\kappa$  ( $|\kappa| = \omega/c$ ), the terms in eq.(2-1) are

$$\rho_f = \frac{V \kappa^2 d\Omega}{(2\pi)^3 \hbar c} \quad (2-2)$$

and

$$V_i = e \mathbf{A} \cdot \mathbf{A}^* \quad (2-3)$$

where  $\rho_f$  is the number of photon states of polarization  $\hat{e}$  per unit energy interval and solid angle in the arbitrary normalization volume  $V$ . The photon vector potential, normalized to a field energy of  $\hbar\omega$  per unit volume, is given by

$$A = \frac{1}{k} \sqrt{\frac{2\pi\hbar\omega}{V}} \delta e^{i\mathbf{k}\cdot\mathbf{r}}$$

(2-4)

The wavefunctions in eq.(2-1) are assumed to be four-component Dirac spinors and  $\alpha$  is the usual 4x4 Dirac matrix. Collecting terms,eq.(2-1) reduces to

$$P_i = \frac{e^2 k}{2\pi\hbar} \int (f, \mathbf{a} \cdot \delta \exp(i\mathbf{k}\cdot\mathbf{r}) |i\rangle)^2 d\Omega$$

(2-5)

In the non-relativistic limit,  $\alpha = \mathbf{p}/mc$ ,  $\exp(i\mathbf{k}\cdot\mathbf{r}) = 1$  and eq.(2-5) becomes the familiar dipole velocity form for the transition rate [50]. When eq.(2-5) is applied to the  $2S_{1/2}$  state of hydrogen, one finds that electric dipole ( $E_1$ ) transitions to the  $1S_{1/2}$  ground state are strictly forbidden by the parity selection rules, but spontaneous magnetic dipole ( $M_1$ ) transitions are allowed when relativistic and retardation corrections are taken into account.

An extensive study of both the spontaneous and field induced single photon decay has been carried out by Drake [51] and Feinberg and Saucher [52] by expanding the plane wave vector potential into transverse electric and magnetic multipoles to finally obtain the result

$$P_i (2S_{1/2} \rightarrow 1S_{1/2}) = (\alpha^3 Z^{10} / 972) \tau^{-1} \quad (2-6)$$

For hydrogen H, eq.(2-6) gives an  $M_1$  decay rate of only  $2.496 \times 10^6 \text{ sec}^{-1}$ , which is much less than the  $2E_1$  decay rate (see section 2.1.1). However the process is still important for the following reasons:

- The total  $2S_{1/2}$  decay rate in hydrogenlike atoms with high  $Z$  has been observed by Gould and Marrus [53] and is sensitive to the  $M_1$  contribution and further experiments are in progress on  $U^{91}$  [54].
- The  $M_1$  process produces interference effects even for light hydrogenlike ions. Possible electron self energy and vacuum polarization correction to the basic  $M_1$  decay have been studied by Lin and Feinberg [55], Drake [56] and Barbieri and Saucher[57].

### 2.1.1: TWO PHOTON TRANSITION

We have discussed in the previous section §2.1 the single photon  $M_1$  and induced  $E_1$  decay modes of the  $2S_{1/2}$  state. However, in the absence of external fields, the dominant decay mechanism to the ground state for  $Z(40)$  is the simultaneous emission of two- $E_1$  photons. The two  $E_1$  process arises from a second order interaction between the atom and the radiation field, as first shown by Goeppert-Meyer [58]. Non-relativistic calculations of the decay rate have been performed by several authors, beginning with the early estimates of Breit and Teller[59] and culminating with the highly accurate values of Klarsfeld[60] and Drake[61]. The application of more elegant mathematical techniques for performing implicit summations over intermediate states is discussed in recent papers by Tung et al [62] and Costescu et al [63].

The two photon decay rate of neutral hydrogen is difficult to measure because the rate is only  $8.229 \text{ sec}^{-1}$ . However, the emission has been observed in experiments by D.O'Connell et al [47], and Kruger and Osd [64]. In closely related work, Perrie et al [24] and Haji-Hassan et al [14] have measured the

polarization correlation of the two photons emitted by metastable atomic deuterium. These experiments are particularly significant because the results are in agreement with the predictions of quantum mechanics, but violate Bell's inequality by nearly two standard deviations. These experiments therefore help to rule out the possibility of constructing a theory in which the indeterminacy of quantum mechanics is removed by the introduction of local "hidden variables" as inspired by the famous Gedanken experiments of Einstein, Podolsky and Rosen [2] and Bohm [10]. Even larger violations of Bell's inequality have been observed by others, culminating in the meticulous work of Aspect, Dalibard and Roger [20-21]. However, their experiments are based on photons produced in an atomic cascade of single photon emissions, rather than a true two-photon process, and may be affected by significant absorption and re-emission processes in the source.

In recent years, interest has centred on two-photon transitions in heavier hydrogenic ions. Since the decay rate increases in proportion to  $Z^6$  along the isoelectronic sequence, accurate atomic-beam measurement of the decay rates become feasible. Such measurements have been performed for  $\text{He}^+$ ,  $\text{Li}^{2+}$ ,  $\text{O}^{7+}$ ,  $\text{F}^{8+}$ ,  $\text{S}^{15+}$  and  $\text{Ar}^{17+}$ . An accurate value of the two-photon decay rate is required in experiments to derive the Lamb shift from the electric field quenching rate of the  $2S_n$  [65].

For these high- $Z$  ions, relativistic effects become important. Accurate calculations, including relativistic effects to all orders, have been done by Goldman and Drake [66], and Parpia and Johnson [67].

There now follows a brief description of theory of two-photon transitions:

### 2.1.2: THEORY OF TWO-PHOTON TRANSITION

The theory of the two photon transition is best discussed in terms of the scattering matrix formalism of quantum electrodynamics. It is instructive, first, to reconsider the results of section §2.1 for single photon transitions within the S-matrix formalism, and then to generalize to the two photon case. The spontaneous emission of a single photon of frequency  $\omega$  and polarization  $\hat{e}$  is described by the first order S-matrix element

$$S_{if} = \frac{-ie}{\hbar} \int \bar{\psi}_f(x) A \cdot \psi_i(x) d^4x \quad (2-7)$$

where, in 4-component notation,

$$A = \gamma_\mu A_\mu, \quad \bar{\psi} = \psi^\dagger \gamma_4, \quad d^4x = d^3x dt$$

In the following discussion a summation over repeated indices is implied. The necessary 4-vectors are defined by

$$\begin{aligned} \gamma &= (-i\beta\alpha, \beta), \\ \mathbf{x} &= (\mathbf{r}, ict), \\ \mathbf{k} &= (\mathbf{k}, i\omega/c), \\ \Lambda &= (\Lambda, i\Lambda_0) \end{aligned} \quad (2-8)$$

with

$$\alpha = \begin{pmatrix} 0 & \sigma \\ \sigma & 0 \end{pmatrix}, \beta = \begin{pmatrix} 0 & 1 \\ 1 & 0 \end{pmatrix}$$

where  $\sigma$  are the Pauli's spin matrices, and

$$\Psi_n(x) = \Psi_n(r) e^{-\frac{iE_n t}{\hbar}}$$

describes a stationary state of the electron with energy  $E_n$ .

In the Coulomb gauge, the scalar potential  $A_0$  is zero and the vector potential is

$$A(x) = \frac{1}{\kappa} \sqrt{\frac{2\pi\hbar\omega}{v}} \mathcal{E} e^{ikx} A(r) e^{-i\omega t} \quad (2-9)$$

The part  $A(r)$  is the same as defined by eq.(2-4) in the previous section. On substituting the above into eq.(2-7), the integral over  $dt$  just gives a factor of  $2\pi\delta(\omega - \omega_1 + \omega_2)$ , where  $\omega_1 = E_i/\hbar$ . The remaining part of  $S_{if}$  can be written in the form

$$S_{if} = \left( \frac{-2\pi i}{\hbar} \right) U_{if}^{(1)} \delta(\omega - \omega_1 + \omega_2) \quad (2-10)$$

where

$$U_{if}^{(1)} = -e \int \psi_f^*(x) \alpha \cdot A(x) \psi_i(x) d^3x \quad (2-11)$$

$U_{if}^{(1)}$  is the matrix element of the effective interaction energy of the electron with the electromagnetic field. It is related to the spontaneous decay rate by

$$\omega = \frac{2\pi}{h} |U_{if}^{(1)}|^2 \rho_f(\omega) |k_{\omega, \sigma_f, \sigma_i}| \quad (2-12)$$

which is the same as eq.(2-1).

The simultaneous emission of two photons with vector potentials  $A_1(x)$  and  $A_2(x)$  correspond to the second order Feynman diagram shown in Fig.(2.2).

By developing the corresponding second order matrix Drake[66] gave the following result

$$S_{if}^{(2)} = \frac{2\pi i}{h} U_{if}^{(2)} \delta(\omega_i + \omega_2 - \omega_f - \omega_1) \quad (2-13)$$

where

$$U_{if}^{(2)} = \frac{e^2}{h} \sum_n \left[ \frac{\langle f | \alpha \cdot A_1^*(\omega_2) | n \rangle \langle n | (\alpha \cdot A_2^*(\omega_1) | i \rangle}{\omega_n + \omega_2 - \omega_i} + \frac{\langle f | \alpha \cdot A_2^*(\omega_1) | n \rangle \langle n | (\alpha \cdot A_1^*(\omega_2) | i \rangle}{\omega_n + \omega_1 - \omega_i} \right] \quad (2-14)$$

is the second order interaction energy. Eq.(2-14) is a general formulation and applies to any two photon transition involving states with total angular momenta  $|j, j\rangle$ .

The two photon transition rates have been calculated by Drake and Goldman[68]. The total two photon decay rate integrated over frequencies is defined by

$$\overline{\omega_{2\gamma}} = 1/2 \int \frac{d\omega}{d\gamma} d\gamma$$

(2-15)

The factor of 1/2 is included because the two photons are indistinguishable. The total theoretical decay rate of the  $2S_{1/2}$  state is given by

$$\overline{\omega_{\text{total}}} = \overline{\omega_{2\gamma}} + \overline{\omega_{M_1}}$$

(2-16)

where  $\omega_{M_1}$  is the spontaneous  $M_1$  decay rate discussed in section §2.1. All of the theoretical calculations were found to be in good agreement with the experimental work of Träbert [69] for  $\text{Ar}^{17}$ . A discussion on quadrupole radiation can be found in [68].

### §2.2: STATE VECTOR REPRESENTATION OF TWO PHOTON PAIRS

Figure 2.1 (see §2.1) demonstrates the important transition routes for the emission of a two-photon pair from the decay of a metastable deuterium atom which is in a state of zero angular momentum before and after emission. Restricting our attention to the case where the two photons move in diametrically opposite directions and, since the electric dipole operation is diagonal in nuclear and electronic spins as pointed out by Breit and Teller [59], the transition  $2S_{1/2} \rightarrow 1S_{1/2}$  results in a pair of photons with no net angular momentum. Also the initial and final atomic states are both of even parity, so that if  $\hat{P}$  is the parity operator for which

$$\hat{P}|R_1\rangle = |L_1\rangle, \hat{P}|L_1\rangle = |R_1\rangle$$

then in order to conserve parity we require

$$P|\psi\rangle = +|\psi\rangle \quad (2-17)$$

corresponding to even parity for the photon pair.

As a result of the conservation principles of angular momentum and parity, the state vector for the two photon in circular polarization basis can therefore be written as [14]

$$|\psi\rangle = \frac{1}{\sqrt{2}} (|R_1\rangle \otimes |R_2\rangle + |L_1\rangle \otimes |L_2\rangle) \quad (2-18)$$

where  $|R_1\rangle$  and  $|L_1\rangle$  represents photons of right-handed and left-handed helicity respectively, propagating to the right, while  $|R_2\rangle$  and  $|L_2\rangle$  represent photons of similar helicities propagating to the left. The state vector, given by, eq.(2-18) also applies to the two-photon pair from a  $j=0 \rightarrow 1 \rightarrow 0$  atomic cascade.

Quantum mechanically, measurements with a circular polarizer causes a collapse of the state vector given by eq.(2-18) into  $|R_1\rangle \otimes |R_2\rangle$  or  $|L_1\rangle \otimes |L_2\rangle$  each possibility occurring with probability one half. Thus both photons have either right-handed helicity as in the state  $|R_1\rangle \otimes |R_2\rangle$  or left-handed helicity for the state  $|L_1\rangle \otimes |L_2\rangle$ . On the other hand for a system with odd parity i.e.,

$$P|\psi\rangle = -|\psi\rangle$$

the state vector given in eq.(2-18) takes the form

$$|\Psi\rangle = \frac{1}{\sqrt{2}} [ |R_1\rangle \otimes |L_2\rangle - |L_1\rangle \otimes |R_2\rangle ] . \quad (2-19)$$

representing the two photons emitted in a  $j=1 \rightarrow 1 \rightarrow 0$  atomic cascade.

In the case where the two photons propagate along  $\pm z$  directions, then one can easily transform eq.(2-18) in terms of linear polarization basis  $|x\rangle, |y\rangle$  as follows

$$|\Psi\rangle = \frac{1}{\sqrt{2}} [ |x_1\rangle \otimes |x_2\rangle + |y_1\rangle \otimes |y_2\rangle ] \quad (2-20)$$

The above relation has been obtained by using the following relations:

$$|R\rangle = \frac{1}{\sqrt{2}} [ |x\rangle + i|y\rangle ]$$

$$|L\rangle = \frac{1}{\sqrt{2}} [ -|x\rangle + i|y\rangle ] \quad (2-21)$$

for photons propagating in the  $z$ -direction.

It should be noted that the state vector  $|\Psi\rangle$  given by eq.(2-20) is invariant with respect to rotation about the propagation axis ( $\pm z$ -axis). Also it has no general polarization state prior to measurement. It is the measurement with linear polarizers, that collapses the state vector  $|\Psi\rangle$  to  $|x_1\rangle \otimes |x_2\rangle$  or  $|y_1\rangle \otimes |y_2\rangle$

instantaneously when one of the photons of the pair is first analyzed and detected, irrespective of the separation between them and of the choice of  $x$  or  $y$  direction which is arbitrary with respect to rotation about the axis of propagation. Thus, the result of the polarization measurement of the photon by a detector on one side can be considered to determine instantaneously the result for the polarization state of the other photon of the pair, despite the fact that the detection events are space-like separated in the relativistic sense.

### §2.3: DENSITY MATRIX REPRESENTATION OF THE TWO PHOTON PAIR

The state vector eq.(2-20), representing the two photon pair, can also be represented in the matrix form(see Appendix;§D) as follows. We have seen that in the linear polarization basis

$$|\psi\rangle = \frac{1}{\sqrt{2}} [ |x_1\rangle \otimes |x_2\rangle + |y_1\rangle \otimes |y_2\rangle ] \quad (2-22)$$

so that its adjoint is

$$\langle\psi| = \frac{1}{\sqrt{2}} [ \langle x_1| \otimes \langle x_2| + \langle y_1| \otimes \langle y_2| ] \quad (2-23)$$

The density matrix, (a detailed description of the density operator and its importance is given in Appendix;§B) representing the two photon pair, is then

given by

$$\rho = |\psi\rangle\langle\psi| \quad (2-24)$$

$$\rho = \frac{1}{2} [|x_1\rangle\langle x_1| \otimes |x_2\rangle\langle x_2| + |x_1\rangle\langle y_1| \otimes |x_2\rangle\langle y_2| + |y_1\rangle\langle x_1| \otimes |y_2\rangle\langle x_2| + |y_1\rangle\langle y_1| \otimes |y_2\rangle\langle y_2|] \quad (2-25)$$

In eq (2-25), the parameters, labelled "1" & "2", corresponds to the two photons and during the process of multiplication of matrices (kets and bras), care must be observed that the matrices (kets and bras) for photons labelled "1" and "2" should multiply with their own respective matrices (kets and bras) and the labelled "1" terms should fall on the right side of the symbol  $\otimes$ ; and the terms labelling "2" should fall on the left side of the symbol  $\otimes$ , of course, the matrix multiplication order has to be observed. The use of eq. (A-14) in Appendix, §A) converts the above equation eq. (2-25) into the following form

$$\rho = \frac{1}{2} \begin{pmatrix} 1 & 0 & 0 & 1 \\ 0 & 0 & 0 & 0 \\ 0 & 0 & 0 & 0 \\ 1 & 0 & 0 & 1 \end{pmatrix} \quad (2-26)$$

In circular polarization basis,  $|\psi\rangle$  and  $\langle\psi|$  takes the forms as given below:

$$|\psi\rangle = \frac{1}{\sqrt{2}} [|R_1\rangle \otimes |R_2\rangle + |L_1\rangle \otimes |L_2\rangle] \quad (2-27)$$

$$\langle \psi | = \frac{1}{\sqrt{2}} [ \langle R_1 | \otimes \langle R_2 | + \langle L_1 | \otimes \langle L_2 | ] \quad (2-28)$$

Thus the density matrix,  $\rho = |\psi\rangle\langle\psi|$ , can be written as (using eqs.2-27,2-28)

$$\rho = \frac{1}{2} [ |R_1\rangle\langle R_1| \otimes |R_2\rangle\langle R_2| + |R_1\rangle\langle L_1| \otimes |R_2\rangle\langle L_2| + |L_1\rangle\langle R_1| \otimes |L_2\rangle\langle R_2| + |L_1\rangle\langle L_1| \otimes |L_2\rangle\langle L_2| ] \quad (2-29)$$

A careful simplification of eq.(2-29) coupled with eq.(A-14) of Appendix;§A) yields exactly the same result as given by eq.(2-26).

#### §2.4: QUANTUM MECHANICAL DESCRIPTION OF ANALYZERS

In quantum mechanics the action of a polarizer may be represented by a linear operator  $\hat{e}$ , with its two orthonormal eigenvectors  $|\epsilon_1\rangle$  and  $|\epsilon_2\rangle$  forming a complete set with non-degenerate eigen values, such that

$$\hat{e} |\epsilon_1\rangle = \epsilon_1 |\epsilon_1\rangle \quad (2-30)$$

$$\hat{e} |\epsilon_2\rangle = \epsilon_2 |\epsilon_2\rangle \quad (2-31)$$

$\epsilon_1$  and  $\epsilon_2$  are generally complex eigenvalues and  $\hat{e}$  corresponds to a normal operator in the sense that it commutes with its adjoint so that

$$[\hat{e}, \hat{e}^\dagger] = 0 \quad (2-32)$$

The projection operators  $P_1$  and  $P_2$  are given by

$$P_1^\wedge = |\epsilon_1\rangle \langle \epsilon_1| \quad (2-33)$$

$$P_2^\wedge = |\epsilon_2\rangle \langle \epsilon_2| \quad (2-34)$$

Thus the normal operator  $\ell^{\wedge}$  can be expressed in terms of projection operators  $P_1^{\wedge}$  and  $P_2^{\wedge}$  as follows

$$\ell^{\wedge} = \ell_1 P_1^{\wedge} + \ell_2 P_2^{\wedge} \quad (2-35)$$

The action of a device, represented by  $\ell^{\wedge}$  on a beam described by a density matrix  $\rho$  given by eq.(2-25) is to transform the polarization state of the two-photon signal to a new state whose density matrix is given by

$$\rho = \ell \rho \ell^{\wedge} \quad (2-36)$$

The trace operation then yields the final probability of joint detection of a photon pair i.e

$$I = \text{Tr } \rho \quad (2-37)$$

#### LINEAR POLARIZER

For a linear polarizer,  $\ell_1$  and  $\ell_2$  in eqs.(2-30,2-31) represent the complex amplitudes for transmission of light parallel and perpendicular to the transmission axis of the polarizer and

$$|\ell_1|^2 = \epsilon_M \quad (2-38)$$

$$|\ell_2|^2 = \epsilon_m \quad (2-39)$$

are the transmission efficiencies of the linear polarizers of light polarized parallel and perpendicular to its transmission axis.

For perfect linear polarizers

$$\epsilon_M = |\ell_1|^2 = 1 \quad (2-40)$$

$$\epsilon_m = \ell_2^2 = 0 \quad (2-41)$$

The projection operators  $P_1^+$ ,  $P_2^+$  for a perfect linear polarizer, with its transmission axis making an angle  $\theta$  with the x-axis, are given by

$$P_1^+ = \frac{1}{2} \begin{pmatrix} 1 + \cos 2\theta & \sin 2\theta \\ \sin 2\theta & 1 - \cos 2\theta \end{pmatrix} \quad (2-42)$$

$$P_2^+ = \frac{1}{2} \begin{pmatrix} 1 - \cos 2\theta & -\sin 2\theta \\ -\sin 2\theta & 1 + \cos 2\theta \end{pmatrix} \quad (2-43)$$

so that the normal operator  $\ell^+$  given by eq.(2-35) becomes

$$\frac{1}{2} \begin{pmatrix} M & N \\ N & \bar{M} \end{pmatrix} \quad (2-44)$$

where

$$\begin{aligned} M &= (\ell_1 + \ell_2) + (\ell_1 - \ell_2) \cos 2\theta \\ \bar{M} &= (\ell_1 + \ell_2) - (\ell_1 - \ell_2) \cos 2\theta \\ N &= (\ell_1 - \ell_2) \sin 2\theta \end{aligned} \quad (2-45)$$

We can also write eq.(2-44) in terms of the two dimensional Pauli spin matrices  $\sigma$

$$\ell^+ = 1/2 [\ell_0 I + \ell^+ \cdot \sigma] \quad (2-46)$$

where,

$$\begin{aligned} \ell_0 &= \ell_1 + \ell_2 = \text{Tr } \ell \\ \ell^+ &= \text{Tr } (\ell \sigma^+) \end{aligned}$$

The components of  $\ell'$  are

$$\ell'_x = (\ell_x - \ell_y)\sin 2\theta, \quad \ell'_y = 0, \quad \ell'_z = (\ell_x + \ell_y)\cos 2\theta$$

### § 2.5: RELATIONSHIP BETWEEN DENSITY MATRIX AND STOKES PARAMETERS

Consider light characterized by a density matrix  $\rho$ , or Stokes parameters  $P_1, P_2, P_3$  (described in Appendix, §E) being analyzed by an imperfect linear polarizer described by a matrix  $A$ . Before passing through the polarizer the light is described by the density matrix  $\rho$  and Stokes parameters  $P_1, P_2, P_3$  and after passing through the polarizer  $A$  the light is described by the density matrix  $\rho'$  or Stokes parameters  $P'_1, P'_2, P'_3$  according to eq.(2-36)

$$\rho' = A \rho A' \quad (2-47)$$

where  $A'$  is the matrix adjoint of  $A$ . The Stokes parameters and density matrices are related by the following expression (Blum, 1981)

$$\rho = \frac{1}{2} \begin{pmatrix} 1 + P_1 & P_2 - iP_3 \\ P_2 + iP_3 & 1 - P_1 \end{pmatrix} \quad (2-48)$$

and the intensity of the two-photon signal recorded by the photomultiplier is then given by eq.(2-37) i.e

$$I = \text{Tr } \rho \quad (2-49)$$

As we have seen the matrix for the linear polarizer  $A$ , as given by eq.(2-44).

is

$$A = \frac{1}{2} \begin{pmatrix} M & \bar{M} \\ N & \bar{N} \end{pmatrix} \quad (2-50)$$

and the adjoint of  $A$  is

$$A^* = \frac{1}{2} \begin{pmatrix} M^* & N^* \\ N^* & M^* \end{pmatrix}$$

where the  $*$  denotes the complex conjugate. Substituting eqs.(2-48,2-50) into eq.(2-49), we obtain

$$I = \frac{1}{4} [L_1^2 + L_2^2 + 2P_1 L_1 L_2 \cos 2\theta + 2P_2 L_1 L_2 \sin 2\theta] \quad (2-51)$$

where

$$L_1 = \ell_1 + \ell_2; \quad L_2 = \ell_1 - \ell_2 \quad (2-52)$$

with the help of eqs.(2-38,2-39,2-52), we can write eq.(2-51) as

$$I = \frac{1}{2} [(\mathbf{e}_M \cdot \mathbf{e}_m) \cdot P_1 (\mathbf{e}_M \cdot \mathbf{e}_m) \cos 2\theta + P_2 (\mathbf{e}_M \cdot \mathbf{e}_m) \sin 2\theta] \quad (2-53)$$

$$= \frac{1}{2} (\mathbf{e}_M \cdot \mathbf{e}_m) [1 + \Pi P_1 \cos 2\theta + \Pi P_2 \sin 2\theta] \quad (2-54)$$

where,

$$\Pi = \frac{e_H - e_m}{e_H + e_m} \leq 1$$

(2-55)

The measured Stokes parameters  $P_1$  and  $P_2$  are derived directly from the measured coincidence rates  $I(0), I(90), I(45), I(135)$  using

$$P_1 = \frac{I(0) - I(90)}{I(0) + I(90)}$$

(2-56)

$$P_2 = \frac{I(45) - I(135)}{I(45) + I(135)}$$

(2-57)

so that  $P_1 = \Pi P_1$  and  $P_2 = \Pi P_2$

Similarly, it can be shown that provided a perfect quarter-wave plate is used in the circular polarization analysis

$$P_3 = \Pi P_3$$

(2-58)

Thus, in order to obtain the true Stokes parameters  $P_1, P_2, P_3$ , the measured parameters  $P_1', P_2', P_3'$  have to be divided by the degree of polarization  $\Pi$ , of the polarizer used.

### §2.6 ANALYSIS OF THE POLARIZATION STATE VECTOR OF THE TWO-PHOTONS BY TWO LINEAR POLARIZERS

In the situation where the two-photons are emitted simultaneously in opposite directions and detected by the two linear polarizers A and B placed diametrically on in opposite sides of the source, as illustrated in Fig.5.1(chap.V;§5.2), one can write [14] the density matrix for the polarization state of the two-photons as

$$\rho_{12} = (A \otimes B) \rho (A \otimes B)^{\dagger} \quad (2-59)$$

Taking the trace yields the intensity of the two-photon coincidence signal,  $I(\theta)$ , i.e

$$I(\theta) = \text{Tr} \rho_{12} = \frac{1}{2} [ (\epsilon_{\parallel}^A \epsilon_{\parallel}^B) \cos^2 \theta + 2\epsilon_{\perp}^A \epsilon_{\perp}^B \sin^2 \theta ] \quad (2-60)$$

where  $\epsilon_{\parallel}$  and  $\epsilon_{\perp}$  are the transmission efficiencies for light polarized in a direction parallel and perpendicular to the transmission axis of each of polarizers A and B. Eq.2-60 gives the following expressions for the two-photon coincidence signal at angles  $\theta=0^\circ, 90^\circ$  and  $\pm 45^\circ$

$$I(0) = \frac{1}{2} (\epsilon_{\parallel}^A \epsilon_{\parallel}^B) ; I(90) = \epsilon_{\perp}^A \epsilon_{\perp}^B ; I(\pm 45) = \frac{1}{4} (\epsilon_{\parallel}^A \epsilon_{\parallel}^B)^2 \quad (2-61)$$

respectively.

The density matrix of the two-photon coincidence signal, after passing through the two linear polarizers A and B and the quarter-wave plate, with its optic axis set at  $\pm 45^\circ$  with respect to the transmission axis of the polarizer B, as illustrated in Fig. 5.2, §5.2 of chap V, is

$$\rho_2 = (A \otimes BR_{1/4}) \rho (A \otimes BR_{1/4})^\dagger \quad (2-62)$$

where  $R_{1/4}$  is the matrix representing the action of a quarter-wave plate, as described in section §2.7, eq. (2-80).

Hence the two-photon coincidence signal, in this case, is

$$I(\theta) = \text{Tr} \rho_2 = \frac{1}{4} (\mathbf{e}_\mu + \mathbf{e}_\nu)^2. \quad (2-63)$$

With  $\theta = \pm 45^\circ$ , Eq. (2-63) gives us

$$I(RHC) = I(LHC) = \frac{1}{4} (\mathbf{e}_\mu + \mathbf{e}_\nu)^2. \quad (2-64)$$

From eqs. (2-61, 2-63), the corresponding Stokes' parameters  $P_1, P_2, P_3$  of the single photon on the right are:

$$P_1 = \frac{I(0) - I(90)}{I(0) + I(90)} = 1; \quad P_2 = \frac{I(45) - I(-45)}{I(45) + I(-45)} = 0; \quad P_3 = \frac{I(RCP) - I(LCP)}{I(RCP) + I(LCP)} = 0. \quad (2-65)$$

§2.7: ANALYSIS OF THE TWO-PHOTON POLARIZATION STATE  
 VECTOR MODIFIED BY THE INSERTION OF AN ACHROMATIC  
 HALF-WAVE PLATE

The two-photon entangled state vector is given by

$$|\Psi\rangle = \frac{1}{\sqrt{2}} [ |x_1\rangle \otimes |y_2\rangle + |y_1\rangle \otimes |x_2\rangle ] .$$

The density matrix for the polarized state of the two-photon signal, after passing through the two linear polarizers A and B and an achromatic half-wave plate, with its optic set at an angle  $45^\circ$  with respect to the transmission of the polarizer B as shown in Fig.5.3, §5.3 of chap V, is given by

$$\rho_s = [A \otimes BR_{\frac{1}{2}}] \rho [A \otimes BR_{\frac{1}{2}}]^\dagger . \quad (2-66)$$

Hence the expression of the two-photon signal, in this case, will be

$$I(\theta) = \text{Tr} \rho_s = \frac{1}{4} [ (\mathbf{e}_M \cdot \mathbf{e}_m)^2 - (\mathbf{e}_m \cdot \mathbf{e}_M)^2 \cos 2\theta ] \quad (2-67)$$

and therefore,

$$I(0) = \mathbf{e}_m \mathbf{e}_m; I(90) = \frac{1}{2} (\mathbf{e}_m^2 - \mathbf{e}_M^2); I(+45) = \frac{1}{4} (\mathbf{e}_m^2 + \mathbf{e}_M^2) \quad (2-68)$$

The density matrix for the two-photon coincidence signal using an achromatic quarter-wave plate and achromatic half-wave plate as shown in Fig.5.4; §5.3 of chap V, is

$$\mathbf{Q}_4 = [A \otimes BR \frac{1}{4} R \frac{1}{2}] \mathbf{Q} [A \otimes BR \frac{1}{4} R \frac{1}{2}]^* \quad (2-69)$$

and hence the intensity of the two-photon coincidence signal, in this case, will be

$$I = \text{Tr} \mathbf{Q}_4 = (\mathbf{e}_m + \mathbf{e}_M)^2 = I(RHC) = I(LHC) \quad (2-70)$$

The Stokes' parameters for the single photon on the right derived from eqs.(2-68,70) are then

$$P_1 = \frac{I(0) - I(90)}{I(0) + I(90)} = - \left[ \frac{\mathbf{e}_m - \mathbf{e}_M}{\mathbf{e}_m + \mathbf{e}_M} \right]^2 = -1; P_2 = \frac{I(45) - I(-45)}{I(45) + I(-45)} = 0; P_3 = \frac{I(RHC) - I(LHC)}{I(RHC) + I(LHC)} = 0 \quad (2-71)$$

In the above equation,  $P_1 = -1$  because of the fact that  $\mathbf{e}_m$  is very small compared to  $\mathbf{e}_M$ .

But we don't assume this in the measurements.

The modulus of the total polarization vector ( $P_1, P_2, P_3$ ) for both the cases (§2.6 and §2.7) is given by

$$|P_{\text{tot}}| = \sqrt{P_1^2 + P_2^2 + P_3^2} = 1 \quad (2-72)$$

**§2.8:RETARDERS**

Retardation plates, or phase shifters, including quarter-wave plates (QWP), half-wave-plates (HWP), and full-wave plates (FWP), are elements primarily used in the synthesis and analysis of light in various states of polarization. The simplest retardation plate is a slice cut out of a uniaxial crystal (birefringent material) such that the slice contains the crystalline optic axis. There is a velocity difference between the ordinary ray (o ray) and extraordinary ray (e ray) within the plate, when a beam of light is incident normally upon it. As the o and e beams traverse the plates, a phase difference accumulates between these rays which is proportional to the distance travelled within the plate. On emerging from the plate the o and e rays recombine to form a beam generally in a different state of polarization from the incident upon it.

The extent to which the phase of one component is retarded relative to the other is called the retardance  $\phi$  (often called the retardation). Retardation is the magnitude of the relative phase change and hence is always positive. The optical path difference  $\delta$  between the two beams is given by

$$\delta = \pm d(n_e - n_o) \quad (2-73)$$

where,

$n_o$  = refractive index of o ray

$n_e$  = refractive index of e ray

$d$  = thickness of the plate

$\lambda$  = wavelength in free space

When  $n_e > n_o$ , we have a positive uniaxial crystal and when  $n_e < n_o$ , we have a negative uniaxial crystal.

The phase difference between two rays travelling through a bi-refringent material is  $2\pi/\lambda$  times the path difference i.e

$$\text{Phase difference} = \phi = (2\pi/\lambda)\delta \quad (2-74)$$

From eqs.(2-73,74), we have

$$\phi = \frac{2\pi d(n_e - n_o)}{\lambda} \quad (2-75)$$

If the thickness of the plate is such that the phase difference (retardation of the slow ray by comparison with the fast ray at emergence) is  $1/4$  wavelength [i.e  $\phi = 2\pi(1/4) = \pi/2$ ], the plate is called a zero or first order QWP. If the phase difference at emergence is  $1/2$  wavelength [ $\phi = 2\pi(1/2) = \pi$ ], the plate is called a zero or first order HWP. If the phase difference at emergence is some multiple of  $1/4$  or  $1/2$  wavelength, the plate is called a multiple order or high order plate. **It is the phase difference and not the physical thickness of the plate to which these names refer.** A retarder that produces the same change irrespective of the wavelength of the light is called **achromatic**.

Since both the o and e ray refractive indices of most materials are strongly wavelength dependent, the retardation which accumulates within a plate of specified thickness is also wavelength dependent.

Within the plane of the retarder, the crystalline optic axis and the axis

normal to it are often called the "fast" or "slow" axes (whichever is appropriate, depending on whether the uniaxial crystal is positive or negative).

By rotating the retarder about one of these axes or the other it is possible to adjust the value of retardation achieved. Rotation about the crystalline optic axis increases the effective thickness of the plate, but does not affect the velocity difference between the o and e rays, thus increasing the accumulated retardation.

Rotation around the other axis both increases the effective thickness of the plate and reduces the velocity difference between o and e rays. The latter effect dominates for small rotation reducing the accumulated retardation. This is how a narrow band retarder may be tuned over a limited range of retardation at fixed wavelength or over a limited range of wavelength at fixed retardation.

The effect of a retarder on a beam of polarized light depends on three things:

- the initial state of polarization
- the orientation of the rotation about an axis perpendicular to the disc measured with respect to the axes of polarization of the incident beam,
- and the net value of retardation.

The effect of the HWP is to rotate the plane of plane polarized light incident with its plane of polarization at an angle  $\theta$  to the axis through an angle  $2\theta$ . The HWP converts LCP (left circular polarized) into RCP (right circular polarized) and vice versa.

If the retarder is a QWP, and the angle  $\theta$  between the electric field vector of the incident linearly polarized beam and the retarder principal plane is  $45^\circ$ , the emergent beam is circularly polarized. Reversing  $\theta$  to  $-45^\circ$  reverses the sense of the emergent circular polarization. Reversing the direction of propagation, a QWP will transform circular polarized light into linearly polarized light.

### 2.8.1: MATRIX REPRESENTATION OF A RETARDER

It can be shown [14] that the general matrix describing the action of a retarder with its optic axis set at an angle of  $\alpha$  with respect to the transmission of a polarizer is given by

$$R_\varphi = \frac{1}{2} [(1 + e^{i\varphi}) I + (1 - e^{i\varphi}) (\sigma_x \sin 2\alpha + \sigma_z \cos 2\alpha)] \quad (2-76)$$

where  $I$  is the  $2 \times 2$  unit matrix and  $\sigma_x, \sigma_z$  are the Pauli's matrices given by

$$I = \begin{pmatrix} 1 & 0 \\ 0 & 1 \end{pmatrix}; \sigma_x = \begin{pmatrix} 0 & 1 \\ 1 & 0 \end{pmatrix}; \sigma_z = \begin{pmatrix} 1 & 0 \\ 0 & -1 \end{pmatrix} \quad (2-77)$$

and  $\varphi$  is the retardation of the retarder.

It can be easily verified from eq.(2-76) that

$$R_\varphi R_\varphi^\dagger = I$$

For  $\alpha = 45^\circ$ , eq.(2-76) can be rewritten as

$$R_{\psi} = \frac{1}{2} \begin{pmatrix} 1 + e^{i\psi} & 1 - e^{i\psi} \\ 1 - e^{i\psi} & 1 + e^{i\psi} \end{pmatrix}$$

(2-78)

and hence

$$R_{\psi}^* = \frac{1}{2} \begin{pmatrix} 1 + e^{-i\psi} & 1 - e^{-i\psi} \\ 1 - e^{-i\psi} & 1 + e^{-i\psi} \end{pmatrix}$$

(2-79)

For a quarter-wave plate  $\psi = \pi/2$  and for a half-wave plate  $\psi = \pi$  so that the corresponding matrices are then given by  $R_{\psi} R_{\psi}^*$

$$R_{\frac{\pi}{4}} = \frac{1}{2} \begin{pmatrix} 1+i & 1-i \\ 1-i & 1+i \end{pmatrix}; R_{\frac{\pi}{2}} = \begin{pmatrix} 0 & 1 \\ 1 & 0 \end{pmatrix}$$

(2-80)

### 2.8.2: RELATIONSHIP BETWEEN THE STOKES PARAMETER AND THE VARIABLE RETARDANCE $\psi$ OF A RETARDER

The density matrix for an x-polarized photon is given by

$$\rho = |x\rangle\langle x| = \begin{pmatrix} 1 \\ 0 \end{pmatrix} \langle x| = \begin{pmatrix} 1 & 0 \\ 0 & 1 \end{pmatrix}$$

(2-81)

The matrix for a retarder whose fast axis makes an angle  $\alpha = 45^\circ$  with the x-axis is given by eq.(2-78). The transmitted two-photon signal after passing through

the retarder is then described by the following density matrix

$$\hat{\rho} = R_{\psi} \rho R_{\psi}^{\dagger} \quad (2-82)$$

With the help of eqs.(2-78,2-79,2-81) the density matrix given by eq.(2-82) is written as

$$\hat{\rho} = \frac{1}{4} \begin{pmatrix} x & y \\ y & x \end{pmatrix} \begin{pmatrix} 1 & 0 \\ 0 & 0 \end{pmatrix} \begin{pmatrix} x^* & y^* \\ y^* & x^* \end{pmatrix} = \frac{1}{4} \begin{pmatrix} xx^* & xy^* \\ yx^* & yy^* \end{pmatrix} \quad (2-83)$$

where  $x = 1 + e^{i\psi}$ ;  $y = 1 - e^{i\psi}$

The terms in (2-83) on its right hand side are:

$$\begin{aligned} xx^* &= 2(1 + \cos\psi) = 4\cos^2\psi/2 \\ yy^* &= 4\sin^2\psi/2; \quad xy^* = 4i\sin\psi/2\cos\psi/2 \\ yx^* &= -4i\sin\psi/2\cos\psi/2. \end{aligned} \quad (2-84)$$

In collaboration with eq.(2-84), eq.(2-83) can be written as

$$\hat{\rho} = \begin{pmatrix} 2\cos^2\frac{\psi}{2} & 2i\sin\frac{\psi}{2}\cos\frac{\psi}{2} \\ -2i\sin\frac{\psi}{2}\cos\frac{\psi}{2} & 2\sin^2\frac{\psi}{2} \end{pmatrix}. \quad (2-85)$$

The density matrix in terms of Stokes' parameters  $P_1, P_2, P_3$ , has already been

established by Blum(1981) and is given by eq.(2-48) in §2.6. Comparison of eq.(2-85) with eq.(2-48) gives the following relations

$$1 + P_1 = 2\cos^2 \frac{\Phi}{2}; 1 - P_1 = 2\sin^2 \frac{\Phi}{2} \quad (2-86)$$

$$P_2 = iP_3 = i\sin\Phi; P_2 = -iP_3 = -i\sin\Phi. \quad (2-87)$$

From eqs.(2-86,87), one can easily derive the following relations:

$$\begin{aligned} P_1(\varphi) &= \cos\varphi \\ P_2(\varphi) &= 0 \\ P_3(\varphi) &= -\sin\varphi \end{aligned} \quad (2-88)$$

Thus we see from the above relations that the Stokes' parameters are very much dependent on the retardance introduced by the retarder. Spectral distribution of the two photon and the transmission efficiencies of the imperfect linear polarizers have not been taken into consideration while deriving these relations. We shall be using these relations to compute the Stokes' parameters of the non-achromatic retarders chosen for our experiment in Chap.IV.

### 2.8.3: ATTAINMENT OF VARIABLE RETARDANCE (NON-ACHROMATIC)

To obtain a variable retardance it would be possible in principle to use a Soleil-Babinet compensator, but this usually has a limited aperture of only 10 mm. Multiple order quartz plates are, in general, too thick (0.75 mm to 1

mm) to investigate effects due to a small optical path difference. Alternatively, one could use zero(first) order plates for a variety of wave lengths to obtain a variable retardance.

For example, say one has a zero order half-wave plate at wave length  $\lambda_1$  of effective thickness  $d$ . The retardation  $R(\lambda_1)$  is

$$R(\lambda_1) = \frac{(n_o - n_e) \lambda_1 2\pi d}{\lambda_1} = \pi = \frac{1}{2} \text{ wavelength} \quad (2-89)$$

or,

$$d = \frac{\lambda_1}{2(n_o - n_e) \lambda_1} \quad (2-90)$$

The retardation produced at some other wavelength  $\lambda_2$  by this plate of thickness  $d$  is

$$R(\lambda_2) = \frac{(n_o - n_e) \lambda_2 2\pi d}{\lambda_2} \quad (2-91)$$

It follows that

$$R(\lambda_2) = \frac{1}{2} \frac{(n_o - n_e) \lambda_2}{(n_o - n_e) \lambda_1} \cdot \frac{\lambda_1}{\lambda_2} \text{ wavelengths.} \quad (2-92)$$

Fig.2.3 shows the birefringence analysis with respect to the wavelength.

Say,  $\lambda_1 = 2\lambda_2$  (as shown in the Fig.2.3) then if correspondingly

$(n_o - n_e)_{\lambda_1} = 2(n_o - n_e)_{\lambda_2}$ , then eq.(2-92) reduces to  $R(\lambda_2) = 2$  wavelengths. In other words, a half wave length retardation at  $\lambda_1$ , becomes a two wavelengths retardation at  $\lambda_2$ . Hence, the formula given by eq.(2-92) is very useful in determining the retardation of a half-wave plate of given thickness at various wavelengths as discussed in section §4.10 (choice of retarders) of Chap IV.

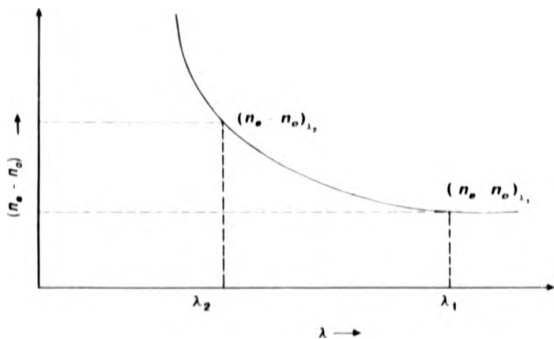


Fig 2.3 Bi-refringence  $(n_o - n_e)$  analysis with respect to wavelength  $\lambda$ .

### 2.8.4: Delay and Displacement of "e" and "o" ray wavepackets by a birefringent plate

Let us assume that a single photon of a two-photon pair can be represented, after detection of the other photon of the pair, by a linearly polarized, minimum uncertainty wavepacket (Fig.2.4) with a spectral distribution  $A(\omega)$  and a carrier frequency  $\omega_c$  (corresponding to a carrier wavelength  $\lambda_c = (2\pi c)/\omega_c = 243$  nm here). On entering a birefringent plate whose axis is set at an angle of  $45^\circ$  to the plane of polarization, the photon can be considered to be split into orthogonally polarized components ("o" and "e" waves) which propagate independently through the plate. The corresponding group velocities are:

$$v_{g_o}(\text{"o" wave}) = \frac{c}{[n_o + \omega_c \left( \frac{dn_o}{d\omega} \right)]_{\omega_c}} \quad (2-93a)$$

$$v_{g_e}(\text{"e" wave}) = \frac{c}{[n_e + \omega_c \left( \frac{dn_e}{d\omega} \right)]_{\omega_c}} \quad (2-93b)$$

The resulting time difference  $\Delta t$  produced between the two components on passing through a plate of thickness  $d$  is

$$\Delta t = \left( \frac{d}{v_{g_o}} - \frac{d}{v_{g_e}} \right) \quad (2-94)$$

On emerging from the plate the two orthogonally polarized components are displaced relative to each other by a distance  $\delta$

$$\delta = c \Delta t = c \left( \frac{d}{v_{g_e}} - \frac{d}{v_{g_o}} \right) = d [n_e + \omega_o \frac{\partial n_e}{\partial \omega}]_{\omega_o} - d [n_o + \omega_o \frac{\partial n_o}{\partial \omega}]_{\omega_o} \quad (2-95 \text{ a})$$

$$\delta = (n_e - n_o)_{\omega_o} d + \omega_o \left[ \frac{\partial (n_e - n_o)}{\partial \omega} \right]_{\omega_o} d \quad (2-95 \text{ b})$$

Now since  $c = v\lambda = (\omega/2\pi)\lambda$ , then on differentiation, we get  $\omega d\lambda + \lambda d\omega = 0$  i.e.  $d\omega/\omega = -d\lambda/\lambda$ . Hence Eq.2-95b becomes

$$\delta = (n_e - n_o)_{\omega_o} d + \lambda_o \left[ \frac{\partial (n_e - n_o)}{\partial \lambda} \right]_{\lambda_o} d \quad (2-96)$$

If the second term in Eq.2-96 is small compared to the first then  $\delta = (n_e - n_o)_{\omega_o} d$  = optical path difference at wavelength  $\lambda_o$ , but, in fact, the second term cannot be neglected in our present case. From table 4-7 (Chap IV), at  $\lambda_o = 243 \text{ nm}$ , we have

$$n_e - n_o = 113.0 \times 10^{-4}; \quad \left. \frac{\partial (n_e - n_o)}{\partial \lambda} \right|_{243} = - \frac{(115.0 - 110.5) \times 10^{-4}}{(255 - 235) \times 10^{-9}} = -2.25 \times 10^4$$

and

$$\lambda_o \frac{\partial (n_o - n_e)}{\partial \lambda} \Big|_{\lambda_o} = -54.7 \times 10^{-4}$$

It follows from Eq.2-96 that

$$\delta = 1.677 \times 10^{-2} d \quad (2-97)$$

We shall be using Eq.2-97 to calculate the relative displacement of wavepacket  $\delta$  for the chosen non-achromatic retarders (discussed in §4.10;chap IV).

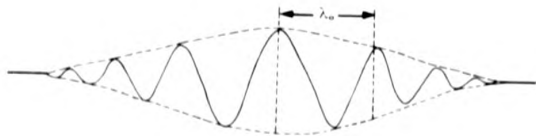


Fig 2.4 Minimum uncertainty packet representing a two-photon pair

## CHAPTER III

### EXPERIMENTAL SET UP

#### §3. INTRODUCTION:

A schematic diagram of the main components of the apparatus is shown in Fig.3.1. A radio frequency (rf) ion source is used to extract a beam of deuterons which are focused by an einzel lens into a caesium charge exchange-cell producing a neutral beam of atomic metastable deuterium (with about 25 % in the excited  $2S_0$  state) which is collimated before entering the detection region. Deuterium was used rather than hydrogen since, for a given metastable density and hence two-photon signal, the noise generated by the interaction of the beam with the background gas was less in the former case. The beam independent background is monitored by closing the gate-valve at either end of the caesium charge-exchange cell, thus cutting off the beam.

In the detection region, the beam is observed by two symmetrically positioned U.V transmitting optical systems consisting of a vacuum window, lens, pile-of-plates polarizer and fast photomultiplier. The photomultiplier tubes are coupled to a delayed coincidence circuit which monitors the distribution of arrival time difference of pulses from the photomultiplier anodes.

The metastable flux is monitored by quenching in an electric field, in the final chamber, and the resulting Lyman alpha radiation is detected by a photomultiplier (PM) in front of which is placed an oxygen filter with lithium fluoride (LiF) window. A C-type electromagnet ( $B=0.05$  Tesla) and Faraday

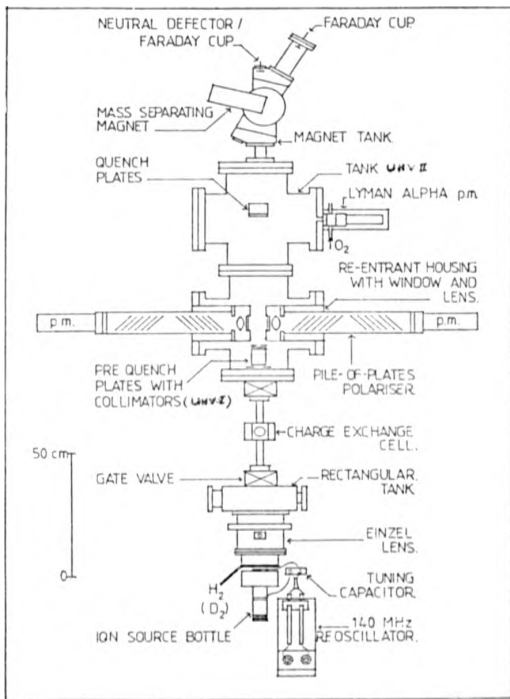


Fig3.1.Schematic diagram of the apparatus.

cup, situated at the extreme end of the apparatus, are used to mass analyze the ions produced before the caesium cell is activated and to collect the neutral beam respectively.

In the following section, a detailed and comprehensive description is given of the major systems and equipments involved in the experiment to produce and manipulate the beam and to detect and analyze the two-photon signal.

### §3.1: DESCRIPTION AND OPERATION OF ION SOURCE

In order to produce an ion beam, an ion source, model C-SO-173 (manufactured by High Voltage Engineering Europe N.V. Amersfoort, the Netherland) was used in the experiment. It is shown in Fig.3.2 along with its power supplies. It is a heavy-duty, prolific source of hydrogen and other ions (e.g. Ar, He, Ne, Ze, Kr, CO<sub>2</sub>, etc)

The quartz source bottle, shown in Fig.3.2, contains the deuterium gas which is supplied from a cylinder of 5 litres at 600 psi and is excited by a 140 MHz, 200 W, self exciting rf oscillator. The rf oscillator has two 4Cx250 B air cooled electron tubes and is capacitively coupled to the plasma discharge.

The rf output is fed via two exciter lines to a 300  $\Omega$  transmission line and is coupled to the source bottle by external electrodes placed on either side of the magnet which is connected to a power supply of 135 V, 1.5 A d.c.

A gap of height 1 inch between the outer edge of the top clip and the magnet on the feeder line, above the shorted end of the exciter line, provides the load adjustment. A variable capacitor (1.6 pF, 1.5 kV), connected in parallel with the electrodes, tunes the source. The three elements of the einzel lens are



supported, aligned and insulated by porcelain insulators. The assembly is, in turn, positioned on the source axis by a close tolerance fit within the vacuum chamber. The lens electrode inside diameter is 1.25 inch.

The rf source and einzel lens assemblies are mounted in a 6-inch diameter bushing assembly, a section of which is insulated for 30 kV. A beam energy up to 35 keV (30 kV accelerating, 5 kV probe) with a maximum current of approximately 2 mA is possible.

The plasma discharge is biased with respect to the extraction canal by the probe voltage. The extraction canal is 2 mm in diameter and 16 mm in length. It is surrounded by an insulating quartz sleeve. A sheath region develops between the canal tip and the body of the discharge as the probe voltage is raised. A spherical plasma surface is formed at the mouth of the quartz sleeve thereby serving as a lens to focus the ions through the canal. The ion beam is accelerated in the region between the canal and the earthed snout of the einzel lens. One can operate the einzel lens by a variable voltage divider fulfilling the condition)

$$V_{\text{focus}} = V_{\text{probe}} + V_{\text{accel}} \quad (3-1)$$

to focus the beam on the target.

Alignment between the source head and lens assembly is predetermined and repeatable. The flow rate of the deuterium gas was controlled by a palladium leak. The source output is optimized by the control of the source gas pressure, magnetic field, oscillator loading and acceleration voltages. The plasma is confined and positioned with an axial magnetic field.

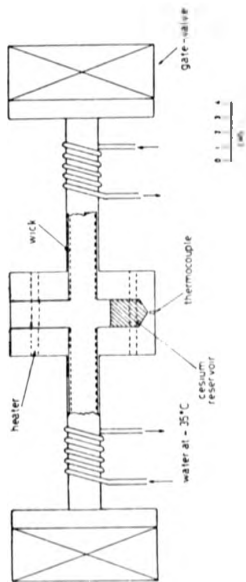
It was possible to operate the ion source for several weeks at low energy = 850 eV with a very stable output, after which the canal and quartz bush need replacement.

### §3.2 CAESIUM CHARGE-EXCHANGE CELL

The caesium charge-exchange cell Fig.3.3 is based on a design proposed by Bacal et al [70]. It is a closed cycle cell which minimises the loss of caesium by returning caesium metal, which condenses on the cell ports, continuously to the cell evaporator.

The central region of the cell (the evaporator) is heated to a temperature at which the desired caesium vapour pressure is obtained. In our case, the caesium was heated to between 100°C and 110°C temperature at which a vapour pressure of  $10^{-3}$  torr could be achieved. A temperature of between 30°C and 40°C, a few degree higher than the melting point of caesium which is 28.5 °C, is imposed on the extremities of the cell by temperature controlled circulating water. By doing so, we thus create a temperature gradient outside the central isothermal region.

The internal surface of the cell is lined with several layers of fine stainless steel wire mesh (wick) tightly fitting against the wall. The heater wire, to heat the caesium, is made of Kanthal material of length 7m and of resistance 90Ω. The liquid caesium which condenses on the wall is spread out by capillary action and does not get a chance to "ball up" and block the beam. The caesium is continuously purified by successive processes of evaporation and condensation.



Fig(3.3) Cesium charge-exchange cell

The caesium loss rate through the ports of this type of cell is reported to be [71]  $6.1 \times 10^{-4}$  g/hr at the evaporator temperature of 110°C and a condenser temperature of 32°C.

The cell can be isolated from the vacuum system by means of gate valves at either end. It has three auxiliary ports one of which supports a needle valve for flushing the cell with Argon/Nitrogen when charging with caesium and the other supports a Langmuir-Taylor hot wire ionization detector.

### §3.3: VACUUM SYSTEM

The vacuum system consists of three stainless chambers, individually pumped, designated from the source as a rectangular tank, vacuum generator chamber I (VGI) and vacuum generator chamber II (VGII). All these chambers can be isolated from their pumping systems by quarter swing butterfly valves, pneumatically controlled. A brief description of these chambers is given below:

#### Rectangular Tank

This tank takes the form of a rectangular shaped chamber, of dimensions  $27.5 \times 25.5 \times 10.5$  cm<sup>3</sup>, linked with the ion source assembly for its support and alignment. It is pumped with a six inch type (EO6) oil diffusion pump DPI, with a water-cooled chevron baffle to prevent the backstreaming of the pump oil. It has three ports, one for the roughing line, the second for pressure monitoring and the third spare- to be used, for example for the insertion of a retractable Faraday cup.

The diffusion pump is backed by a single stage oil filled rotary pump type ED 660 to obtain a pressure of the order of  $\sim 10^{-3}$  torr.

With the source off, a pressure of  $\sim 10^{-7}$  torr was attainable in the rectangular tank. A detectable effect on the pressure inside the tank was observed with the ion beam on. A higher pressure of  $5 \times 10^{-6}$  torr was recorded in this case. A better pressure of the order of  $5 \times 10^{-7}$  torr resulted when the temperature of the caesium charge-exchange cell was reduced from  $110^{\circ}\text{C}$  to  $90^{\circ}\text{C}$ .

#### UHV CHAMBERS I & II

These are identical 8 inch UHV crosspieces bolted together and pumped by 6 inch EC6 diffusion pumps with thermo-electric and water cooled chevron baffles respectively. An ultimate pressure of  $\sim 10^{-8}$  torr could be achieved in 24 hours. Backing was provided by an ISC 450B double-stage oil filled rotary pump. Santovac 5 pumping fluid is used throughout because of its exceptional high vacuum performance, in particular, its chemical and thermal stability, its extremely low vapour pressure ( $2 \times 10^{-10}$  torr at  $20^{\circ}\text{C}$ ) and its breakdown products being electrically conducting.

Bolted to the end of tank VCI is the magnet tank with a short beam line attached, pumped via tank VCII.

A combination of copper and rubber gaskets are used to seal the chambers and each chamber has an ion gauge head with thorium coated iridium filament (non-burn-out) and a measuring range of  $10^{-2}$  to  $10^{10}$  torr.

#### **§3.4 QUENCHING ARRANGEMENT**

Positive ions (deuterons), metastables and ground state neutrals are the main components of the beam after having left the caesium charge-exchange

cell. The singles background due to deuterons is usually too large to be coped with by the electronics system. Hence, in order to monitor this background, a system consisting of a set of four plates, two inner and two outer shown in the Fig.3.1, was designed similar to that of Spiess et al [72]. It was fitted through the top flange of UHVI chamber adjacent to the beam exit from the charge-exchange cell. Keeping in view the limitations of the physical space in the UHVI chamber and other constraints, the dimensions of  $31 \times 65 \text{ mm}^2$  for a pair of inner plates separated by 40 mm, was found to be the most suitable choice.

The electric field, due to a voltage of  $\pm 200 \text{ V}$  applied across these plates, was strong enough to quench the metastable flux  $> 99.9\%$  before entering the detection region. But we did not make use of these pre-quench plates to monitor the background, instead we preferred to close the gate-valve on either side of the charge-exchange cell. By doing so, we reduced the background noise and consequent error as discussed in §4.6 of chapter IV.

Another set of four plates, having dimensions one third of the pre-quench plates described above were used in UHVII chamber. In this case a constant voltage of  $\pm 200 \text{ V}$  was supplied across them to quench the metastables to obtain Lyman-alpha radiation which was monitored by a Lyman-alpha photomultiplier to give a measurement of the metastable beam flux (see section 3.6.1).

### §3.5: NEUTRAL BEAM DETECTOR

The neutral beam detector consists of a Faraday cup, with a guard ring and a 90% transparency tungsten wire mesh over the cup entrance. With the

guard ring and mesh biased negatively, the cup operates as an electron-suppressed Faraday cup, to measure the charge component of the beam. With the charged component of the beam deflected by the quench field, and a positive potential on the guard ring and mesh, it measures the neutral component of the beam. In this latter case the secondary electrons, emitted by the neutrals striking the surface, are accelerated out of the cup through the positively biased grounded mesh. The positive current flowing from the detector can then be used to measure the neutral current provided the secondary electron emission coefficient is known. Prodel et al [73] found the same value 1.7 for the coefficient at a beam energy of 1 keV for both metastables and ground state neutrals.

### §3.6 PHOTOMULTIPLIER TUBE

Keeping in consideration the spectral response and time resolution required, we made use of the photomultipliers, type 9883 QA and 9883 QB previously selected for the experiment of Perrie et al [24]). These tubes were fast linearly focused types chosen for timing applications with an output pulse rise time of 2.2 ns and a gain of  $3 \times 10^6$ . The spectral sensitivity of the bi-alkali photocathodes was in the range from 180 nm to 600 nm and the quantum efficiency  $\eta=28\%$  at  $\lambda=420$  nm. The dark count rate of these photomultipliers was found to be about  $40 \text{ sec}^{-1}$  (9883 QA) and  $150 \text{ sec}^{-1}$  (9883 QB) respectively.

In order to avoid voltage gradients across the photomultiplier window, both the photomultipliers with their cathodes were operated at ground potential. Any electric field may introduce some sensitivity to polarization in the

photomultiplier windows.

### 3.6.1: LYMAN-ALPHA PHOTOMULTIPLIER

In order to monitor the  $I_{\alpha}$  radiation ( $\lambda = 121.6$  nm), a photomultiplier tube, obtained from EMI, type G-08-18, having spectral response in the range of from 105 nm to 220 nm, was used in conjunction with a LiF window coupled to a slow shaping amplifier (NE 4603) and integral discriminator (NE 4623). The discriminator output is fed to a ratemeter and two scalars. One of these scalars monitors the metastable beam, the other the background. An electrometer (type, Keithly, Model 610 C) was used to measure the output from the neutral detector.

To produce a filter for  $I_{\alpha}$  photons, dry O<sub>2</sub> was allowed to flow between the LiF vacuum window and the photo-multiplier tube. The above mentioned LiF window was covered by an aperture of 3 mm diameter to reduce the count rate to an acceptable level.

### §3.7 PILE OF PLATES POLARIZERS

To achieve a degree of polarization, the two polarizers, used in the experiment of Perrie et al [24], were re-employed in the present experiment. They were pile-of-plates polarizers consisting of 12 fused silica suprasil plates having a short wavelength cut off at 160 nm. The dimension of each plate was 100 x 160 x 2 mm<sup>3</sup>. The plates were set at the Brewster angle  $\theta_B = 56.31^\circ$  to the incident light of wavelength  $\lambda = 243$  nm. The plates were stacked in two complementary groups of six plates to cancel transverse ray displacements. Surface scattering effects of these plates are minimised by polishing them to

$2\lambda$  per face at  $\lambda = 243$  nm.

Fig.3.4 [74] shows the reflection coefficient for the transverse magnetic mode (TM) i.e the mode in which B-field vector is perpendicular to the plane of incidence and E-field vector is parallel to the plane of incidence (also known as p-component) and TE (transverse electric mode) mode in which E-field vector is perpendicular to the plane of incidence (also known as s-component). These reflection coefficients are determined from the Fresnel equations[74]. Negative values of the reflection coefficient for both the TE and TM modes indicate a phase change in the E and B vectors on reflection.

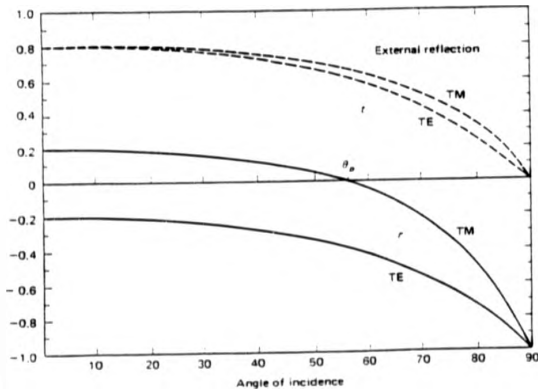
The fraction of power P in the incident wave that is reflected or transmitted, called the reflectance and transmittance respectively, depends upon the ratio of the squares of the amplitudes, given by

Reflectance:TE mode(s-comp)

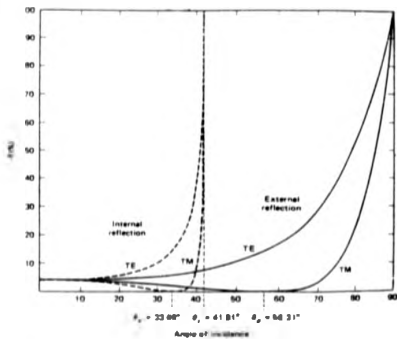
$$R_s = r^2 = \left( \frac{E_R}{E} \right)^2 = \left( \frac{\cos\theta - \sqrt{n^2 - \sin^2\theta}}{\cos\theta + \sqrt{n^2 - \sin^2\theta}} \right)^2 \quad (3-2)$$

Transmittance:TE mode

$$T_s = 1 - R_s = \left( \frac{2\cos\theta}{\cos\theta + \sqrt{(n^2 - \sin^2\theta)}} \right)^2 \quad (3-3)$$



Fig(3.4). Reflection( $r$ ) and transmission( $t$ ) coefficients for the case of external reflection, with  $n = n_1/n_2 = 1.50$



Fig(3.5) Reflectance for both external and internal reflection when  $n=1$  and  $n=1.50$ .

Reflectance: TM (mode) i.e( p-component)

$$R_p = \left( \frac{n^2 \cos \theta - \sqrt{n^2 - \sin^2 \theta}}{n^2 \cos \theta + \sqrt{n^2 - \sin^2 \theta}} \right)^2 \quad (3-4)$$

Transmittance: TM (mode)

$$T_p = 1 - R_p = \left( \frac{2n \cos \theta}{n^2 \cos \theta + \sqrt{n^2 - \sin^2 \theta}} \right)^2 \quad (3-5)$$

Fig.3.5 shows the reflectance for both external and internal reflection when  $n_1=1$  and  $n_2=1.5$ . The curve for the case of external reflection, TM mode(p-comp), indicates that no wave energy is reflected when the angle of incidence is near  $60^\circ$ . More precisely  $R_{TM}=0$  when  $\theta = \tan^{-1} n = \theta_B$ , the Brewster angle.  $R_{TM}$  does not go to zero under this condition, so that the reflected light contains only the TE mode and is linearly polarized with  $R_{TE} = 15\%$ .

For normal incidence ( $\theta=0$ ), the reflectance for the TE mode (s-comp) is given by

$$R_s = \left( \frac{1-n}{1+n} \right)^2 \quad (3-6)$$

suggesting that the higher the refractive index  $n$ , the higher is the reflectance and hence fewer plates would be required to achieve a reasonable degree of polarization. Repeated reflections by multiple layers of the dielectric at Brewster's angle both increases the intensity of TE (s-comp) reflection and

necessarily, purifies the transmitted beam.

The Airy expressions [75] for the Reflection and Transmittance for the TE mode are given by

$$R_s = \frac{(n^2 - 1)^2}{(n^2 + 1)^2} ; T_s = \frac{2n^2}{(n^2 + 1)^2}$$

(3-7)

Transmission through a single plate of suprasil ( $n=1.54$  at  $\lambda = 243$  nm) for TE mode is given by

$$T_s = \frac{2(1.511)^2}{(1.511)^4 + 1} = 0.735$$

(3-8)

Therefore, transmission through  $m$  plates =  $(T_s)^m = (0.735)^m$ .

To reduce the TE component to less than 5 %, we need  $m > 10$ . Therefore we chose 12 plates for which  $T_s^{12} = (0.735)^{12} = 0.025$  thereby giving us the degree of polarization

$$P = \frac{1 - T_s^{12}}{1 + T_s^{12}} = 0.95$$

(3-9)

Although multiple reflection between plates can occur, diverting a proportion of the unwanted radiation back into the transmitted beam and thus reducing the expected polarization. Conn and Eaton [75] have shown that no significance reduction in the TM component would be expected provided only

a small number of such rays reach the detector. Polarization as high as 99.7% has been claimed for an experimentally produced polarizer due to Conn and Eaton[75]. Up to 96% polarization is claimed for a unit produced commercially by Hilger and Watts, Ltd.

### §3.8. TRANSMITTANCES OF THE LINEAR POLARIZERS

In order to compare the experimental results with theory, it was necessary to know the values of the transmission efficiencies  $\epsilon_M$  and  $\epsilon_m$  for light polarized, respectively, parallel and perpendicular to the transmission axes of the polarizers and these quantities have been measured in the past experiments [14,24] in a subsidiary experiment, making use of the 254-nm line from a mercury lamp. In this experiment, using the apparatus as shown in Fig. 3.6, the photomultiplier was removed from one arm and an almost parallel beam of polarized light was passed through the piles-of-plates polarizer (aligned with its transmission axes parallel to the plane of polarization of the light from the mercury source) to come to a focus at the position normally occupied by the centre of the atomic source. The light emerging from this focus was then analyzed by the pile-of-plates polarizer and photomultiplier in the other detection arm. After application of a small correction to take into account the slight absorption in the fused silica between 185 and 200 nm. It was found that for the two polarizers used here.

$$\epsilon_M = 0.908 \pm 0.013 \quad \text{and} \quad \epsilon_m = 0.0299 \pm 0.0020$$

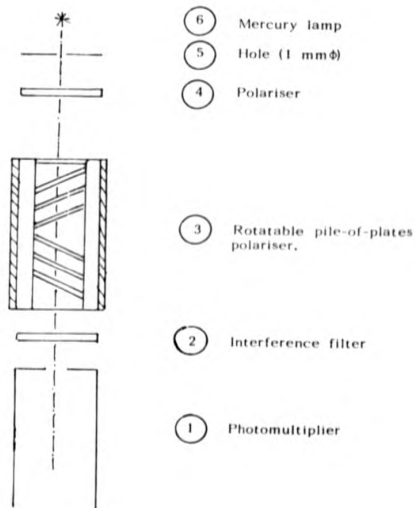


Fig3.6.Experimental set up for the calibration of the polarizer.

### §3.9:RETARDERS

Half-wave plates (HWP) and quarter-wave plates (QWP), achromatic over the spectral range of from 185 nm to 300 nm, and four special non-achromatic half-wave plates at wavelengths  $\lambda=486$  nm, 300 nm, 243 nm and 200 nm, (zero-order doublets), each having thickness  $d=2$  mm, were used in the experiment in conjunction with the pile of plates polarizers. These retarders, each of 30 mm aperture, were obtained from Gooch and Housego Limited Cornhill Ilminster Somerset, England. A detailed description and working of retarders is given in §2.8 of chapter II and the procedure for the choice of the above mentioned half-wave plates used as depolarizers is described in §4.10 of chapter IV. Special cylindrical mounts of aluminium and copper were designed to hold these retarders. These mounts fitted very well into the fronts of the polarizers and UHV I chamber. The relative angle between the fast axis of retarder and transmission axis of the polarizer could be set with the aid of a plastic graduated scale fixed at the supporting end of the polarizer.

### §3.10 SYMMETRICAL OPTICAL SYSTEM

The optical system, for ultra-violet(UV)light,comprises of the following components:

- Two photomultipliers (section §3.6)
- Two pile-of-plates polarizers (section §3.7)
- Two bi-convex lenses(suprasil) each of focal length 50 mm,refractive index  $n(\lambda)=1.4585$  at  $\lambda =587.6$  nm.

- Two glass vacuum windows(suprasil) each of diameter 50 mm,thickness =5 mm.
- Vacuum system(section §3.3)
- Optical benches and holders

In the UHVI chamber, on each side of the atomic beam the radiation passes through the suprasil window which is followed by a suprasil bi-convex lens, which focuses the light through a pile-of-plates polarizer, forming a magnified image at the photomultiplier cathode as shown in the Fig.3.6. Special mounts were prepared for holding the windows, providing an easy and manageable access for fitting them on to the interior end (~ 25 mm from the atomic beam line) of the snout of UHVI. The other end of the snout supports one end of the polarizer on a tight fitting rotatable teflon bearing. The photomultiplier and polarizer were supported on the optical benches coupled together by a light tight aluminium bearing. The optical benches were aligned,positioned and supported on 2 m long aluminium table bolted at right angles to the main framework of the experiment. The alignment of lenses and windows is discussed in section §4.4 of Chapter IV.

### §3.11 SYSTEM INTERLOCK

To protect the various systems and components involved in the project from any damage especially the ion source due to a failure of the vacuum, water cooling for diffusion pumps, high voltage and mains power supply, an interlock system, designed by Perrie et al [24] was installed with the experiment.

### §3.12: COINCIDENCE ELECTRONICS

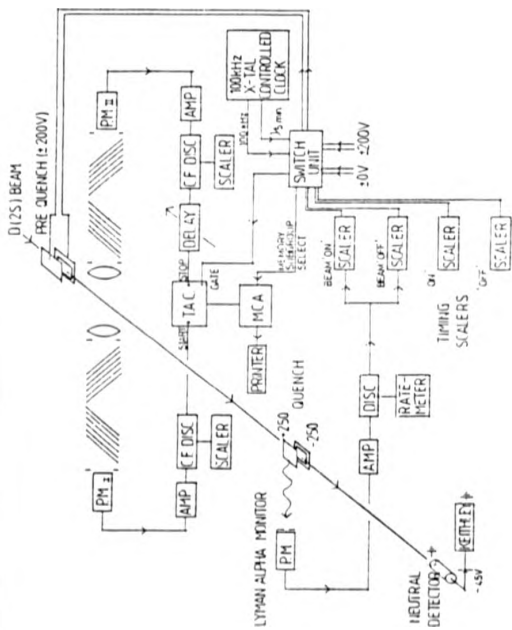
The best possible practical timing resolution was achieved by designing a coincidence electronic system comprising of fast amplifiers, discriminators, a time-to-amplitude converter (TAC), scalars, pulse stretcher and multichannel analyzer (MCA). A schematic diagram of the system is shown in Fig.3.7. Throughout, matched 50  $\Omega$  cables were used and great care was taken to match the photomultiplier anodes to the cables. In spite of the fact that dc coupled amplifiers and discriminators were used, it was felt desirable to operate the photocathodes at ground potential to avoid stray electric fields in the detection region. In consequence, photomultiplier anodes had to be ac coupled, however no evidence for pulse pile up on the blocking capacitors was observed.

Initial operation of the detection system gave rise to a number of spurious coincidence peaks, but most of these were discovered to be either cross-talk between the coincidence channels, or electrical pick up. A small spurious coincidence peak was still observed in spite of the elimination of the above mentioned effects. After a number of tests this peak was ascribed to cosmic rays or possibly radioactive decay induced fluorescence in the fused quartz components. Similar effects have been observed by Novick [76], King et al [77], O'Connell et al [47], Perri et al [24], Haji-Hassan et al [14].

In order to compensate for this effect in previous experiments, the metastable beam was modulated by a dc electric quenching field while synchronously switching the detection system. It did help to eliminate the spurious effect, but the measuring period was almost doubled in this exercise.

In the present set of experiments this was achieved by closing the gate valve in front of the beam exit.

The anode pulses from the coincidence photomultipliers were amplified by a factor of 10 in fast amplifiers, (LRS 333;234) having rise time of 2 ns. The output pulses were fed to constant fraction differential discriminators, (ORTEC, Model 583;463). One of the discriminator outputs is taken directly to the start input of a TAC (NE 4670), while the other is taken through a gate and delay generator(ORTEC 416 A) to the stop input. In the NE 4670 TAC, the time interval between the arrival of a START and the next STOP input is converted to an output voltage, the amplitude of which is directly proportional to the time interval. The output pulses from the TAC are taken to the input of the pulse stretcher (ORTEC, model 411) whose output is connected to the MCA (Canberra 8000) to record the resulting pulse height spectrum from the TAC. This spectrum consists of true coincidences (in which the two photons originate from the same excited H atom) and random coincidences (where the two photons have no common origin). The true coincidences form a peak on top of a background of coincidences. The time spectra for the metastable beam **ON** and **QUENCHED or BLOCKED (by closing the gate valve)** are stored separately into the eight compartments of the MCA memory. The outputs of the timing discriminators are coupled to fast scalars which monitor the integrated single counts. The discriminator level for each of the photon channel are adjusted to a suitable level(30-50 mV for each channel) in order to discriminate against the noise without affecting the real signal.



Fig(3.7) Schematic diagram of the detection system.

## CHAPTER IV

### EXPERIMENTAL PROCEDURE & TECHNIQUES

#### §4. INTRODUCTION

Experimental data is an important aspect of the experimental work which should be analyzed with great care for the extraction of useful information concerning the physical quantity of interest e.g., coherence length of the photon etc. Therefore, in this chapter, we describe some experimental techniques employed in our experimental work, for reducing the background radiation, improving the statistical accuracy of measurements, optimizing the signal, achieving the required optical alignment and the coincidence techniques for the analyzing of data.

A detailed procedure, for the process of selecting various non-achromatic retarders (depolarizers) employed in the experiment, is also described along with the experimental procedure of checking their optic axis and retardation values.

#### §4.1: BACKGROUND RADIATION

Beam surface collisions in the chamber UHV 1 (Fig.3.1), were found to be mainly responsible for the random background or noise. These radiations were critically dependent on slight changes in the operating conditions of the source. On the other hand the pressure dependence of the background was found to be negligible. It was noted that with the caesium cell off, the resulting ion beam produced background rates of an order of magnitude lower than

with the neutral atomic beam present. Hence the random background due to the remaining small ionic component in the "neutral beam" constitutes  $< 1$  percent of the total random background. The level of background radiation in the detection region due to beam surface collision etc, was reduced with the aid of a shield consisting of a cylindrical aluminium "can" with 15 & 20 cm diameter holes for the passage of the atomic beam which is first passed through 15 cm diameter hole and then through 20 cm diameter hole to avoid direct collision. This "can" can slide neatly over the stainless inserts in the detection region and was carefully aligned with the 1 cm diameter apertures on the pre-quench plates. Its internal surfaces were sooted to reduce reflections. Also, very importantly, the shield was effective in preventing the contamination of the vacuum windows with caesium emanating from the ends of the charge-exchange cell. The Balmer  $\beta$ -line was the main component of the background radiation (observed through an optical spectrometer). Because of the very low sensitivity of the photomultipliers at  $\lambda=486.1$  nm, they were insensitive to the Balmer  $\beta$  line, thereby, helping in reducing the background. The sensitivity of the photo-multiplier extends from 120 nm to 355 nm.

A small reduction of caesium temperature was found to be advantageous not only in minimising background (without losing signal) but also in improving pressure. Pressure in the rectangular tank was improved from  $3 \times 10^{-6}$  to  $3 \times 10^{-7}$  torr by reducing the temperature of the caesium oven from  $110^{\circ}\text{C}$  to  $90^{\circ}\text{C}$ . There is however, a possibility that the temperature within the interior of the caesium oven may be more than the one which is

recorded from its outer surface through the thermocouple. A high temperature in the caesium oven might be the cause for more thermal radiation to be emitted from the surface of the oven thereby increasing the background. But it is very unlikely because of the fact that our photomultipliers are insensitive to infra-red radiations. For a defocussed neutral beam of 8 nA, the singles rate of the photo-multiplier tube 9883 QA was higher (4.4kHz) than that of 9883QB (1.7kHz).

#### §4.2: METASTABLE ATOMIC BEAM OF DEUTERIUM

A method proposed by Donnally [78] et al in 1974, is used to produce a dense beam of metastable atomic deuterium at a low energy using the nearly resonant process of charge-exchange of protons in caesium vapour



An investigation made by Massey [79] showed that the cross sections were large at low energies, provided the energy deficit for the charge exchange process was small. This has since been verified in a number of experiments.

The maximum cross section was found to be at  $E = 600$  eV and is independent of thickness of the caesium target. This fact was established by Pradel [80] et al. We used the near resonant charge exchange process because it ensures a large cross section at a low energy and hence high beam density which was the requirement of the experiment since the rate of two-photon emission from a metastable beam at a fixed detector location is proportional to the metastable density.

## Mass analysis of ion beam

Extracted from RF ion source

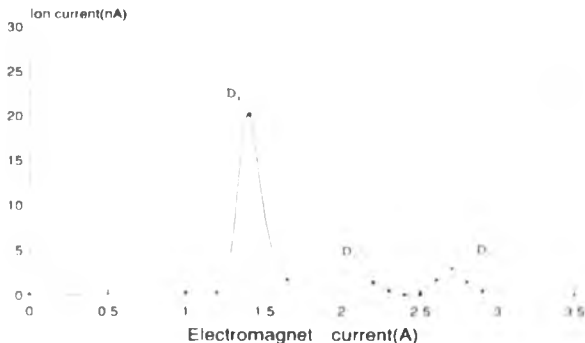


Fig 4.1 Mass analysis of the beam

### §4.3: BEAM ANALYSIS BY A MAGNET

A standard C-type electromagnet, situated at the end of the apparatus, capable of producing a magnetic field  $B=0.5T$ , is used to analyze the beam components ( $D_1^+$ ,  $D_2^+$ ,  $D_3^+$  ions). These ions, deflected at  $30^\circ$  are collimated by a 4 mm aperture at the entrance of the magnet tank. Shortly after starting the source it is possible to obtain a deuteron fraction  $f_D = 0.75$  as shown in Fig 4.1. With continuous operation of the discharge over a long period (several days/weeks) this fraction increases to  $f_D = 0.9$ . During the process of checking

the deuteron fraction, some magnetic hysteresis is developed in the magnet and this affects the total beam current observed. Care has to be taken to eliminate the residual magnetic field in it. Reversing the connections to the magnet restores the total beam current.

#### §4.4: ALIGNMENT OF THE OPTICAL SYSTEM

Alignment of the optical system (described in §3.10) was achieved using a He-Ne laser (Scientific & Cook Electronics, class 3B, Max. output 5 mW) and hand made hard-paper discs with a central pin hole which were cut according to the size of snout's aperture ( $\Phi=59$  mm) and those of the optical holders ( $\Phi=36$  mm). The latter were capable of sliding smoothly on the optical benches provided for the optical system. The laser beam was adjusted to pass through the centres of the vacuum optical window and collecting lens after getting it aligned through the pin holes lying in between the vacuum optical window and laser. Lateral displacement of 2 mm was found between the parallel optical benches of the optical system. Special mounts of aluminium metal were prepared for holding the windows to fit tightly around the aperture in the detection region. Provision was also made on these aluminium mounts to hold the mounts, made of teflon, for lenses without disturbing the positions of the windows. The lenses are positioned with their focal points close to the centre of the interaction region in order to produce a nearly parallel beam of light. With great care and patience, the alignment was achieved by adjusting the screws provided on the lenses mounts. To do it conveniently, some pieces of packing material were slotted into the space surrounding the lenses for the

fine adjustment of the screws on lens mounts. Alignment of the optical system was confirmed by performing the following two simple experiments.

(i) Two cylindrical aluminium inserts, with concentric pin poles, were fitted tight into the entrances of the detection chambers. These pre-aligned entrances are located opposite to each other across the detection chambers. A thin steel wire was made to pass through the pin holes of these inserts and was kept stretched. In this way, the stretched wire passes through the centre of the detection region and is symmetrically located with respect the lenses and windows on its either side. By shining light (from an electric bulb) from the top flange position of the detection chamber, the image of the wire was observed on a screen which was pre-aligned with the centre of the lens. By contacting the stretched wire at the two extremes of the verticle diameter of the pin holes through which it is passing, the two images of the wire are obtained on the screen. They were found to be symmetrical and equidistant from the centre of the screen, thereby confirming the optical alignment.

(ii) A second check was made using the same stretched wire as described above but this time we sent the two light beams, from either side of the optical system, through the lenses and windows. The two light beams were aligned with the centres of the snouts of the optical system. It was observed that the two beams struck the stretched wire, in the detection region, exactly at the same spot, thereby, giving us another confirmation of the optical alignment.

### §4.5 COINCIDENCE TECHNIQUE

The coincidence technique has been used in experimental physics for more than two decades. It was first developed in nuclear physics by Brannen (1955) and then extended into the fields of atomic and molecular physics. There are four kinds of delayed coincidence techniques namely,

- (i) Photon-photon coincidence
- (ii) Electron-photon coincidence
- (iii) Electron-electron coincidence
- (iv) Electron-ion-photon coincidence

but for our experiment we shall be using the photon-photon coincidence which is described in the following paragraph.

#### 4.5.1: Photon-photon coincidence

The basic principle of this technique is to excite the atom or molecule in some way and then observe the emission of two photons. One photon is used to start and one to stop the timing device. By observing the delayed coincidence between the start and stop pulses, a time spectrum is obtained from which the lifetime of the intermediate state can be obtained. Such measurements have been made by Imhof and Read (1977). The photon-photon coincidence technique was first used by Brannen et al (1955) to measure the lifetime of the  $7^2S_1$  state of mercury. It has since been used by many workers for the life time measurements of atoms and molecules (Kaul 1966 [81], Popp et al 1970 [82], Holt & Pipkin 1974 [83] and King et al 1975-76) [84].

The following method was used to calculate the number of true

coincidence counts and the error in them. Fig 4.2 shows a schematic diagram of the coincidence spectrum in the MCA. It is divided into three regions ( $x_2-x_1$ ), ( $x_3-x_2$ ), and ( $x_4-x_3$ ), with corresponding coincidence counts  $N_1$ ,  $N_2$ ,  $N_3$ , where,  $N_1$  and  $N_3$  are related to the chance coincidence events.

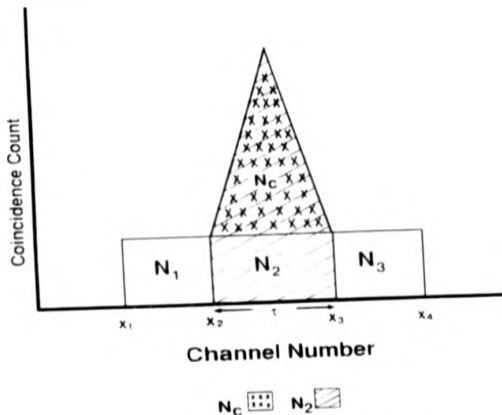


Fig 4.2. Data acquisition for coincidence analysis.

The number of random coincidences  $B$  under the coincidence peak is given by

$$B = \frac{(N_1 + N_3)(x_3 - x_2)}{(x_2 - x_1) + (x_4 - x_3)}$$

(4-2)

The number of true/real coincidences,  $N_r$ , is

$$N_r = N_2 - B \quad (4-3)$$

The error  $\delta N_r$  (standard deviation) of the number of real coincidences is given by

$$\delta N_r = \sqrt{N_2 + \left[ \frac{(x_3 - x_2)^2}{(x_2 - x_1) + (x_4 - x_1)} \right]^2 (N_1 + N_2)} \quad (4-4)$$

The number  $N_r$  and  $\delta N_r$  are normalized to the total number of  $L_{\alpha}$ -photons collected during each run so that the effects of fluctuations of the neutral beam current, and the target density are largely eliminated. The resulting values of  $N_r/L_{\alpha}$  and  $\delta N_r/L_{\alpha}$  are used to measure the Stokes parameters in the polarization correlation measurements.

#### §4.6. COSMIC RAYS COINCIDENCE RATE

The spurious coincidences, presumably due to cosmic rays (CR), radioactivity and electrical pick up, arrive at a constant average rate, depending on the geometry and sensitivity of the detection system. This rate was about  $1.6 \times 10^3 \text{ sec}^{-1}$  (5.8 hr<sup>-1</sup>), and gives rise to relatively large peaks in the coincidence spectra for the pre-quenched state of the beam. It has been the practice in the past to determine the CR coincidence rate by quenching the beam to remove the metastables before it enters the detection region. But here, the CR coincidence rate was determined by closing the gate valve in front of the beam so that there was no beam in the detection region. This method [85] was beneficial in reducing the statistical error as shown below.

#### 4.6.1. Pre-quench field method with beam present

##### (i) Pre-quench field "OFF"

With the prequench field off, the statistical error in the number of true coincidences which includes those due to two-photon decay and cosmic rays etc, is given by

$$\delta N_T = \pm \sqrt{N_2 + (N_1 + N_3) \Delta^2}, \quad (4-5)$$

where,

$$\Delta = \frac{(X_3 - X_2)}{(X_2 - X_1) + (X_4 - X_1)}$$

To a good approximation, the eq. 4-5 can be written as

$$\delta N_T = \pm \sqrt{N_2}$$

since in practice

$$(N_1 + N_3) \Delta^2 \ll N_2$$

##### (ii) Pre-quench field ON

The statistical error, in the CR coincidence rate with the prequench field ON, is given by

$$\delta N_2' = \pm \sqrt{N_2' + (N_1 + N_1') \Delta^2} = \pm \sqrt{N_2'} \quad (4-6)$$

where  $N_2'$  are the true CR coincidences and the 2nd term in eq.(4-6) has been dropped for the reason stated above.

In order to determine the real two-photon coincidences due to two-photon decay, CR coincidences are subtracted from the total coincidences. Hence the standard deviation  $\delta N_2(2\gamma)$  will be given by

$$\delta N_2(2\gamma) = \pm \sqrt{N_2 + N_2'} \quad (4-7)$$

#### 4.6.2: Closing gate valve method

By closing the gate valve, not only do we block the background but also we reduce the error in measuring the contribution of the cosmic rays to the coincidence signal. This will now be given by

$$\delta N_2'' = \pm \sqrt{N_2'' + (N_1'' + N_1'') \Delta^2} = \pm \sqrt{N_2''} \quad (4-8)$$

where  $N_2''$  are the true CR coincidences, and the 2nd term in eq.(4-8) is dropped. Thus the error in the true  $2\gamma$  coincidences will be then given by (combining eqs.4-5 & 4-8)

$$\delta N_2(2\gamma) = \pm \sqrt{N_2 + N_2''} = \pm \sqrt{N_2} \quad (4-9)$$

since  $N_2' \ll N_2$ . The comparison of the eq.(4-9) with eq.(4-7) suggests that the error will be more with the **prequench field ON** procedure than the **closing of the gate valve** method simply because of the fact that  $(N_2 + N_2')$  in eq.(4-7) is much larger than  $N_2$  in the eq.(4-9). It is for this reason we adopted the closing gate valve method. However, this method is based on the assumption that only cosmic rays etc contribute to the spurious real coincidence signal and there is no contribution due to the presence of the beam itself.

#### §4.7: SIGNAL OPTIMISATION

In addition to the knowledge of the spectral range over which a particular detector is effective, it is important to know the actual sensitivity or more precisely, the responsivity  $S$  of the detector, defined as the ratio of the output to input:

$$S = \text{output/input} \quad (4-10)$$

Input may be the radiant flux or irradiance, output is always a current or voltage. For the responsivity to be a useful specification of a detector, it should be constant over the useful range of the instrument. In other words, the detector, with its associated amplifier and circuits, should provide a linear response, with output proportional to input. In general, however, responsivity is not independent of wavelength. When responsivity is a function of wavelength  $\lambda$ , the detector is said to be selective (in our experiment, both the detectors, 9883 QB and 9883 QA, were selective). A non-selective detector is one that depends only on the radiant flux, not on the wavelength.

The detectivity  $D$  of a detector is the reciprocal of the minimum detectable

power, called the **NOISE equivalent power**  $\phi_n$  of the detector:

$$D = 1/\phi_n \quad (4-11)$$

The minimum detectable power  $\phi_n$  is limited by the noise inherent in the operation of the detector. **The NOISE is that part of the signal or output not related to the desired output.** Many sources of NOISE exist, including the statistical fluctuations of photons or **radiation noise**, and the thermal agitation of current carriers, or **Johnson noise**, inherent in all detectors; the generation and recombination noise due to statistical fluctuation of current carriers in photoconductors; the **shot noise** due to random emission of electrons in photoemissive detectors; and the noise due to temperature fluctuations in thermal detectors. Mere amplification of a signal is not useful when it does not distinguish between **SIGNAL** and **NOISE** and results in the same signal-to-noise ratio. The signal-to-noise (S/N) ratio was optimized by controlling the singles rate ( $N_1$ ), without much loss of signal by adjusting the focusing conditions of the beam[85].

If  $N_1$ ,  $N_2$  are the singles rates for the two detectors and  $N_c$  is the two-photon decay rate, then the total number of two-photon coincidences in the coincidence window of time  $\tau$  is given by

$$N_c = N_1 T + N_2 N_1 \tau T = N_1 N_2 \tau T$$

(4-12)

where  $T$  is the total counting time

The error in  $N_c$  (total no. of two-photon coincidences) is given by (see

section §4.5 & Fig.4.2)

$$\delta N_c = \sqrt{N_2 + (N_1 + N_3) \left[ \frac{(X_3 - X_2)}{(X_2 - X_1) + (X_4 - X_3)} \right]^2} = \sqrt{N_2} = \sqrt{N_1 N_2 \tau T} \quad (4-13)$$

since under normal circumstances  $\dot{N}_c \ll \dot{N}_1, \dot{N}_2, \tau T$ .

In the above equation we have dropped the factor given by

$$\frac{(N_1 + N_3) (X_3 - X_2)}{(X_2 - X_1) + (X_4 - X_3)} \quad \text{being}$$

a very small number as compared to  $N_2$ . Since  $\dot{N}_1 = \dot{N}_2$ , the eq.(4-13) can be rewritten as

$$\delta N_c = N_1 \sqrt{\tau T}$$

Thus we can write the fractional error in  $N_c$  as

$$\frac{\delta N_c}{N_c} = \frac{\dot{N}_1}{\dot{N}_c} \sqrt{\frac{\tau}{T}} \quad (4-14)$$

The above equation suggests that if  $\dot{N}_1$  and  $\dot{N}_c$  are changed in the same ratio, then the percentage error in the two photon decay rate  $\dot{N}_c$  is unchanged. Hence defocusing the beam, in an attempt to reduce the singles rate, was helpful in optimizing signal provided the other parameters remain unchanged even although the two-photon signal resulting from the two-photon decay was also reduced.

#### §4.8: MEASUREMENT METHOD

In order to achieve an acceptable statistical accuracy, all the coincidence runs were almost of 24 hours duration. All the parameters, such as the beam energy, the neutral current, focusing conditions, integrated  $I_{\alpha}$  counts, the oxygen flow rate to the  $I_{\alpha}$  monitor, pressure in the rectangular tank UHV I, Cs temperature, singles rate from the coincidence photomultipliers; were carefully monitored throughout each run to check and rectify any drifts.

#### §4.9: NORMALIZATION PROCEDURE

Since the strength of the signal was very much dependent on the metastable density, therefore, the variations from run to run were taken care of by the normalization procedure according to which the coincidence rate of each run is to be divided by the total number of  $I_{\alpha}$  photons recorded for that particular run.

#### §4.10: CHOICE OF RETARDERS

The following steps were taken in selecting quartz retarders of various wavelengths tabulated in Table 4-2.

- (i) The variation of birefringence ( $n_e - n_o$ ) of quartz material versus wavelength  $\lambda$  in the range from 185 nm to 355 nm was recorded on a graph Fig. 4.3 using Table 4-1 taken from the Handbook of Optics [86]. The variation of birefringence is shown also in the fourth column of Table 4-6.
- (ii) The thicknesses  $d$  of zero-order retarders (shown in Table 4-2) were calculated by using the retardation formula,  $\phi = (n_e - n_o)2\pi d / \lambda$ , described already in section §2.9; eq(2-75).

(iii) The wavelength variation of the transmission efficiencies  $\epsilon_m, \epsilon_n$  of the polarizers previously calculated by Haji-Hassan etc [14] is shown in Fig.4.5 and the spectral distribution  $A(\lambda)$  of two-photon emission versus wavelength  $\lambda$  is shown in Fig.4.4 using Table 4-3 taken from Spitzer and Greenstein [87]. The variation of the degree of polarization  $\Pi = (\epsilon_m - \epsilon_n) / (\epsilon_m + \epsilon_n)$  and spectral distribution  $A(\lambda)$  are shown in Table 4-4. From Fig.4.4, we can calculate the area

$$\int_{185}^{355} A(\lambda) d\lambda$$

which represents the spectral distribution of two photons in the range from 185 nm to 355 nm.

(iv) The Stokes parameters,  $(P_1 = \cos\phi; P_2 = 0; P_3 = -\sin\phi)$ , derived in section §2.9 eq.(2-86), were found for the spectral range of from 185 nm to 355 nm. These values have been tabulated in Tables (4-5 to 4-8) for the thicknesses of the retarders tabulated in Table 4-2. The above mentioned Stokes' parameters  $P_1, P_2, P_3$  were derived under the assumption that the polarizers were perfect, but in practice they are not. With imperfect linear polarizers, the Stokes' parameters are  $P_1', P_2', P_3'$  derived in section §2.5 i.e

$$P_1' = \Pi P_1; P_2' = \Pi P_2; P_3' = \Pi P_3$$

These Stokes parameters were calculated using Tables 4-5 to 4-8. Figs 4-6-4-9 show the corresponding graphs between these Stokes' parameters and wavelength.

(v) The average values of these Stokes' parameters  $P_i(\lambda)$  ( $i=1,2,3$ ) were actually calculated from these graphs for the range from 185 nm to 355 nm and they are shown in Table 4-9 along with the expected total polarization  $P_{tot}$  for the chosen depolarizers.

The average values of these Stokes parameters are quite sensitive to the spectral distribution  $A(\lambda)$  of the two photons and the transmission efficiencies of the polarizers, these were actually calculated and are shown under the columns labelled  $P_i$ ,  $P_i(A)$ ,  $P_i(AI)$  respectively in Table 4-9a.  $P_i$  ( $i=1,2,3$ ) represent the Stokes' parameters without taking into consideration the spectral distribution and imperfection of the polarizers,  $P_i(A)$  ( $i=1,2,3$ ) represents the Stokes' parameters by taking into consideration only the spectral distribution and  $P_i(AI)$  ( $i=1,2,3$ ) represent the Stokes' parameters taking into consideration both the spectral distribution and imperfection of the polarizers. The average values of  $P_i(\lambda)$  were calculated through the formula

$$\overline{P_i}(\lambda) = \frac{\int_{\lambda_1=185}^{\lambda_2=355} P_i(\lambda) A(\lambda) d\lambda}{\int_{\lambda_1=185}^{\lambda_2=355} A(\lambda) d\lambda}$$

(4-15)

where  $A(\lambda)$  is the spectral distribution of two photons and  $P_i(\lambda)$  is the Stokes' parameter calculated for a particular retarder.

The authenticity of the above formula (4-15) can be easily verified by comparing it with the measured Stokes' parameters. We measure these Stokes' parameters by the following equation:

$$P_1^{meas} = \frac{\int I(\lambda, 0^\circ) d\lambda - \int I(\lambda, 90^\circ) d\lambda}{\int I(\lambda, 0^\circ) d\lambda + \int I(\lambda, 90^\circ) d\lambda}$$

which can be re-written as

$$P_1^{meas} = \frac{\int [I(\lambda, 0^\circ) - I(\lambda, 90^\circ)] d\lambda}{\int [I(\lambda, 0^\circ) + I(\lambda, 90^\circ)] d\lambda}$$

(4-16)

where  $I(\lambda, 0^\circ)d\lambda$  represents the intensity in the wavelength range  $\lambda$  to  $\lambda+d\lambda$ .

Replacing  $i$  by 1 in eq.(4-15) and combining it with eq.(4-16), we get the following result:

$$P_1 = \frac{\int \left[ \frac{I(\lambda, 0^\circ) - I(\lambda, 90^\circ)}{I(\lambda, 0^\circ) + I(\lambda, 90^\circ)} \right] A(\lambda) d\lambda}{\int A(\lambda) d\lambda}$$

(4-17)

where  $A(\lambda)d\lambda$  is the probability of a photon of wavelength  $\lambda$  being emitted in the range  $\lambda$  to  $\lambda+d\lambda$ .

Since  $I(\lambda, 0^\circ) + I(\lambda, 90^\circ) = \eta A(\lambda)$ , where  $\eta$  is some constant, therefore eqs. 4-16 & 4-17 can be written as

$$P_1^{meas} = \frac{\int [I(\lambda, 0^\circ) - I(\lambda, 90^\circ)] d\lambda}{\eta \int A(\lambda) d\lambda} = P_1$$

(4-18)

i.e the measured and calculated Stokes' parameters corresponds to the same quantity. Thus eq.(4-15) is a valid way of calculating average Stokes' parameters.

**Table 4-1: Birefringences ( $n_e - n_o$ ) of quartz vs wavelength  $\lambda$ . [86]**

$\lambda$ nm	$(n_e - n_o)$ $10^{-4}$
150	214
200	130
250	111
300	103
350	98
400	96

**Table 4-2: Thicknesses of retarders at different wavelength ( $\lambda$ ).**

$\lambda$ nm	d $\mu\text{m}$
200	7.69
243	10.84
300	14.56
486	26.27

**Table 4-3: Transmission efficiencies  $\epsilon_M, \epsilon_m$  of polarizers and spectral distribution  $A(\lambda)$  of two photons versus wavelength  $\lambda$  [87,14].**

$\lambda$ nm	$\epsilon_M$ $10^3$	$\epsilon_m$ $10^4$	$A(\lambda)$
182.9	1694	7760	140.8
202.7	2307	8772	117.4
221.1	2722	9149	100.0
243.1	3080	9339	83.03
270.2	3379	9383	66.47
303.9	3640	9406	52.23
347.3	3880	9443	39.06

Table 44. Variations of transmission efficiencies ( $\epsilon_M, \epsilon_m$ ), degree of polarization  $\Pi$  and spectral distribution  $A(\lambda)$  versus wavelength  $\lambda$ .

$\lambda$ , nm	$\frac{\epsilon_M}{10^6}$	$\frac{\epsilon_M}{10^4}$	$\frac{\epsilon_M \epsilon_m}{10^4}$	$\frac{\epsilon_M + \epsilon_m}{10}$	$\Pi = \frac{\epsilon_M \epsilon_m}{\epsilon_M + \epsilon_m}$	$A(\lambda)$
185	1780	78400	76620	80180	9555	132
195	2100	84000	81900	86100	9512	124
200	2200	86600	84400	88800	9504	119.5
205	2360	88800	86440	91160	9482	115
215	2580	90400	87820	92980	9445	105
225	2800	92000	89200	94800	9409	96
235	2980	93200	90220	96180	9380	88
245	3100	93590	90490	96690	9358	81.5
255	3240	93600	90360	96840	9330	75
265	3340	93600	90260	96940	9310	68.5
275	3440	93800	90360	97240	9292	64
285	3520	94000	90480	97520	9278	59
295	3600	94000	90400	97600	9262	55
305	3660	94000	90340	97660	9250	51.5
315	3720	94000	90280	97720	9238	47.5
325	3780	94200	90420	97980	9252	45
335	3840	94200	90360	98040	9216	42
345	3880	94400	90520	98280	9210	40
355	3940	94400	90460	98340	9198	37.5

Table 4-5: Stokes' parameters  $P$ ,  $P_{\text{scat}}$ ,  $A(\lambda)$ , versus wavelength  $\lambda$ , for a HWP at  $t=200$  nm of thickness  $d=7.69\mu\text{m}$ 

$\lambda$ nm	$A(\lambda)$	$\Pi$ $10^4$	$(n_x - n_y)$ $10^{-4}$	$\phi$ rad	$P_{\text{scat}} \cos \phi$ $10^4$	$A(\lambda) \Pi P_{\text{scat}} = P_I$ $10^7$	$P_{\text{scat}} \sin \phi$ $10^4$	$A(\lambda) \Pi P_{\text{scat}} = P_{II}$ $10^7$
185	132	9555	144	3.760	-8142	-10269.17	5805	7321.61
195	124	9512	134	3.320	-9840	-11606.16	1777	2095.95
200	119.5	9504	130	3.140	-9999	-11356.13	-9	-10.21
205	115	9482	127	2.993	-9890	-10784.35	-1477	-1610.56
215	105	9445	122	2.741	-9211	-9134.77	-3892	-3859.79
225	96	9409	118.5	2.544	-8271	-7470.89	-5620	-5076.34
235	88	9380	115	2.364	-7129	-5884.56	-7012	-5787.98
245	81.5	9358	112.5	2.218	-6034	-4601.99	-7973	-6080.81
255	75	9330	110.5	2.093	-4994	-3494.55	-8663	-6061.93
265	68.5	9310	109	1.987	-4046	-2580.27	-9144	-5831.44
275	64	9292	107	1.879	-3042	-1809.04	-9525	-5664.40
285	59	9278	105.5	1.788	-2160	-1182.38	-9763	-5344.28
295	55	9262	104	1.703	-1322	-673.44	-9912	-5049.27
305	51.5	9250	102.5	1.623	-529	-251.99	-9985	-4756.59
315	47.5	9238	101	1.549	215	94.33	-9997	-4386.72
325	45	9252	100	1.486	839	349.30	-9964	-4148.45
335	42	9216	99	1.427	1424	551.19	-9898	-3831.23
345	40	9210	98	1.372	1969	725.37	-9804	-3611.79
355	37.5	9198	97	1.320	2479	855.06	-9687	-3341.28

Table 4-6-Stokes parameters  $P_1, P_2, P_3$ , Birefringences and Spectral distribution  $A(\lambda)$  versus wavelength  $\lambda$  for HWP at  $\lambda=243$  nm of thickness  $d=10.84 \mu\text{m}$ 

$\lambda$ nm	$A(\lambda)$	$\Pi$ $10^4$	$(n_v - n_o)$ $10^4$	$\phi$ rad	$P_1 = \cos\phi$ $10^4$	$A(\lambda)P_1 = P_1$ $10^4$	$P_2 = \sin\phi$ $10^4$	$A(\lambda)P_2 = P_2$ $10^4$
185	132	9555	144	5.30	5543	6991.16	8322	10496.20
195	124	9512	135	4.68	-323	-380.97	9994	11787.80
205	115	9482	127	4.21	-4815	-5250.42	8764	9556.52
215	105	9445	122	3.86	-7528	-7465.70	6581	6526.54
225	96	9409	118.5	3.58	-9054	-8178.15	4244	3633.45
235	88	9380	115	3.33	9823	-8108.29	1872	1383.43
245	81.5	9358	112.5	3.12	-9997	-7624.47	-215	-163.97
255	75	9330	110.5	2.95	-9817	-6869.44	-1904	-1332.32
265	68.5	9310	109	2.80	-9422	-6008.73	-3349	-2135.76
275	64	9292	107	2.65	-8815	-5242.17	-4720	-2806.92
285	59	9278	105.5	2.52	-8129	-4449.83	-5823	-3187.52
295	55	9262	104	2.40	-7373	-3755.87	-6754	-3440.55
305	51.5	9250	102.5	2.28	-6512	-3102.15	-7588	-3614.73
315	47.5	9238	101	2.18	-5722	-2510.84	-8201	-3598.63
325	45	9252	100	2.09	-4961	-2065.46	-8682	-3614.66
330	43.5	9245	99.5	2.05	-4610	-1853.94	-8873	-3568.33
335	42	9216	99	2.01	-4252	-1645.83	-9050	-3503.00
345	40	9210	98	1.93	-3515	-1294.92	-9361	-3448.59
355	37.5	9198	97	1.86	-2851	-983.37	-9584	-3305.76

Table 4-7 Stokes' parameters  $P_1, P_2, P_3$ , Birefringences and Spectral distribution  $A(\lambda)$  versus wavelength  $\lambda$  for a HWP at  $\lambda=300$  nm of thickness  $d=14.56 \mu\text{m}$

$\lambda$ nm	$A(\lambda)$	$\Pi$ $10^4$	$(n_x - n_y)$ $10^4$	$\theta$ rad	$P_1 = \cos\theta$ $10^4$	$A(\lambda)\Pi P_1 = P_1$ $10^4$	$P_2 = \sin\theta$ $10^4$	$A(\lambda)\Pi P_2 = P_2$ $10^4$
185	132	9555	144	8376	6691	8439.09	-7430	-9371.16
195	124	9512	135	0.050	9987	11779.54	-502	-592.10
205	115	9482	127	5.667	8163	8901.18	5775	6297.23
215	105	9445	122	5.191	4606	4567.88	1.8875	8801.55
225	96	9409	118.5	4.818	1055	952.94	9944	8982.05
235	88	9380	115	4.476	-2333	-1925.75	9723	8025.75
245	81.5	9358	112.5	4.200	-4895	-3733.29	8719	6649.77
255	75	9330	110.5	3.964	-6802	-4759.69	7329	5128.46
265	68.5	9310	109	3.762	-8131	-5185.41	5820	3711.61
275	64	9292	107	3.559	-9139	-5434.85	4058	2413.24
285	59	9278	105.5	3.386	-9701	-5310.34	2424	1326.90
295	55	9262	104	3.225	-9965	-5076.27	834	424.84
300	53	9258	103	3.140	-9999	-4906.24	-6	-2.94
305	51.5	9250	102.5	3.074	-9977	-4752.78	-671	-319.64
315	47.5	9238	101	2.933	-9783	-4292.82	-2068	-907.44
325	45	9252	100	2.814	-9470	-3942.73	-3209	-1336.03
335	42	9216	99	2.703	-9055	-3504.93	-4241	-1641.57
345	40	9210	98	2.598	-8561	-3153.87	-5166	-1903.15
355	37.5	9198	97	2.499	-8009	-2762.49	-5987	-2065.06

Table 4-4-Stokes' parameters  $P, Q, R$ , Birefringences and Spectral distribution  $A(\lambda)$  versus wavelength  $\lambda$ , for a HWP at  $\lambda=486$  nm of thickness  $d=26.27 \mu\text{m}$ 

$\lambda$ nm	$A(\lambda)$	$\Pi$ $10^4$	$(n_x - n_y)$ $10^4$	$\phi$ rad	$P = \cos\phi$ $10^4$	$A(\lambda)P_x = P_I$ $10^4$	$P_y = \sin\phi$ $10^4$	$A(\lambda)P_y = P_y$ $10^4$
185	132	9555	144	0.281	9606	12114.78	-2.777	-3502.51
195	124	9512	135	5.143	4183	4933.79	9082	1071.20
205	115	9482	127	3.942	-6960	-7589.39	7179	7828.19
215	105	9445	122	3.082	-9982	-9899.390	-585	-580.15
225	96	9409	118.5	2.409	-7440	-6720.28	-6681	-6034.70
235	88	9380	115	1.794	-2215	-1828.34	-9751	-8048.86
245	81.5	9358	112.5	1.296	2712	2068.38	-9624	-7340.00
255	75	9330	110.5	0.8693	6452	4514.78	-7639	-5345.39
265	68.5	9310	109	0.506	8746	5577.63	-4847	-3091.09
275	64	9292	107	0.139	9903	5889.19	-1386	-824.23
285	59	9278	105.5	6.110	9850	5391.90	1722	942.628
295	55	9265	104	5.819	8942	4556.01	4476	2280.85
305	51.5	9250	102.5	5.547	7410	3529.93	6714	3198.38
315	47.5	9238	101	5.292	5480	2404.65	8364	3670.16
325	45	9252	100	5.078	3582	1491.32	9336	3886.95
335	42	9216	99	4.877	1647	637.50	9863	3817.69
345	40	9210	98	4.688	-237	-87.31	9997	3682.89
355	37.5	9198	97	4.510	-2009	-692.94	9796	3378.88

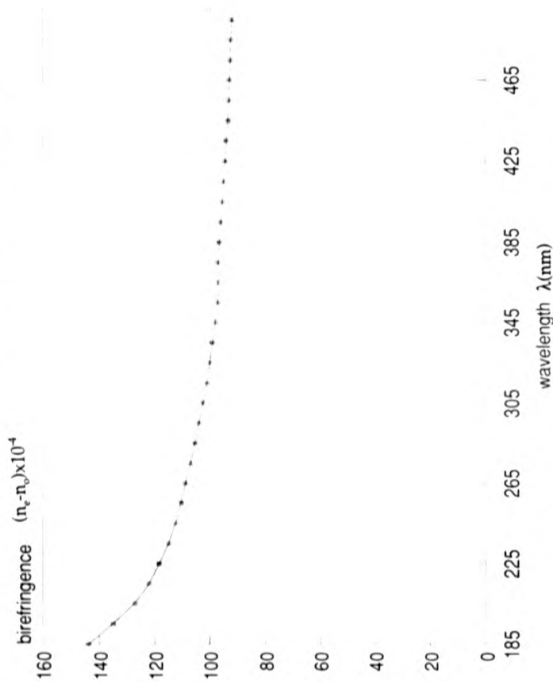
Table 4-9a: Expected and measured Stokes' parameters for different half-wave plates

HWP nm	P <sub>1</sub>			P <sub>2</sub>			P <sub>3</sub>				
	P <sub>1</sub>	P <sub>1</sub> (A)	P <sub>1</sub> (AIT)	P <sub>2</sub> <sup>e</sup>	P <sub>2</sub> (A)	P <sub>2</sub> (AIT)	P <sub>3</sub> <sup>e</sup>	P <sub>3</sub> (A)	P <sub>3</sub> (AIT)	P <sub>3</sub> <sup>m</sup>	
0	0.9362 ±0.0042	.....	.....	0.891 ±0.090	0.00	0.00	-0.032 ±0.085	0.000	.....	.....	-0.006 ±0.085
200	-0.380	-0.529	-0.502	-0.332 ±0.060	0.00	0.00	0.128 ±0.106	-0.721	-0.607	-0.543	-0.640 ±0.104
243	-0.626	-0.611	-0.573	-0.5190 ±0.0789	0.00	0.00	0.186 ±0.138	-0.208	0.044	0.041	-0.1368 ±0.0915
300	-0.427	-0.204	-0.181	-0.0344 ±0.0330	0.00	0.00	0.010 ±0.040	0.302	0.334	0.317	0.2251 ±0.0844
486	0.268	0.163	0.155	0.1150 ±0.061	0.00	0.00	0.006 ±0.086	0.158	0.002	0.0149	-0.033 ±0.087

Table 4-9b: Expected and measured total polarization for different half-wave plates.

HWP nm	P <sub>tot</sub>			P <sub>tot</sub> <sup>m</sup>			
	P <sub>tot</sub>	P <sub>tot</sub> (A)	P <sub>tot</sub> (AIT)	P <sub>tot</sub> <sup>e</sup>	P <sub>tot</sub> <sup>m</sup> (A)	P <sub>tot</sub> <sup>m</sup> (AIT)	P <sub>tot</sub> <sup>m</sup>
0	0.9362±0.0042	.....	.....	.....	.....	.....	0.9520±0.1040
200	0.8150	0.8063	0.7398	0.7398	0.7398	0.7398	0.7819±0.1036
243	0.6601	0.6129	0.5747	0.5747	0.5747	0.5747	0.6006±0.0862
300	0.5234	0.3920	0.3657	0.3657	0.3657	0.3657	0.2704±0.0845
486	0.3113	0.1639	0.1560	0.1560	0.1560	0.1560	0.1200±0.0635

## Birefringence analysis of quartz crystal



Fig(4.3). Variation of bi-refrignence  $(n_e - n_o)$  of quartz versus wavelength  $\lambda$ .

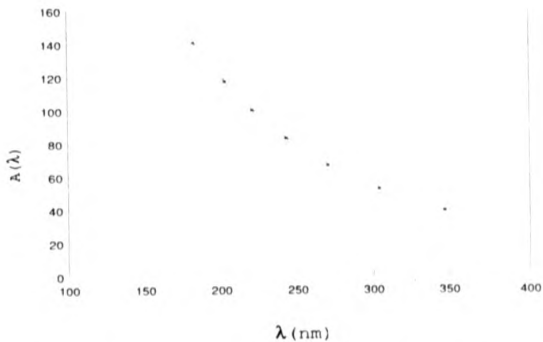


Fig 4.4. Spectral distribution function  $A(\lambda)$  of two photons versus wavelength  $\lambda$ .

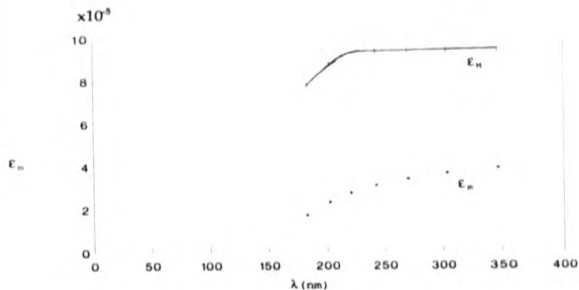
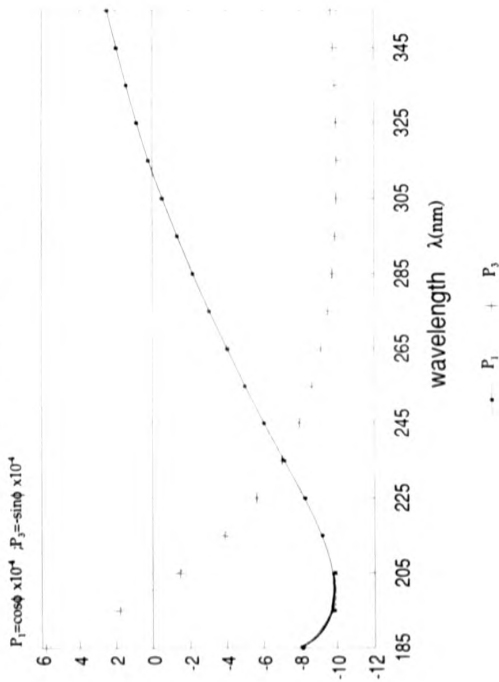


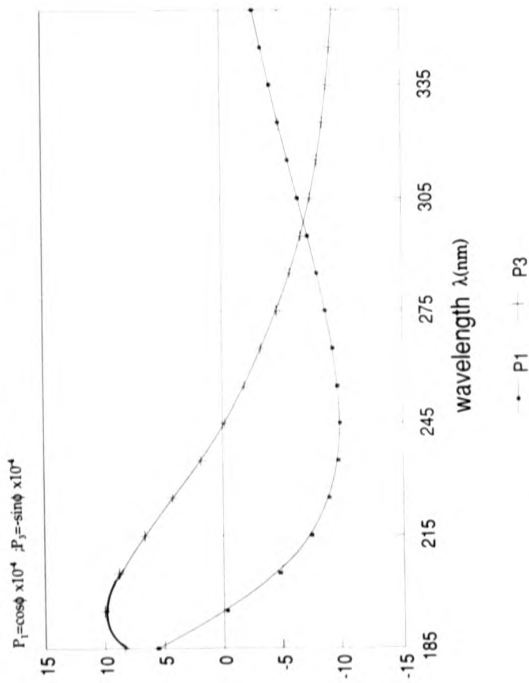
Fig 4.5. The wavelength dependence of the transmission efficiencies  $\epsilon_M$  and  $\epsilon_m$  for light polarized, respectively, parallel to and perpendicular to the transmission axes of the linear polarizers.

## Retardation analysis HWP at wavelength 200nm



Fig(4.6).Retardation analysis of HWP at  $\lambda=200\text{nm}$ .

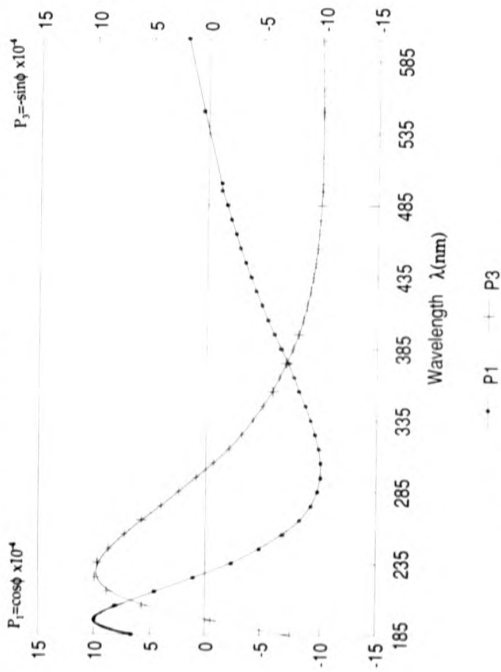
## Retardation analysis



Fig(4.7).Retardation analysis of HWP at  $\lambda=243\text{nm}$

## Retardation analysis

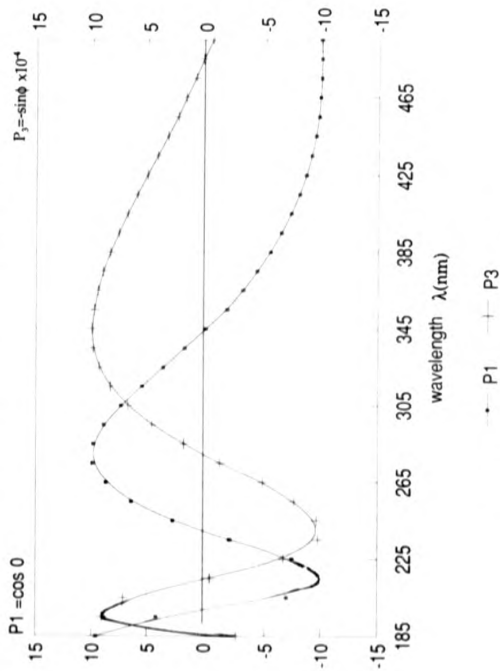
Stokes parameters vs wavelength



Fig(4.8) Retardation analysis of HWP at  $\lambda = 300$  nm.

## RETARDATION ANALYSIS

### Stokes parameters vs wavelength



Fig(4.9) Retardation analysis of HWP at  $\lambda = 486$  nm.

#### §4.11:PROCEDURE FOR CHECKING THE OPTIC AXIS AND RETARDATION OF A GIVEN RETARDER

The following steps were carried out to check the optic axis, retardation values and the transmission percentage of the retarders before using them in the detection part of the main apparatus.

(b).Find out the wavelength  $\lambda$  for which the given half-wave plate at wavelength  $\lambda$  will act as a quarter waveplate. This can be easily achieved using the eq.(2-75) of section §2.9 and is given by

$$\lambda / 4d = (n_e - n_o) \quad (4-19)$$

Both sides of eq.(4-19) are wavelength dependent, and hence one can draw a graph of each side versus wavelength. The point of intersection of these two graphs will determine the wavelength  $\lambda$  at which a given half-wave plate at wavelength  $\lambda$  will act as quarter-wave plate. These graphs are shown in Fig.4.10. Table 4-10 shows the results of the above mentioned procedure for the retarders chosen for the experiment.

It can be seen from Table 4-10 that we can only check the half-wave plates at  $\lambda = 243 \text{ nm}$ ,  $300 \text{ nm}$  with the help of a naked eye because of the fact that  $\lambda$  falls within the visible range from  $400 \text{ nm}$  to  $700 \text{ nm}$ .

##### (ii) Checking the optic axis

To check the marked axis(optic axis as reported by the manufacturer, Gooch & Housego Ltd.) on the retarder, we insert it between the two crossed polarizers and rotate it until the field is as dark as without it. This position could be determined within the limits of  $\pm 2^\circ$ . The schematic diagram of the

experimental arrangement is shown in Fig.4.11. The experiment can be performed either by using white light or monochromatic light produced by passing the light through filter F.

(iii) Checking of the retardation:

We calculated the retardation value of the given retarder, whose thickness is known, at different wavelengths by using eq.(2-75) of section §2.9. These retardation values were calculated for wavelength 500 nm in the green part of the spectrum and are tabulated in Table 4-11 under the heading  $\delta_r(G)$ . Fig.4.12 shows the schematic diagram of the experimental arrangement for measuring the retardation values of the given retarder for a particular wavelength in this case at 500 nm. Ordinary light from the source S is passed through the green filter F to obtain monochromatic green light. With the axis of the two polarizers A & B crossed, we inserted the Soleil-Babinet compensator (SBC) with its axis oriented at  $45^\circ$  to that of polarizer A. We set the zero-retardation band (dark band) in the centre of the field by turning the micrometer screw of the SBC to obtain a reference point. We then obtained the dark band (nearest to the reference point) on either side of the reference point and recorded the readings. The separation of any two of the above mentioned consecutive dark bands gives the calibration of the SBC i.e. how much linear motion of SBC corresponds to a full wave retardation at  $\lambda$  (green). These calibrations for the green line are given in Table 4-11 under the heading  $\lambda(G)$ . The construction and working of the SBC can be found in reference [86]. We then inserted the given retarder R with its optic axis oriented parallel to that

of SBC, as shown in Fig.4.12 and repeated the experimental procedure as described for the calibration and watched the direction of rotation of the micrometer screw of the SBC while obtaining the reference dark band. If it was clockwise (i.e moving towards increasing negative values on the SBC linear scale) then, as reported by the manufacturer of SBC (BHalle Nachf Berlin-Steglitz), the optic axis of the compensator is the slow axis and hence the marked axis of the retarder R shall be the fast axis to account for the compensation for zero retardation. We recorded the position of the dark band immediately next to the reference one. The difference of this reading from that of the reference one determines the retardation of the given retarder at the given wavelength  $\lambda$ . These values are tabulated in Table 4-11 under the heading  $\delta_m(G)$ . These values were found to be nearly the same as expected, thereby, confirming that the given retarder is a zero-order half-wave plate at  $\lambda$  acting as quarter-wave plate at  $\lambda$ .

Similar procedures were adopted for the other plates for checking their retardation values. The measured retardation values for each of these plates is shown in Table 4-11 and they were quite in agreement with the expected ones. Hence it was concluded that the retarders supplied by the manufacturer were zero-order half-wave plates as specified.

(iv) Wavelength dependence of the transmission was measured using ultra-violet spectrophotometer KONTRON UVIKON 860 and the results of the "lambda-scan" are shown in Table 4-12.

**Table 4-10: Conversion of HWP of given  $\lambda$  into QWP at  $\lambda$** 

HWP $\lambda(\text{nm})$	$(n_e-n_o)$ $10^{-5}$	$d_{\text{HWP}}$ $\mu\text{m}$	$\lambda$ $\text{nm}$
200	1020	7.69	315
243	113	10.75	485
300	920	14.56	540
486	870	26.27	870

**Table 4-11: Retardation values of the HWP plates for green line.**

HWP(nm)	$d_{\text{HWP}}(\mu\text{m})$	X(G)	$\delta(\text{G})$	$\delta_o(\text{G})$
200	7.69	12.90	.142 $\lambda$	.140 $\lambda$
243	10.84	12.90	.20 $\lambda$	.193 $\lambda$
300	14.56	12.90	.27 $\lambda$	.27 $\lambda$
486	26.27	12.90	.485 $\lambda$	.475 $\lambda$

**Table 4-12: Wavelength dependence of the transmission for the chosen retarders.**

Retarders at $\lambda$ nm	Transmission percentage
200	82.5
243	81.7
300	81.3
486	89.9

Graphical determination of wavelength  
at which HWP will act as QWP.

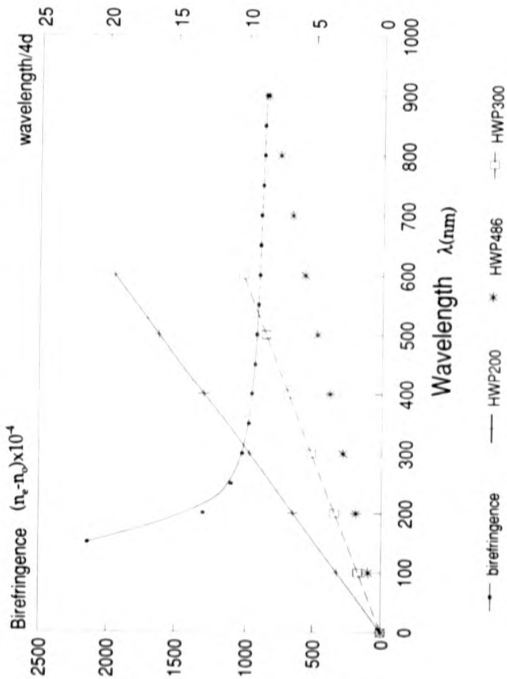


Fig.(4.10). Graphical determination of wavelength at which half-wave plate will act as quarter-wave plate.

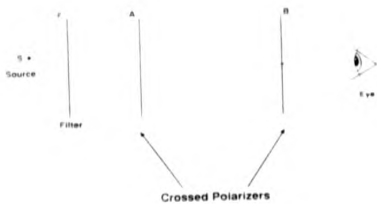


Fig 4.11. Experimental set up for checking the optic axis of a given retarder.

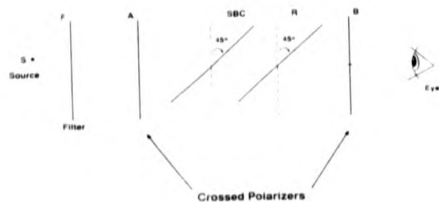


Fig 4.12). Experimental set up for measuring the retardation of a given retarder.

## CHAPTER V

### MEASUREMENTS AND RESULTS

#### §5:INTRODUCTION

During the course of study,different experiments(described in the coming sections §5.1,§5.2,§5.3,§5.4) were performed using achromatic and non-achromatic retarders(quarter-wave plates and half-wave plates) in conjunction with the detection system described in section §3.10 of chapter III. **The main aim of these experiments was to measure the coherence length and bandwidth of single photons of atomic two-photon radiation and hence to obtain for the first time a measurement of the spectral distribution by depolarization of a prepared two-photon polarized source** and to confirm experimentally the following properties of the "entangled" state of the two-photon pair:

- (i) The result of the polarization measurement of the photon by a detector on one side can be considered to determine instantaneously the result for the polarization state of the other photon of the pair,despite the fact that the detection events are space-like separated in the relativistic sense.
- (ii) The plane of polarization of one of the two photons of a two-photon pair can be considered to be rotated through  $90^\circ$  when passed through an achromatic half-wave plate.
- (iii) The fine and hyperfine interaction, resulting from the electron and nuclear spin respectively does not affect the two-photon emission and consequently its polarization state - the Breit and Teller [59] hypothesis.

## EXPERIMENT I

## §5.1: TWO LINEAR POLARIZERS AND A TWO-PHOTON PAIR

Fig 5.1 shows the schematic experimental arrangement of the apparatus. The transmission axis of the polarizer A is aligned vertical parallel to the x-axis, while that of the linear polarizer B is rotatable in the range  $0 \leq \theta \leq 90^\circ$ . All the rotations were measured with respect to the x-axis.

The present work employed the photon-photon polarization coincidence technique (described in section §4.5 of chapter IV) which involves the determination of three Stokes' parameters  $P_1, P_2, P_3$  (discussed in Appendix §F) characterizing the vector polarization of the emitted pair of two-photons.

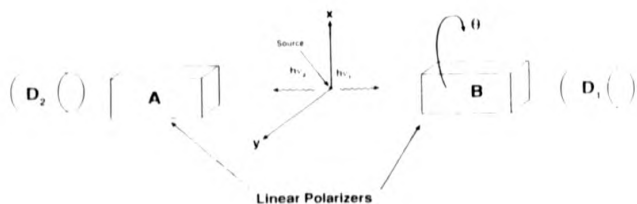
Coincidence rates  $N_c(\theta)$  were measured for angles  $\theta = 0^\circ, 90^\circ, \pm 45^\circ$  and they were further normalized according to the procedure described in section §4.9 of chapter IV.

## 5.1.1: Linear polarization correlation measurements

The linear polarization correlation measurements were carried out without the quarter-wave plate or the half-wave plate in the detection system. Stokes' parameters  $P_1$  and  $P_2$  for the linear polarization correlation (shown in Table 5-1) were derived directly from the normalized coincidence rates  $I(0), I(90), I(\pm 45)$  using the following equations

$$P_1 = \frac{I(0) - I(90)}{I(0) + I(90)}, \quad P_2 = \frac{I(45) - I(-45)}{I(45) + I(-45)}$$

(5-1)



Fig(5.1) A typical experimental arrangement used for two-photon polarization correlation measurements.  $D_1$  and  $D_2$  are photomultipliers.

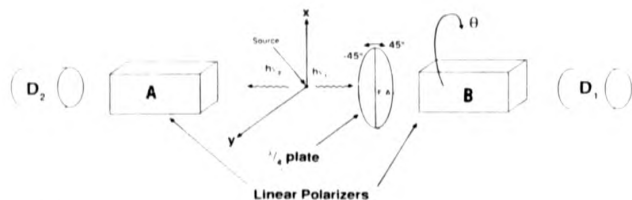


Fig (5.2) Schematic diagram of the typical ideal experimental arrangement using two linear polarizers A & B ,two detectors  $D_1$  and  $D_2$ .The transmission axis of the polarizer B is rotated through angles  $\theta$  while that of A is oriented vertical parallel to the x-axis.The fast axis of the  $\lambda/4$  plate is set at  $\pm 45^\circ$  relative to the x-axis to obtain left-hand and right-hand circular polarization.

True Stokes' parameters  $P_1, P_2$  (shown in Table 5-1) were obtained by dividing the measured ones by the degree of polarization  $\Pi$  (defined in section §2.6 of chapter II; eq 2-55) given by

$$\Pi = \frac{\epsilon_A - \epsilon_B}{\epsilon_A + \epsilon_B} = 0.9362 \pm 0.0042 \quad (5-2)$$

where the transmission efficiencies  $\epsilon_A, \epsilon_B$  of the polarizers A and B have been actually measured [24] and are given by

$$\epsilon_A = 0.908 \pm 0.013, \quad \epsilon_B = 0.0299 \pm 0.002 \quad (5-3)$$

### 5.1.2: Circular polarization correlation measurements

The circular polarization correlation measurements were carried out by inserting a quarter-wave plate (aperture  $\phi = 19.5$  mm) nominally achromatic over the wavelength range 180 nm to 300 nm in front of the linear polarizer B with its fast axis set at angles  $\pm 45^\circ$  with the x-axis while keeping the transmission axes of both the polarizers A and B vertical and parallel to the x-axis as shown in Fig.5.2. The optic axis of the quarter-wave plate is set at  $45^\circ$  with respect to the x-axis for right circular polarized light and for the left circular polarized light it is set at  $-45^\circ$  with respect to the x-axis. The corresponding Stokes' parameter  $P_3$  is determined by the relation

$$\beta_3 = \frac{I(RHC) - I(LHC)}{I(RHC) + I(LHC)} \quad (5-4)$$

where I(RHC) and I(LHC) denote the normalized coincidence rates for right hand and left hand circular polarized light respectively. Table 5-1 also shows the measured and true Stokes' parameters  $P_1$  and  $P_2$ .

Total polarization  $P_{tot}$  (also shown in Table 5-1) is calculated by the following relation:

$$|P_{tot}| = \sqrt{P_1^2 + P_2^2 + P_3^2}$$

(5-5)

**Table 5-1: Measured and True Stokes' parameters without any retarder:**

Measured Stokes' parameters			True Stokes' parameters			T.Pol(True)
$P_1$	$P_2$	$P_3$	$P_1$	$P_2$	$P_3$	$P_{tot}$
0.891	-0.030	-0.006	0.951	-0.032	-0.006	0.952
$\pm 0.090$	$\pm 0.080$	$\pm 0.098$	$\pm 0.098$	$\pm 0.085$	$\pm 0.085$	$\pm 0.104$
Expected Stokes' parameters						
0.8765	0.000	0.000	.9362	0.000	0.000	0.9362
$\pm 0.0079$			$\pm 0.0042$			$\pm 0.0042$

**5.1.3: Quantum mechanical prediction for the photon "2" seen by the polarizer A.**

The action of the polarizer A, on the left side of the source in Fig.5.1, represented by the matrix A, on a beam described by a 4x4 density matrix  $\rho$  (cf. Eq.2-25; chap. II) is to transform the polarization state of the beam to a new state whose density matrix is  $\rho'$  [14], where

$$\rho' = A\rho A^\dagger \quad (5-6)$$

With the help of eq.2-44; § 2.5 of chapter II, we can write the matrix for the polarizer A as

$$A = \begin{pmatrix} I_1 & 0 \\ 0 & I_2 \end{pmatrix} \quad (5-7)$$

where  $I_1$  and  $I_2$  are the complex amplitudes for the transmission of light parallel and perpendicular to the transmission axes of the polarizers.

Substituting eq.5-7 into eq.5-6 and doing further simplification, we have the following relation

$$\rho' = \frac{1}{2} \left[ \begin{pmatrix} 1 & 0 \\ 0 & 1 \end{pmatrix}_1 \otimes \begin{pmatrix} I_1^2 & 0 \\ 0 & 0 \end{pmatrix}_2 + \begin{pmatrix} 0 & 1 \\ 0 & 0 \end{pmatrix}_1 \otimes \begin{pmatrix} 0 & I_1 I_2^* \\ 0 & 0 \end{pmatrix}_2 + \begin{pmatrix} 0 & 0 \\ 1 & 0 \end{pmatrix}_1 \otimes \begin{pmatrix} 0 & I_2 I_1^* \\ 0 & 0 \end{pmatrix}_2 + \begin{pmatrix} 0 & 0 \\ 0 & I_2^2 \end{pmatrix}_1 \right] \quad (5-8)$$

Eq.5-8 has been obtained by taking care of the fact that the matrix operator A acts only on the matrices labelled "2" representing the Photon "2" seen by the

polarizer A. These matrices are lying on the right side of the product symbol  $\otimes$  in the above equation.

The effective density matrix for the photon "2" is then given by

$$\rho_{\text{eff}} = \text{Tr}_2 \hat{\rho} \quad (5-9)$$

where the trace operation  $\text{Tr}_2$  acts only on the photon "2" i.e on the matrices lying on the right side of the symbol  $\otimes$  in eq 5-8. On simplification, eq.5-9 becomes as

$$\rho_{\text{eff}} = \frac{1}{2} \begin{pmatrix} I_1^2 & 0 \\ 0 & I_2^2 \end{pmatrix} = \frac{1}{2} \begin{pmatrix} \epsilon_M & 0 \\ 0 & \epsilon_m \end{pmatrix} \quad (5-10)$$

where  $\epsilon_M$  and  $\epsilon_m$  represents the transmission efficiencies of the polarizers.

The normalized density matrix for the photon "2" is obtained by dividing eq.5-10 by  $(\frac{1}{2})(\epsilon_M + \epsilon_m)$  i.e

$$\rho_{\text{nor}} = \begin{pmatrix} \frac{\epsilon_M}{\epsilon_M + \epsilon_m} & 0 \\ 0 & \frac{\epsilon_m}{\epsilon_M + \epsilon_m} \end{pmatrix} \quad (5-11)$$

The relationship between the density matrix and the Stokes' parameters  $P_1, P_2, P_3$  has already been established through eq.2-48; §2.6 of chapter II and is given by

$$\rho = \frac{1}{2} \begin{pmatrix} 1+P_1 & P_2-iP_3 \\ P_2+iP_3 & 1-P_1 \end{pmatrix} \quad (5-12)$$

Comparing eq.5-11 with eq.5-12, and substituting the values of the transmission efficiencies of the polarizers, we have the following values for the Stokes' parameters  $P_1, P_2, P_3$

$$P_1 = \frac{E_H^* E_H + E_V^* E_V}{E_H^* E_H - E_V^* E_V} = 0.9362 \pm 0.0042, P_2 = 0, P_3 = 0 \quad (5-13)$$

and hence the expected total polarization will be

$$P_{tot}^* = 0.9362 \pm 0.0042 \quad (5-13a)$$

#### 5.1.4:Result

The experimental measurements of the Stokes' parameters for photon "1" shown in Table 5-1 are, within the limits of experimental error, in good agreement with the quantum mechanically predicted Stokes' parameters for the photon "2" seen by the polarizer A (given by eq.5-13) neglecting the fine and hyperfine interaction. In other words, the Breit and Teller hypothesis is confirmed. The measurements are also consistent with the idea that the polarization measurement of photon by a detector on one side, can be considered to determine instantaneously the result for the polarization state of the other of the pair emitted by second-order decay process, despite the fact that the detection events are space-like separated in the relativistic sense.

## EXPERIMENT 2

**§5.2:TWO LINEAR POLARIZERS, AN ACHROMATIC HALF-WAVE PLATE  
AND A TWO-PHOTON PAIR**

In this experiment, we studied the effect on the polarization properties of the two-photons emitted simultaneously from the metastable atomic deuterium of an achromatic half-wave. The plate was inserted in between the collimating lens and the front of the polarizer B. The optic axis was oriented at  $45^\circ$  with respect to the x-axis. Fig 5.3 shows the schematic experimental arrangement of the apparatus for measuring the linear polarization correlation measurement.

An achromatic quarter-wave plate was inserted in between the half-wave plate and the front of the polarizer B, as shown in Fig 5.4, with its optic axis set at  $\pm 45^\circ$  to the x-axis for measuring the circular polarization correlation measurement.

Exactly the same procedure was adopted for measuring the Stokes' parameters  $P_0, P_1, P_2$  as described in experiment 1, section §5.1.

**5.2.1:MEASUREMENTS**

Table 5-2a shows the measured Stokes' parameters with and without the achromatic half-wave plate and Table 5-2b shows the true Stokes' parameters which were obtained by dividing the measured Stokes' parameters by the degree of polarization  $\Pi$  of the linear polarizers A and B, defined by eq.(5-2)

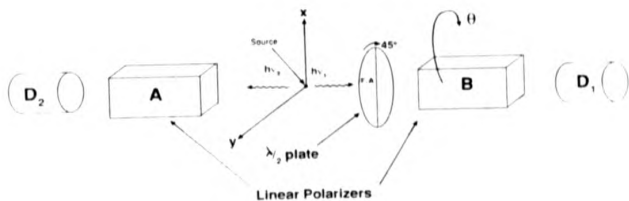


Fig.(5.3).Schematic diagram of the typical ideal experimental arrangement using two linear polarizers A & B ,two detectors  $D_1$  and  $D_2$ .The transmission axis of the polarizer B is rotated through angles  $\theta$  while that of A is oriented vertical parallel to the x-axis,the fast axis of the  $\lambda/2$  plate is set at  $45^\circ$  relative to the x- axis. polarization.

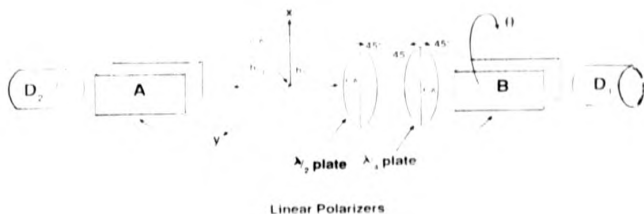


Fig.(5.4).Schematic diagram of the typical ideal experimental arrangement using two linear polarizers A & B,two detectors  $D_1$  and  $D_2$ .The transmission axis of the polarizer B is rotated through angles  $\theta$  while that of A is oriented vertical parallel to the x-axis,the fast axis of the  $\lambda/2$  plate is set at  $45^\circ$  relative to the x-axis,the fast axis of the  $\lambda/4$  plate is set at  $\pm 45^\circ$  relative to the x-axis to obtain left-hand and right-hand circular polarization.

Table 5-2a: Measured Stokes' parameters with and without achromatic half-wave plate.

Stokes' parameters without HWP					Stokes' parameters with HWP				
$P_1$	$P_2$	$P_3$	$P_{tot}$	$P_4$	$P_1$	$P_2$	$P_3$	$P_{tot}$	$P_4$
0.891	-0.030	-0.006	0.891	-0.938	-0.450	-0.490	1.140		
$\pm 0.090$	$\pm 0.080$	$\pm 0.080$	$\pm 0.09$	$\pm 0.300$	$\pm 0.280$	$\pm 0.400$	$\pm 0.320$		
Predicted Stokes' parameters									
0.8765	0.0000	0.0000	0.8765	-0.8765	0.0000	0.0000	-0.8765		
$\pm 0.0079$				$\pm 0.0079$			$\pm 0.0079$		

Table 5-2b: True Stokes' parameters with and without achromatic half-wave plate.

Stokes' parameters without HWP					Stokes' parameters with HWP				
$P_1$	$P_2$	$P_3$	$P_{tot}$	$P_4$	$P_1$	$P_2$	$P_3$	$P_{tot}$	$P_4$
0.951	-0.032	-0.006	0.952	-1.030	-0.495	-0.530	1.262		
$\pm 0.098$	$\pm 0.085$	$\pm 0.085$	$\pm 0.104$	$\pm 0.300$	$\pm 0.280$	$\pm 0.400$	$\pm 0.320$		
Predicted Stokes' parameters									
0.9362	0.0000	0.0000	0.9362	-0.9362	0.0000	0.0000	0.9362		
$\pm 0.0042$				$\pm 0.0042$			$\pm 0.0042$		

From Table 5-2b we see that, with the half-wave plate

$$|P_{103}| = \sqrt{P_1^2 + P_2^2 + P_3^2} = 1.262 \pm 0.320$$

### 5.2.2: Quantum mechanical prediction for the modified two-photon polarization state produced by insertion of an achromatic half-wave plate

Stokes' parameters  $P_1, P_2, P_3$  for the above mentioned situation have already been derived quantum mechanically in chapter II, section §2.8 eq (2-71) and they are as follows

$$P_1 = -\left| \frac{\epsilon_{\alpha} - \epsilon_{\beta}}{\epsilon_{\alpha} + \epsilon_{\beta}} \right|^2 = -0.8765 \pm 0.0079; P_2 = 0; P_3 = 0$$

(5-14)

since here  $\epsilon_{\alpha}, \epsilon_{\beta}$  are given by Eq 5-3. The true Stokes' parameters of the single photon on the right can then be obtained by dividing the measured ones by the degree of polarization  $|P_1|$ . These are shown in table 5-2b

### 5.2.3: Result

The experimental measurements, given in Table 2b are, within the limits of error, in good agreement with the quantum mechanical predictions also shown in table 5-2b, neglecting fine and hyperfine interaction and thus again confirm indirectly, the Breit and Teller hypothesis i.e. the electron spin and nuclear spin do not play any role in the two-photon decay process. The statistical errors in this case are considerably larger due partly to the reduction in signal strength resulting from the insertion of half-wave plate and partly in

the reduced time spent on taking these measurements. The results, however, are consistent with the idea that the insertion of the half-wave plate on the right rotates the plane of polarization of the photon on the right through  $90^\circ$  resulting in the new entangled state vector

$$|\Psi\rangle = \frac{1}{\sqrt{2}} (|x\rangle_1 \otimes |y\rangle_2 + |y\rangle_1 \otimes |x\rangle_2)$$

(5-15)

Thus detection of an x-polarized photon on the left is now associated with detection of a y-polarized photon on the right, reflected in the fact that the first Stokes' parameter  $P_1$  is negative and close to unity rather than positive as before.

## EXPERIMENT 3

## §5.3:TWO LINEAR POLARIZERS, A MULTI-ORDER PLATE AND A TWO-PHOTON PAIR

The experimental arrangement is exactly the same as shown in Figures 5.3 and 5.4 except that the achromatic half-wave plate is replaced by a non-achromatic multiple order half-wave plate at wavelength 694 nm consisting of a quartz plate of actual thickness 1.3 mm. With the same procedure as described for experiments 1 and 2, we measured the Stokes' parameters  $P_1, P_2, P_3$  and calculated the total polarization using eq.5-5. These measurements are shown in Table 5-3.

**Table 5-3:Measured and True Stokes' Parameters with non-achromatic half-wave plate at wavelength  $\lambda=694$  nm of thickness 1.3 mm.**

Measured Stokes' parameters				True Stokes' parameters			
$P_1$	$P_2$	$P_3$	$P_{tot}$	$P_1$	$P_2$	$P_3$	$P_{tot}$
0.070	-0.021	-0.095	0.112	0.074	-0.022	-0.101	0.119
$\pm 0.012$	$\pm 0.106$	$\pm 0.149$	$\pm 0.133$	$\pm 0.012$	$\pm 0.113$	$\pm 0.159$	$\pm 0.142$
Predicted Stokes' parameters							
0.000	0.000	0.000	0.000	0.000	0.000	0.000	0.000

## 5.3.1:Result

As we know that the first surface of the plate can be considered to act as a polarizing beam splitter, the two resulting orthogonally polarized wavepackets travel at different group velocities through the plate introducing a relative displacement between them. The emerging radiation will be completely depolarized because of the very large thickness of the plate and hence a very large optical path difference  $\delta = 21801 \text{ nm}$ , 32 wavelengths at 694 nm. The wavepackets will not overlap and the total polarization will be zero. This fact is established, within the limits of experimental error, from the results shown in table 5-3.

## EXPERIMENT 4

**§5.4:TWO LINEAR POLARIZERS, A (ZERO-ORDER) MULTIWAVE PLATE  
AND A TWO-PHOTON PAIR**

The experimental arrangement is exactly the same as shown in Figures 5.3 & 5.4 except that the achromatic half-wave plate is replaced one at a time by zero-order half-wave plates at wavelengths 200 nm, 243 nm, 300 nm and 486 nm. These half-wave plates, made of uniaxial quartz crystal, were chosen according to the procedure described in detail in section §4.10 under the heading "choice of retarders" in chapter IV. The actual experimental arrangement is shown in Figures 5.5 & 5.6.

The half-wave plate is placed on the right side of the source with its optic axis set at  $45^\circ$  with respect to the  $x$ -axis. The first surface of this plate acts as a polarizing beam splitter. The two resulting orthogonally polarized components travel at different speeds through the plate introducing a phase shift between them (cf. see section §4.10 of chapter IV) and, finally, the two components recombine on emerging from the second surface. Normally the emerging radiation will, in general, be in a state of pure elliptical polarization. However if the coherence length is very short, the recombination may not be complete and the emerging radiation will then appear to be partially polarized or even completely unpolarized [46].

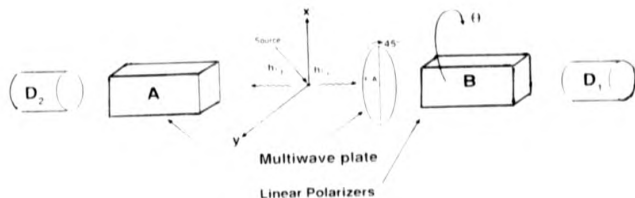


Fig.(5.5).Schematic diagram of the typical ideal experimental arrangement using two linear polarizers A & B,two detectors  $D_1$  and  $D_2$ .The transmission axis of the polarizer B is rotated through angles  $\theta$  while that of A is oriented vertical parallel to the x-axis,the fast axis of the  $\lambda/2$  plate (multi-wave) is set at  $45^\circ$  relative to the x-axis.

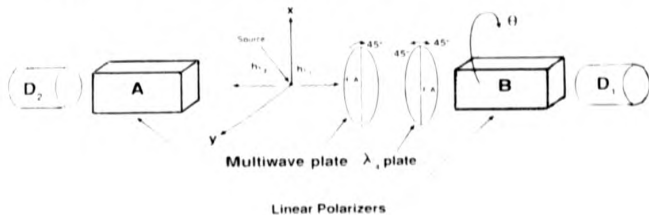


Fig.(5.6).Schematic diagram of the typical ideal experimental arrangement using two linear polarizers A & B,two detectors  $D_1$  and  $D_2$ .The transmission axis of the polarizer B is rotated through angles  $\theta$  while that of A is oriented vertical parallel to the x-axis,the fast axis of the  $\lambda/2$  plate (multi-wave) is set at  $45^\circ$  relative to the x-axis,the fast axis of the  $\lambda/4$  plate is set at  $\pm 45^\circ$  relative to the x-axis to obtain left-hand and right-hand circular polarization.

### 5.4.1: Measurements

In order to measure the total polarization, we inserted the zero-order half-wave plates at wavelengths 200 nm, 243 nm, 300 nm and 486 nm in turn and measured the Stokes' parameters  $P_1, P_2, P_3$  for each of these plates according to the procedure described in section §5.1. In addition, we also inserted two of the half-wave plates at wavelengths 200 nm and 243 nm together in series with their optic axes oriented parallel and perpendicular to each other to obtain effectively two more zero-order half-wave plates of thickness  $d=18.53 \mu\text{m}$ , corresponding to half-wave plate at 354 nm, and  $d=3.15 \mu\text{m}$  corresponding approximately to a half-wave plate at 150 nm. The Stokes' parameters  $P_i$  ( $i=1,2,3$ ) were also measured for these plates according to the procedure as stated above. Exactly, as described above, the HWP at wavelength 486 nm was placed in series with the HWP at 200 nm with its optic axis parallel to each other to obtain effectively another HWP of thickness  $34.96 \mu\text{m}$  at wavelength 640 nm. The Stokes' parameters for this plate was also measured with the same procedure as for the others described above. The results are shown in Table 5-4a along with the true values obtained by dividing the measured values by the degree of polarization  $\Pi$  given by eq.5-2 in §5.2. The expected Stokes' parameters ( $P_i^e, i=1,2,3$ ) for a series of plate thicknesses  $d$  corresponding to zero-order half-wave plates in the range from 0 to 700 nm have been calculated according to the procedure described in section §4.10 and are shown in the Table 5-4a along with the relative displacement of the wavepacket  $\delta$  introduced by each of them. Figures 5-7 and 5-8 show the variations of the expected (shown by curves) and measured Stokes' parameters  $P_1, P_3$  with respect to the relative displacement of wavepacket  $\delta$  introduced by each plate.

Table 5-4b shows the total measured polarization  $P_{tot}^m$  for each of the above mentioned half-wave plates along with their corresponding expected total polarization  $P_{tot}^e$ .

Figures 5.7, 5.8, and 5.9 show the measured values of respectively, the Stokes' parameters  $P_1$ ,  $P_3$  and the total polarization  $P_{tot}^m$  as a function of the relative displacement  $\delta$  of the orthogonally polarized wavepackets. The solid lines show the theoretically expected values of these quantities obtained by graphical integration as previously described. It is clear that within the limits of error there is good agreement between the measured and expected values of the Stokes' parameters  $P_1$ ,  $P_3$  and the total polarization  $P_{tot}^m$ . It is interesting to note the approximate damped oscillatory nature of the behaviour of  $P_1$  and  $P_3$  with  $\delta$  with a period of 180 nm for the first "oscillation" increasing in length for subsequent "oscillations". The total polarization  $P_{tot}^m$  is seen to fall rapidly from approximately "1" at  $\delta=0$  to a low value at  $\delta=400$  nm. Theoretically if the bandwidth to be associated with a single photon is indeed in the range from 185 nm to 355 nm as previously discussed, a coherence length  $l_c = \lambda^2/\Delta\lambda = 386$  nm would be expected (see section 5.4.2).

The results are therefore consistent with the idea of the single photon of a two-photon pair being represented by a wavepacket of coherence length about 400 nm and the very short coherence time  $\tau_c$  of  $400 \text{ nm}/c = 1.33 \times 10^{-15}$  s rather than the long coherence length and long coherence time that would be expected if the properties of the single photon were determined by the  $\frac{1}{2}$  a lifetime of the metastable state.

From the coherence time  $\tau_c = 1.33 \times 10^{-15}$  s, one can easily calculate, using the relation  $\Delta\nu = 1/\tau_c$ , the bandwidth  $\Delta\nu$  of single photons of atomic two-

**photon radiation.** It was found to be  $0.75 \times 10^{15} \text{ Hz} = 10^{15} \text{ Hz}$  which is almost equal to the **bandwidth** ( $= 0.77 \times 10^{15} \text{ Hz}$ ) of the uv range (185 nm to 355 nm) obtained by using the relation  $\nu = c/\lambda$ .

Furthermore, the measured value of the relative displacement of wavepacket  $\delta = 88.888 \text{ nm}$  at  $P_1 = 0$ , from the Fig. 5.7, confirms our assumption that the photon can be represented by a wavepacket having central wavelength 243 nm. This was checked by us in the following way.

The wavelength  $\lambda_0$ , corresponding to the carrier frequency  $\omega_0$ , was calculated by a graphical method using the formula [85], given below, for the values of  $\delta$  at which  $P_1 = 0$

$$\delta = \left[ 1 + \frac{\alpha_0 - \alpha_1}{n_0 - n_1} \right] \left[ \frac{\lambda_0}{4}, \frac{3\lambda_0}{4}, \dots, \dots \right] \quad (5-15a)$$

where  $(\alpha_0 - \alpha_1)/(n_0 - n_1)$  is a wavelength dependent correction term.

The graphical method, mentioned above, requires the computation of the slopes  $\partial(n_0 - n_1)/\partial\lambda$  for different wavelengths from the graph shown in Fig. 4.3 and the determination of the corresponding birefringence  $(n_0 - n_1)$  values. Multiplying the slopes by their corresponding values of wavelength and then dividing them by the respective values of birefringence  $(n_0 - n_1)$ , yields the correction term in eq.(5-15a).

In the method a graph of the right hand side of eq.(5-15a) was drawn as a function of wavelength. The wavelength at which the right hand side was equal to the value of  $\delta$  corresponding to  $P_1 = 0$  was then determined as shown in Fig.5.10. It can be seen that the centre wavelength is given by this method as  $\lambda_0 = 236 \pm 10 \text{ nm}$ . While a similar analysis using the results for  $P_1$ , gave  $\lambda_0 = 233 \pm 10 \text{ nm}$ . Both results are in agreement with the theoretical value of 243 nm.

Table 5-4a: Measured, True and Expected Stokes' parameters for the half-wave plates used in the experiment.

HWP $\lambda$ , nm	d $\mu$ m	$\delta$ nm	Measured			True <sup>1</sup>			Expected		
			$P_1$	$P_2$	$P_3$	$P_1$	$P_2$	$P_3$	$P_1^*$	$P_2^*$	$P_3^*$
0	0	0	0.891 $\pm 0.090$	-0.030 $\pm 0.080$	-0.006 $\pm 0.080$	0.951 $\pm 0.098$	-0.032 $\pm 0.085$	-0.006 $\pm 0.085$	0.9362 $\pm 0.0042$	0.00	0.00
150	3.15	52.8	0.399 $\pm 0.088$	0.00	-0.567 $\pm 0.108$	0.4267 $\pm 0.094$	0.00	-0.6064 $\pm 0.116$	0.5175	0.00	-0.7257
200	7.69	129	-0.332 $\pm 0.060$	0.120 $\pm 0.100$	-0.640 $\pm 0.104$	-0.3547 $\pm 0.064$	0.128 $\pm 0.106$	-0.684 $\pm 0.111$	-0.502	0.00	-0.543
243	10.84	181.8	-0.519 $\pm 0.078$	0.186 $\pm 0.138$	-0.137 $\pm 0.091$	-0.554 $\pm 0.084$	-0.198 $\pm 0.147$	-0.145 $\pm 0.097$	-0.573	0.00	0.041
300	14.56	244.2	-0.034 $\pm 0.033$	0.010 $\pm 0.040$	0.2251 $\pm 0.0844$	-0.066 $\pm 0.057$	0.106 $\pm 0.064$	0.2398 $\pm 0.0896$	-0.181	0.00	0.317
354	18.53	310.7	-0.052 $\pm 0.0985$	0.00	0.2319 $\pm 0.084$	-0.0055 $\pm 0.105$	0.00	0.2477 $\pm 0.089$	0.0524	0.00	0.1714
425	22.48	376.98	...	...	...	...	...	...	0.077	0.00	0.123
486	26.27	440.5	0.115 $\pm 0.061$	0.006 $\pm 0.081$	-0.033 $\pm 0.087$	0.122 $\pm 0.064$	0.006 $\pm 0.086$	-0.036 $\pm 0.092$	0.155	0.00	0.0149
550	29.98	502.76	...	...	...	...	...	...	0.151	0.00	-0.068
600	33.00	553.46	...	...	...	...	...	...	0.060	0.00	-0.089
640	34.96	586.27	0.044 $\pm 0.103$	0.00	0.033 $\pm 0.259$	0.046 $\pm 0.110$	0.00	0.035 $\pm 0.270$	0.007	0.00	-0.120
700	38.97	653.60	...	...	...	...	...	...	-0.027	0.00	-0.075

<sup>1</sup> Stokes' parameters obtained by dividing the measured ones by the degree of polarization  
 $\Pi = 0.9362 \pm 0.0042$

Table 5-4b: Measured and expected total polarization for the half-wave plates used in the experiment.

HWP $\lambda_{nm}$	d $\mu m$	$\delta$ nm	$P_{tot}^m$	$P_{tot}^e$
0	0	0	$0.9520 \pm 0.1040$	$0.9362 \pm 0.0042$
150	3.15	52.8	$0.7414 \pm 0.109$	0.8913
200	7.69	129	$0.7819 \pm 0.1036$	0.7398
243	10.84	181.8	$0.6006 \pm 0.0862$	0.5747
300	14.56	244.2	$0.2704 \pm 0.0845$	0.3657
354	18.53	310.7	$0.2477 \pm 0.089$	0.1792
425	22.48	376.98	.....	0.1451
486	26.27	440.5	$0.1200 \pm 0.0635$	0.1560
550	29.98	502.76	.....	0.1650
600	33.00	553.46	.....	0.107
640	34.96	586.27	$0.058 \pm 0.195$	0.127
700	38.97	653.6	.....	0.079

#### 5.4.2: Quantum mechanical prediction of the coherence length of the two-photon radiation

In the situation where the two-photons are emitted simultaneously in opposite directions with frequencies  $\nu_1$  and  $\nu_2$  as shown in Fig.2.1 in section §2.2 of chap II, the coherence length  $l_c$  can be written as

$$l_c = c \Delta t \quad (5-16)$$

where  $\Delta t$  is the coherence time interval of these simultaneously emitted two-photons and "c" denotes the speed of light.

In eq.5-16, the only unknown is the time interval  $\Delta t$  which can be calculated using the Heisenberg uncertainty principle stating that the product of the uncertainties in energy  $\Delta E$  and time  $\Delta t$  is equal to the Plank's constant  $\hbar$  i.e

$$\Delta E \Delta t = \hbar \quad (5-17)$$

where  $\Delta E = h(\nu_1 - \nu_2) = \hbar \Delta \nu$ .

Making use of the relation  $c = \lambda \nu$  in eq.(5-17) and combining it with eq.(5-16), we get the following expression for the coherence length  $l_c$

$$|l_c| = c \Delta t = \left| \frac{\lambda_1 \lambda_2}{\lambda_1 - \lambda_2} \right| = \frac{\lambda^2}{\Delta \lambda} \quad (5-18)$$

where  $\lambda_1$  and  $\lambda_2$  are the extreme limits of the ultra-violet region i.e  $\lambda_1 = 185$  nm and  $\lambda_2 = 355$  nm. Substituting the numerical values of  $\lambda_1$  and  $\lambda_2$  in eq.(5-18) and simplifying, we get the coherence length  $l_c$  as given below

$$l_c = 386.32 \text{ nm} \quad (5-19)$$

### Analysis of Stokes' Parameter P1

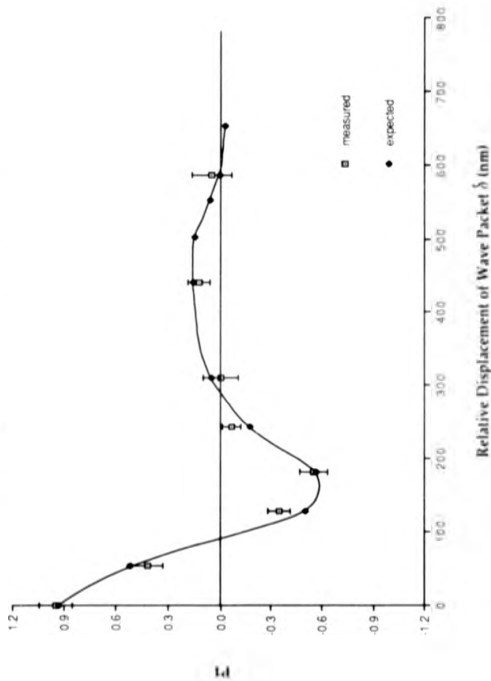
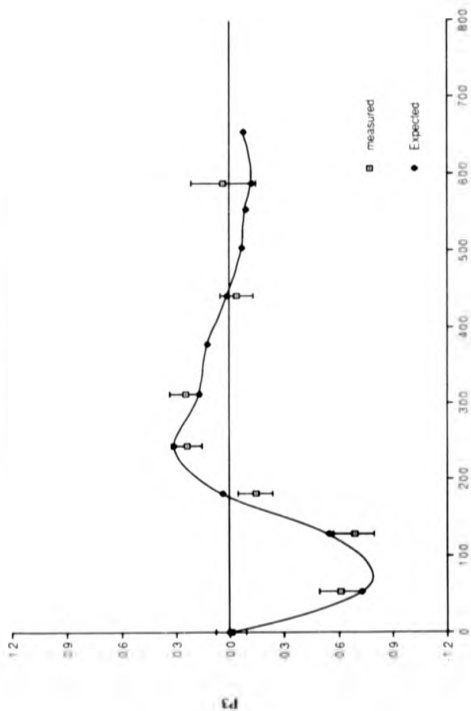


Fig.5.7  
Relative Displacement of Wave Packet  $\delta$  (nm)

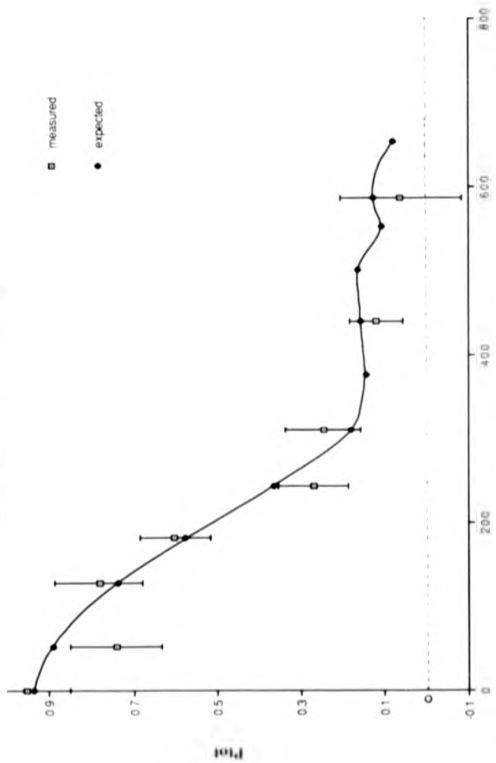
### Analysis of Stokes' Parameter P3



Relative Displacement of Wave Packet  $\Delta$  (nm)

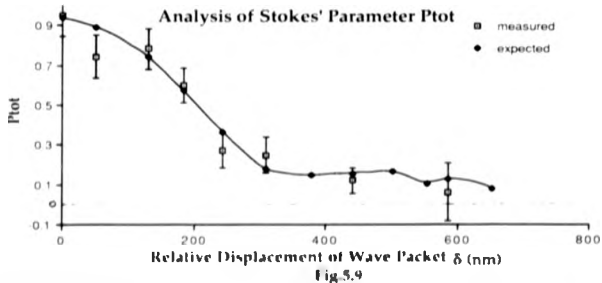
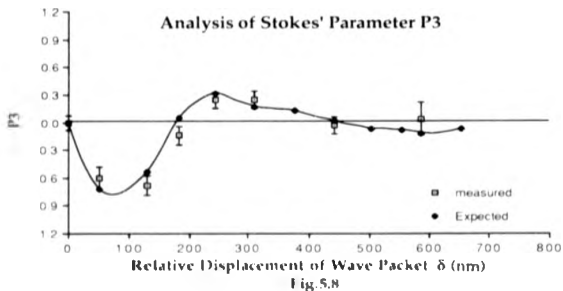
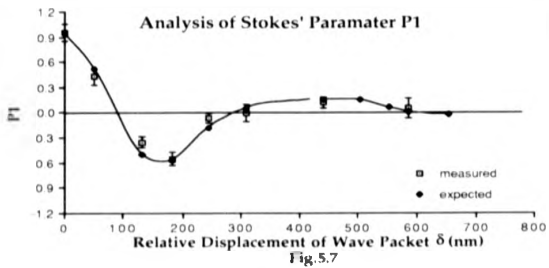
Fig.5.8

### Analysis of Stokes' Parameter Plot



Relative Displacement of Wave Packet  $\delta$  (nm)

Fig.5.9



## Wavepacket analysis

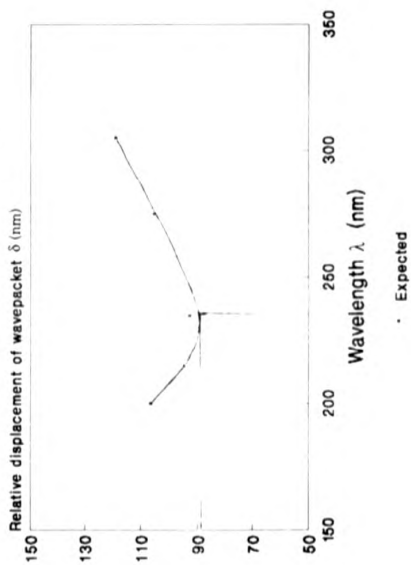


Fig.5.10

## CHAPTER VI

### DISCUSSION

On examining table 5-2a and table 5-2b, first of all we note that the results for the Stokes' parameters without the half-wave plate in place agree, within the limits of experimental error, with the quantum mechanical predictions calculated in § 5.1.3. Previous measurements [24] of the polarization correlation with only two linear polarizers were also found to agree well with the quantum mechanical predictions and were used successfully to test Bell's inequality [24]. Since the quantum mechanical prediction involves the hypothesis, made originally by Breit and Teller [59], that the fine and hyperfine interaction plays no part in the two-photon decay process, the good agreement between theory and experiment can be considered indirectly to provide confirmation of the Breit and Teller hypothesis.

In addition the results are consistent with the idea, implicit in the form of the state vector given by Eq.2-22, that, in the case of ideal polarizers, the single photon on the right detected in coincidence with a photon on the left which has passed through a polarizer with its transmission axis in the  $x$ -direction, may itself, to all intents and purposes, be regarded as polarized in the  $x$ -direction. Of course, since the polarizer on the left is not ideal, the single photon on the right is not completely polarized in this sense, but the experimental accuracy is not sufficient to detect this deviation from the ideal. The results with the half-wave plate in place are also in broad general

agreement with the quantum mechanical predictions although the statistical errors in this case are considerably larger due partly to the reduction in signal strength resulting from the insertion of the half-wave plate and partly to the reduced time spent on taking these measurements. The results, however, are consistent with the idea that the insertion of the half-wave plate on the right rotates the plane of polarization of the photon on the right through  $90^\circ$  resulting in the new entangled state vector given by Eq.5-15. Thus detection of an x polarized photon on the left is now associated with the detection of a y polarized photon on the right, reflected in the fact that the first Stokes'parameter  $P_1$  is negative and close to unity rather than positive as before.

It has also been shown that the total polarization is zero when the beam is passed through a birefringent plate of very large thickness. This result can be explained easily by the fact,that, assuming the single photon can be represented by a wavepacket, the optical path difference  $\delta$  between the two orthogonally polarized wavepackets is very large resulting in a completely depolarized emergent beam. An interesting situation arises when we allow the beam to pass through the various non-achromatic half-wave plates at different wavelengths of correspondingly different thicknesses. It has been shown that the total polarization gradually falls in the range between 0 nm and 300 nm followed by a sharp fall of total polarization in the range between 300 nm and 400 nm. Beyond this range the polarization continues to fall but at a slower rate. Therefore, one is in a position to say that the coherence length of a single

photon of the two-photon pair falls within the range between 300 nm and 400 nm. This enables us to claim that for the first time, in a novel way, we have been successful in measuring the coherence length of a single photon of a two-photon pair produced in the decay of metastable atomic deuterium by observing the polarization of the photons in what is essentially a single-photon interference experiment. We have also resolved the controversy over whether the coherence length is very long corresponding to the long life of  $\frac{1}{2}$  sec of the metastable state or very short by measuring a very short coherence length.

We have seen above that the experimental results are in agreement with the theoretical predictions based on the assumption of a particular spectral distribution  $A(\lambda)$  for the two-photon emission process as might be expected. However, viewed from another aspect, the experimental method and result described in this work can be regarded as a method of determining the spectral distribution function  $A(\lambda)$  regarded as unknown. For example, by a method of trial and error the form of  $A(\lambda)$  which best agrees with the results could be found. However, such an approach is likely to be laborious and imprecise with no guarantee that the result obtained is a unique form for  $A(\lambda)$ . A better method would need to be found to measure  $A(\lambda)$  satisfactorily. We have, in fact, been able to go some way towards the determination of  $A(\lambda)$  on the basis of a theory proposed by A.J.Duncan [85]. This theory allows us to deduce that the centre wavelength and bandwidth of the single-photon, and hence also of the two-photon spectral distribution,  $236 \pm 10$  nm and  $0.75 \times 10^{13}$  Hz respectively, in agreement with the theoretically predicted values of 243 nm

and  $0.77 \times 10^{15}$  Hz.

In conclusion, experimentally we have demonstrated successfully the effect of optically active materials on short wavepackets, theoretically examined for short laser-pulses by A.J.Duncan et al [46], using multi-wave birefringent plates.

Finally, it is interesting to note how the simplest atom, atomic hydrogen, continues to prove such a versatile testing ground for fundamental ideas in atomic physics and quantum mechanics.

## APPENDIX

### §A:PHOTON POLARIZATION

#### INTRODUCTION

A classical light wave propagating in the Z-direction is described by the electric field vector E given by

$$E(x, t) = \begin{pmatrix} E_x(x, t) \\ E_y(x, t) \\ 0 \end{pmatrix} \quad (\text{A-1})$$

where

$$E_x(x, t) = E_x e^{i(kx - \omega t)} \quad (\text{A-2})$$

$$E_y(x, t) = E_y e^{i(kx - \omega t)} \quad (\text{A-3})$$

and k is the wavenumber of the light ( $k = 2\pi/\lambda$ ),  $\omega$  is the angular frequency.

In addition

$$E_x = E_{0x} e^{i\alpha_x}; E_y = E_{0y} e^{i\alpha_y} \quad (\text{A-4})$$

where  $\alpha_x, \alpha_y$  are the phases and  $E_{0x}$  and  $E_{0y}$  are the real amplitudes of the

electric field. The polarization state of the light is directly related to the E-vector. For example:

- (i) if  $E_y = 0$ , the wave is plane polarized in the x-direction
- (ii) if  $E_x = 0$ , the wave is plane polarized in the y-direction
- (iii) if  $E_x = E_y$ , the wave is polarized with its plane of polarization at  $45^\circ$  to the x-axis as shown in Fig.(A.1)
- (iv) If

$$E_y = e^{i\pi/2} = iE_x$$

then the y-component lags the x-component by  $90^\circ$  and the wave is right circular polarized (RCP)

- (v) similarly, if

$$E_y = -iE_x$$

then the wave is left circular polarized (LCP)

The average energy per unit volume of the wave, in S.I. units, is given by

$$= \epsilon E^2$$

The total energy of the wave in the volume  $V$  is then given by

$$\epsilon E^2 V$$

(A-5)

Now if we pass a wave polarized at an angle of  $45^\circ$  to the x-axis through a polaroid filter that transmits x-polarized light, but not y-polarized light, then before the light passes through the polaroid

$$E_x = E_y = E \quad (\text{A-6})$$

After it passes through the polarizer,

$$E_x = E, E_y = 0 \quad (\text{A-7})$$

and the beam emerges polarized in the x-direction and its total energy is halved. The emerging electric field is along x-axis.

Now let us consider the effect of the polarizer from a quantum mechanical point of view. The total energy of a wave of frequency  $\omega$  cannot be arbitrary but must be an integral multiple of  $\hbar\omega$ :

$$E_{\text{tot}} = N\hbar\omega \quad (\text{A-8})$$

where  $N$  is the number of photons in the wave.

The probability of the photon passing through the polaroid along the x-direction is given by

$$\frac{|E_x|^2}{|E_x|^2 + |E_y|^2} = \frac{|E_x|^2}{|E|^2} \quad (\text{A-9})$$

Similarly, if we had a device that passed only right circular polarized light, then the probability that one photon would pass through the device, and emerge with RCP is given by

$$\frac{|E_{RCP}|^2}{|E_{RCP}|^2 + |E_{LCP}|^2} \quad (\text{A-10})$$

since all beams of light can be considered to be superpositions of many beams consisting of one photon each, let us discuss the polarization properties of a single photon. The general laws of quantum mechanics are just the generalization of the classical mechanics, so that for one photon, one can write from eqs.(A-5) & (A-8) that

$$|E|^2 V = 8\pi\hbar\omega \quad (\text{A-11})$$

#### A.1: STATE VECTOR OF THE PHOTON POLARIZATION

The state vector of the photon polarization is defined as

$$|\Psi\rangle = \begin{pmatrix} \Psi_x \\ \Psi_y \end{pmatrix} \quad (\text{A-12})$$

by writing

$$\Psi_x = \sqrt{\frac{V}{8\pi\hbar\omega}} E_x, \quad \Psi_y = \sqrt{\frac{V}{8\pi\hbar\omega}} E_y \quad (\text{A-13})$$

The  $|\Psi\rangle$  vectors are vectors in a complex two-dimensional space, since their components are complex numbers. From (A-11) it follows at once that  $|\Psi\rangle$  unit length:

$$|\Psi_x|^2 + |\Psi_y|^2 = 1$$

(A-13a)

In fact, the state vectors are independent of the volume  $V$  and depend only on the state of polarization of the photon. For example, if

$$|\Psi\rangle = \frac{1}{\sqrt{2}} \begin{pmatrix} e^{i\alpha} \\ e^{-i\alpha} \end{pmatrix}$$

then the photon is polarized at  $45^\circ$  to  $x$ -axis. A knowledge of the  $|\Psi\rangle$  vector gives us all the information we can have about the state of polarization of the photon.

Some special examples of these vectors are:

$$|x\rangle = \begin{pmatrix} 1 \\ 0 \end{pmatrix}; \text{ } x\text{-polarization}$$

$$|y\rangle = \begin{pmatrix} 0 \\ 1 \end{pmatrix}; \text{ } y\text{-polarization}$$

$$|R\rangle = \frac{1}{\sqrt{2}} \begin{pmatrix} 1 \\ i \end{pmatrix}, \dots \dots \dots (RCP)$$

$$|L\rangle = \frac{1}{\sqrt{2}} \begin{pmatrix} 1 \\ -i \end{pmatrix}, \dots \dots \dots (LCP)$$

(A-14)

Each column vector  $|\psi\rangle$  has an associated row vector  $\langle\psi|$  defined by

$$\langle\psi| = (\psi_x^*, \psi_y^*) \quad (\text{A-15})$$

where \* stands for complex conjugate.

The scalar product of a row vector  $\langle\phi|$  and a column vector  $|\psi\rangle$  is given by

$$\langle\phi|\psi\rangle = \phi_x^* \psi_x + \phi_y^* \psi_y = (\psi|\phi)^*$$

The normalization condition (A-13) on the  $|\psi\rangle$  vectors can then be written as

$$\langle\psi|\psi\rangle = 1 \quad (\text{A-16})$$

clearly,

$$\langle x|x\rangle = 1 = \langle y|y\rangle, \quad \langle R|R\rangle = 1 = \langle L|L\rangle \quad (\text{A-17})$$

The vectors  $|x\rangle$  and  $|y\rangle$  are orthogonal in the sense that

$$\langle x|y\rangle = 0 \quad (\text{A-18})$$

They are said to form a basis, since any  $|\psi\rangle$  vector can be written as a linear superposition of them:

$$|\Psi\rangle = \begin{pmatrix} \Psi_x \\ \Psi_y \end{pmatrix} = \Psi_x |x\rangle + \Psi_y |y\rangle$$

(A-19)

because they are orthogonal and satisfy the normalization condition (A-16). The basis they form is called orthonormal. Similarly, the set  $|R\rangle$  and  $|L\rangle$  form an orthonormal basis, since we can always write

$$|\Psi\rangle = \begin{pmatrix} \Psi_x \\ \Psi_y \end{pmatrix} = \frac{\Psi_x - i\Psi_y}{\sqrt{2}} |R\rangle + \frac{\Psi_x + i\Psi_y}{\sqrt{2}} |L\rangle$$

(A-20)

Taking the scalar product of both sides of eq.(A-19) with  $\langle x|$ , we see that

$$\langle x|\Psi\rangle = \Psi_x \langle x|x\rangle + \Psi_y \langle x|y\rangle = \Psi_x$$

(A-21)

Thus we can write eq.(A-19) as

$$|\Psi\rangle = |x\rangle\langle x|\Psi\rangle + |y\rangle\langle y|\Psi\rangle$$

(A-22)

and eq.(A-20), as

$$|\Psi\rangle = |R\rangle\langle R|\Psi\rangle + |L\rangle\langle L|\Psi\rangle$$

(A-23)

Thus any polarization can be regarded as a coherent superposition of, e.g;  $x$  and  $y$  polarization states, or equivalently as a coherent superposition of right and left circular polarization states (superposition principle).

If we have a device that passes only light in the state  $|\eta\rangle$ , rejecting states orthogonal to  $|\eta\rangle$ , then the probability amplitude that a photon in the state  $|\psi\rangle$  will pass through the device is

$$\langle \eta | \psi \rangle$$

(A-24)

and the probability that the photon passes through is

$$|\langle \eta | \psi \rangle|^2$$

(A-25)

It would be interesting to note that this probability is independent of the phase of  $|\eta\rangle$  or  $|\psi\rangle$ , though the probability amplitude depends on this phase.

### §B: DENSITY OPERATOR

#### OUTLINE OF THE PROBLEM

For systems whose state is perfectly well known, it is sufficient to perform on the system a set of measurements corresponding to a complete set of commuting observables. For example, in our experiment, the polarization state of the photons is perfectly well known when the light beam has traversed the polarizer.

However, in practice, the state of the system is often not perfectly determined. This is true, for example, of the polarization state of photons coming from a source of natural (unpolarized) light, and also for the atoms of a beam emitted by a furnace at temperature  $T$ , where the atom's kinetic energy is known statistically. The problem posed by the quantum description of such systems

is the following:

How can we incorporate into the formalism the incomplete information we possess about the state of the system, so that our predictions make maximum use of this partial information. To do this, we shall introduce here a very useful mathematical tool, the density operator, which facilitates the simultaneous application of the postulates of quantum mechanics and the results of probability calculations:

### B.1: THE CONCEPT OF A STATISTICAL MIXTURE

When one has an incomplete information about a system, one typically appeals to the concept of probability. For example, we know that a photon emitted by a source of natural light can have any polarization state with equal probability. Such an incomplete information about the system is represented in quantum mechanics in the following way, the state of this system can be either the state  $|\psi_1\rangle$  with a probability  $p_1$  or the state  $|\psi_2\rangle$  with a probability  $p_2$ , etc. Obviously

$$p_1 + p_2 + \dots = \sum_k p_k = 1 \quad (\text{B-1})$$

we then say that we are dealing with a statistical mixture of states  $|\psi_1\rangle, |\psi_2\rangle, \dots$  with probabilities  $p_1, p_2, \dots$

A system described by a statistical mixture of states (with probability  $p_k$  of the state vector being  $|\psi_k\rangle$ ) must not be confused with a system whose state is a linear superposition of states.

$$|\psi\rangle = \sum_i c_i |\psi_i\rangle$$

(B-2)

It is a well known fact in quantum mechanics, when the state vector is the ket  $|\psi\rangle$ , as given by eq.(B-2), then the "system has a probability  $|c_i|^2$  of being in the state  $|\psi_i\rangle$  when a measurement is made. But a system in the state  $|\psi\rangle$  given by eq.(B-2) is not simply equivalent to a system having the probability  $|c_1|^2$  of being in the state  $|\psi_1\rangle$ ,  $|c_2|^2$  of being in the state  $|\psi_2\rangle$ , etc----- In fact for a linear combination of  $|\psi_i\rangle$ , there exist, in general, interference effects between the states (due to cross terms of the type  $c_1 c_2^*$ , when the modulus of the probability amplitude is squared) which are very important in quantum mechanics we therefore see that it is impossible in general, to describe a statistical mixture of states by an "average state vector" which would be a superposition of the states  $|\psi_i\rangle$ . Even, when we take a weighted sum of probabilities, we can never obtain interference terms between the states  $|\psi_i\rangle$  of a statistical mixture.

**B.2:THE DENSITY OPERATOR(PURE CASE)**

Actually, it is an "average operator" and not an "average vector" which permits a simple description of the statistical mixture of states:the density operator.

Before studying this general case, let us examine the simple case where the state of the system is perfectly known (all the probabilities  $p_k$  are zero, except one). The system is then said to be in a pure state.

We shall show that characterizing the system by its state vector is completely equivalent to characterizing it by a certain operator acting in the state space,the density operator.

**B.3:Description by a state vector**

Consider a system whose state vector at the instant  $t$  is:

$$|\Psi(t)\rangle = \sum_n C_n(t) |U_n\rangle \quad (\text{B-3})$$

where the  $\{|U_n\rangle\}$  form an orthonormal basis of the state space. The coefficients  $C_n(t)$  satisfy the relation:

$$\sum_n |C_n(t)|^2 = 1 \quad (\text{B-4})$$

which expresses the fact that  $|\Psi(t)\rangle$  is normalized.

If  $A$  is an observable, with matrix elements:

$$\langle U_n | A | U_p \rangle = A_{np}$$

(B-5)

then the mean value of  $A$  at the instant  $t$  is:

$$\langle A \rangle (t) = \langle \Psi (t) | A | \Psi (t) \rangle = \sum_{n,p} C_n^* (t) C_p (t) \langle U_n | A | U_p \rangle = \sum_{n,p} C_n^* (t) C_p (t) A_{np}$$

(B-6)

The above equation shows that the coefficients  $C_n(t)$  enter into the mean values through quadratic expressions of the type  $C_n^* (t)C_p(t)$

Finally, the evolution of  $|\Psi(t)\rangle$  is described by the Schrödinger equation:

$$i\hbar \frac{d}{dt} |\Psi (t)\rangle = H(t) |\Psi (t)\rangle$$

(B-7)

where  $H(t)$  is the Hamiltonian of the system.

#### B.4: DESCRIPTION BY A DENSITY OPERATOR

The Projector  $P_\Psi$  onto a ket  $|\Psi\rangle$  is given by

$$P_\Psi = |\Psi\rangle\langle\Psi|$$

The matrix elements of the projector  $P_\Psi$  in the orthonormal basis  $\{|U_n\rangle\}$  are :

$$\langle U_p | P_\Psi | U_n \rangle = \langle U_p | \Psi \rangle \langle \Psi | U_n \rangle$$

$$\begin{aligned}
 &= \langle U_p | \sum_p C_p | U_p \rangle \sum_n C_n^* \langle U_n | U_n \rangle \\
 &= \sum_{n,p} C_p C_n^* \langle U_p | U_p \rangle \langle U_n | U_n \rangle = C_p(t) C_n^*(t)
 \end{aligned}
 \tag{B-8}$$

Thus we see that  $C_p(t)C_n^*(t)$  are the matrix elements of the operator  $|\psi\rangle\langle\psi|$ . It is therefore natural to introduce the density operator

$$\rho(t) = |\psi(t)\rangle\langle\psi(t)|
 \tag{B-9}$$

The density operator is represented in the  $\{|U_n\rangle\}$  basis by a matrix called the **density matrix** whose elements are:

$$\rho_{p,n} = \langle U_p | \rho(t) | U_n \rangle = C_n^*(t) C_p(t)
 \tag{B-10}$$

Now we shall show that this specification of  $\rho(t)$  is sufficient to characterize the quantum state of the system; it enables us to obtain all the physical predictions that can be calculated from  $|\psi(t)\rangle$ .

To do this, let us write formulae given by eqs.(B-4),(B-6),(B-7) in terms of the operator  $\rho(t)$ .

According to eq.(B-10), eq.(B-4) can be rewritten as

$$\sum_n |C_n(t)|^2 = \sum_n \rho_{nn} = \text{Tr} \rho = 1
 \tag{B-10a}$$

i.e. the sum of the diagonal elements of the density matrix is equal to 1. The left hand side of the eq.(B-10a) expresses the total probability of obtaining the eigen value  $a_n$  of some observable  $A$ . Thus the conservation of the probability is expressed in terms of the density matrix as

$$\text{Tr } \rho = 1$$

The eq.(B-6) is then given by [using eq.(B-10)]

$$\langle A \rangle (t) = \langle \psi(t) | A | \psi(t) \rangle = \sum_{n,p} C_n^* C_p \langle U_n | A | U_p \rangle$$

$$= \sum_{n,p} C_n^* C_p A_{np}$$

$$= \sum_{n,p} \langle U_p | \rho | U_n \rangle \langle U_n | A | U_p \rangle$$

$$= \sum_p \langle U_p | \rho A | U_p \rangle$$

Hence,

$$\langle A \rangle (t) = \text{Tr } \rho(t) A$$

(B-11)

Finally, the time evolution of the operator  $\rho(t)$  can be deduced from the Schrödinger eq.(B-7)

$$\begin{aligned}
\frac{d}{dt} \rho(t) &= \frac{d}{dt} |\Psi(t)\rangle\langle\Psi(t)| \\
&= \left( \frac{d}{dt} |\Psi(t)\rangle \right) \langle\Psi(t)| + |\Psi(t)\rangle \left( \frac{d}{dt} \langle\Psi(t)| \right) \\
&= \frac{1}{i\hbar} [H|\Psi\rangle\langle\Psi| - |\Psi\rangle\langle\Psi|H] \\
&= \frac{1}{i\hbar} [H, \rho]
\end{aligned}$$

Thus we have

$$\frac{d}{dt} \rho(t) = \frac{1}{i\hbar} [H, \rho] \tag{B-12}$$

Therefore in terms of the density operator,

- conservation of probability is expressed by

$$\text{Tr} \rho(t) = 1 \tag{B-13}$$

- the mean value of the observable  $A$  is calculated using the formula

$$\langle A \rangle(t) = \text{Tr}[A\rho(t)] = \text{Tr}[\rho(t)A] \tag{B-14}$$

- and the time evolution obeys the equation:

$$i\hbar \frac{d}{dt} \rho(t) = [H(t), \rho(t)] \quad (\text{B-15})$$

- the probability  $P(a_n)$  of the various results  $a_n$  which can be obtained in the measurement of an observable  $A$  at time  $t$  can also be expressed as

$$P(a_n) = \langle \Psi(t) | P_n | \Psi(t) \rangle \quad (\text{B-16})$$

where,

$$P_n = \sum_{i=1}^{g_n} |U_n^i\rangle \langle U_n^i|$$

is the projection operator and  $\{|u_n^i\rangle\}(i=1, 2, 3, \dots, g_n)$  is an orthonormal set of vectors which forms a basis in the eigen space  $E_n$  associated with eigen value  $a_n$ .

The use of density operator eliminates the drawbacks related to the existence of an arbitrary global phase factor for the state vector.

It can be easily verified from eq.(B-9), that the density operator  $\rho$  is an hermitian operator satisfying  $\rho^\dagger = \rho$  and for the pure case

$$\rho^2 = \rho; \text{Tr}\rho^2 = 1 = \text{Tr}\rho \quad (\text{B-17})$$

In summary,

- The density operator  $\rho$  is a positive definite, hermitian operator of trace equal to unity.

- It is always possible to represent the dynamical state of a system by its density operator, whether that state be completely or incompletely known.
- The density operator representing the state of the system is defined in a unique manner, while the vector representing a pure state is at best defined only to within a phase factor.

### §C: A STATISTICAL MIXTURE OF STATES (NON-PURE CASE)

#### C.1: Definition of the density operator

Consider a system for which (at a given instant) the various probabilities  $(p_1, p_2, p_3, \dots, p_k, \dots)$  are arbitrary, on the condition that they satisfy the relations:

$$0 \leq p_1, p_2, p_3, \dots, p_k, \dots \leq 1$$

$$\sum_k p_k = 1$$

(C-1)

under these conditions, how does one calculate the probability  $P(a_n)$  that a measurement of the observable  $A$  will yield the result  $a_n$ ?

Let:

$$P_k(a_n) = \langle \psi_k | P_n | \psi_k \rangle \quad (C-2)$$

be the probability of finding  $a_n$  if the state vector were  $|\psi_k\rangle$ . To obtain the desired probability  $P(a_n)$  one must weight  $P_k(a_n)$  by  $p_k$  and then sum over  $k$ :

$$P(a_n) = \sum_k p_k P_k(a_n) \quad (C-3)$$

Now, from eq.(B-16), one can get

$$P_k(a_n) = \text{Tr}[\rho_k P_n] \quad (\text{C-4})$$

where:

$$\rho_k = |\psi_k\rangle \langle \psi_k| \quad (\text{C-5})$$

is the density operator corresponding to the state  $|\psi_k\rangle$ .

Substituting eq.(C-4) into eq.(C-3), we have:

$$\begin{aligned} P(a_n) &= \sum_k P_k \text{Tr}[\rho_k P_n] \\ &= \text{Tr}[\sum_k P_k \rho_k P_n] = \text{Tr}[\rho P_n] \end{aligned} \quad (\text{C-6})$$

where we have set:

$$\rho = \sum_k P_k \rho_k \quad (\text{C-7})$$

We therefore see that the linearity of the formulae which use the density operator enables us to express all physical predictions in terms of  $\rho$ , the average of the density operators  $\rho_k$ ;  $\rho$  is, by definition, the density operator of the system.

## C.2: General properties of the density operator

The density operator:

$$\rho = \sum_k P_k \mathbf{Q}_k$$

where  $P_k$  are real, is obviously a Hermitian operator like each of  $\rho_k$ . Let us calculate the trace of  $\rho$ ; it is equal to

$$\text{Tr} \rho = \sum_k P_k \text{Tr} \mathbf{Q}_k \quad (\text{C-8})$$

From eq.(B-13), it follows that:

$$\text{Tr} \rho = \sum_k P_k = 1 \quad (\text{C-9})$$

Using eq.(C-6), we can easily generalize eq.(B-11) to statistical mixtures:

$$\langle \mathcal{A} \rangle = \text{Tr} [\rho \mathcal{A}] \quad (\text{C-10})$$

where the observable  $\mathcal{A}$  has been in the form

$$\mathcal{A} = \sum a_n P_n; P_n = \sum_i | \psi_n^i \rangle \langle \psi_n^i | \dots \dots \dots \text{Projector} \quad (\text{C-11})$$

One can easily generalize to a statistical mixture of states all the equations of §B, with the exception of (B-17). Since  $\rho$  is no longer a projector, we have, in general:

$$\rho^2 = \rho$$

(C-12)

and consequently:

$$\text{Tr} \rho^2 \leq 1$$

(C-13)

### C.3: POPULATIONS: COHERENCES

What is the physical meaning of the matrix elements in the  $\{|U_n\rangle\}$  basis?

First let us consider the diagonal element  $\rho_{nn}$ . According to eq.(C-7), we have:

$$\rho_{nn} = \sum_k P_k \langle \Psi_k | \rho | \Psi_k \rangle_{nn}$$

(C-14)

Using eq.(C-5) and introducing the component :

$$C_n = \langle U_n | \Psi_k \rangle$$

(C-15)

of  $|\Psi_k\rangle$  in the  $\{|U_n\rangle\}$  basis:

Eq.(C-14) can be rewritten as

$$\rho_{nn} = \sum_k P_k \langle U_n | \rho_k | U_n \rangle$$

$$= \sum_k P_k \langle U_n | \Psi_k \rangle \langle \Psi_k | U_n \rangle$$

$$\rho_{nn} = \sum_k P_k |C_n|^2 \quad (\text{C-16})$$

$|C_n|^2$  is a positive real number, whose physical interpretation is the following: If the state of the system is  $|\psi_k\rangle$ , it is the probability of finding, in a measurement, this system in a state  $|U_n\rangle$ . According to eq.(C-14), if we take into account the indeterminacy of the state before the measurement,  $\rho_{nn}$  represents the average probability of finding the system in the state  $|U_n\rangle$ . For this reason,  $\rho_{nn}$  is called the POPULATION of the state  $|U_n\rangle$ .

It is evident from eq.(C-16) that  $\rho_{nn}$  is a positive real number, equal to zero only if all the  $|C_n|^2$  are zero. A calculation analogous to the preceding one gives the following expression for the non-diagonal elements  $\rho_{np}$ :

$$\rho_{np} = \sum_k P_k C_n^{(k)*} C_p^{(k)} \quad (\text{C-17})$$

$C_n^{(k)*} C_p^{(k)}$  is a cross term which expresses the interference effects between the states  $|U_n\rangle$  and  $|U_p\rangle$  which can appear when the state  $|\psi_k\rangle$  is a linear superposition of these states.

According to eq.(C-17)  $\rho_{np}$  is the average of these terms taken over all the possible states of the statistical mixture. In contrast to the populations,  $\rho_{np}$  can be zero even if none of the products  $C_n^{(k)*} C_p^{(k)}$  is zero while  $\rho_{nn}$  is sum of all real positive (or zero) numbers,  $\rho_{pp}$  is a sum of real positive (or zero) numbers,  $\rho_{np}$  is a sum of complex numbers. If  $\rho_{np}$  is zero, this means that the average  $\rho_{np}$  has cancelled out any interference effects between  $|U_n\rangle$  and  $|U_p\rangle$ . On the

other hand, if  $\rho_{op}$  is different from zero, a certain coherence subsists between these states. This is why the non-diagonal elements of  $\rho$  are often called COHERENCES.

### **§D: POLARIZATION DENSITY MATRICES**

The polarization density matrix of photons  $\rho$  is a tensor of rank 2 given by the direct product (i.e. each element of one matrix is multiplied by all the elements of second matrix), denoted by the symbol  $\otimes$ , of two matrices representing the photons:

$$\rho = |\psi\rangle\langle\psi| \otimes |\psi\rangle\langle\psi| \quad (12-1)$$

#### (i) Density matrix for x-polarized photons

$$|x\rangle\langle x| \otimes |x\rangle\langle x| = \begin{pmatrix} 1 & 0 \\ 0 & 0 \end{pmatrix} \otimes \begin{pmatrix} 1 & 0 \\ 0 & 0 \end{pmatrix} \quad (12-2)$$

#### (ii) Density matrix for y-polarized photon

$$|y\rangle\langle y| \otimes |y\rangle\langle y| = \begin{pmatrix} 0 & 0 \\ 1 & 1 \end{pmatrix} \otimes \begin{pmatrix} 0 & 0 \\ 0 & 1 \end{pmatrix} \quad (12-3)$$

#### (iii) Density matrix for right circularly polarized photon

$$|R\rangle\langle R| \otimes |R\rangle\langle R| = \frac{1}{\sqrt{2}} \begin{pmatrix} 1 \\ i \end{pmatrix} \otimes \frac{1}{\sqrt{2}} \begin{pmatrix} 1 & -i \\ 1 & 1 \end{pmatrix} \quad (12-4)$$

(iv) Density matrix for left circularly polarized photons.

$$|L \otimes L\rangle = \frac{1}{\sqrt{2}} \begin{pmatrix} 1 \\ -i \end{pmatrix} \otimes \frac{1}{\sqrt{2}} \begin{pmatrix} 1 \\ -i \end{pmatrix} = \frac{1}{2} \begin{pmatrix} 1 & -i \\ -i & 1 \end{pmatrix}$$

(D-5)

(v) General density matrix for pure polarized photons

$$\rho = |\Psi\rangle \langle \Psi| = \begin{pmatrix} \Psi_x \\ \Psi_y \end{pmatrix} \langle \Psi_x^*, \Psi_y^*|$$

$$\begin{pmatrix} |\Psi_x|^2 & \Psi_x \Psi_y^* \\ \Psi_x^* \Psi_y & |\Psi_y|^2 \end{pmatrix}$$

$$\begin{pmatrix} \rho_{11} & \rho_{12} \\ \rho_{21} & \rho_{22} \end{pmatrix}$$

where,

$$\rho_{11} = |\Psi_x|^2 ; \rho_{12} = \Psi_x \Psi_y^*$$

$$\rho_{21} = \Psi_x^* \Psi_y ; \rho_{22} = |\Psi_y|^2$$

The diagonal elements of the density matrix  $\rho$  are real and they represent the intensities of the component in the x and y directions:

$$\begin{aligned} I &= \text{Tr } \rho = \rho_{11} + \rho_{22} \\ &= |\Psi_x|^2 + |\Psi_y|^2 = 1 \end{aligned}$$

$$\text{Tr } \rho = 1$$

(D-6)

Experimentally, only a linear polarizer (LP) is needed to determine  $\rho_{11}$  &  $\rho_{22}$  and the real parts of  $\rho_{12}$  &  $\rho_{21}$ . To determine the imaginary parts  $\rho_{12}$  &  $\rho_{21}$ , it is necessary to make arrangements of circular polarization, for which a retarder

QWP is also needed in addition to the LP.

#### §E: POLARIZED LIGHT AND STOKES' PARAMETERS

Polarized light serves as a tool, or probe, for evaluating the properties of matter. It has the merit of being completely convertible. It, being the simplest kind of light, is easier to deal with than the ordinary light; with it, the physical manipulation is cleaner, and the mathematical procedure for predicting the experimental outcomes are simpler. If light is man's most useful tool, polarized light is the quintessence of utility<sup>1</sup>.

The polarization state of the transmitted beam is fully characterized by elements of the photon density matrix, or equivalently, the Stokes' parameters. These parameters give the information concerning the amplitude of reflected and transmitted portions of the incident beam. They have been discussed extensively by Born and Wolf[88], Blum and Kleinpoppen(1979) and da Paixa, et al (1989). Four Stokes' parameters  $I, P_1, P_2, P_3$  are defined as follows.

$I$  is total intensity and three parameters associated with linear and circular analysis of the transmitted beam are

$$P_1 = \frac{I(0) - I(90)}{I}, \quad P_2 = \frac{I(45) - I(135)}{I}$$

$$P_3 = \frac{I(RHC) - I(LHC)}{I}$$

where

$$I = I(0) + I(90) = I(45) + I(135) = I(RHC) + I(LHC).$$

---

<sup>1</sup>Extracts from "Polarized Light" by Schurcliff, Harvard University press (1962).

## REFERENCES

- [1] Letter to H.Zangger, quoted on p. 399 of the book "Subtle is the Lord" by A. Pais Oxford: (Clarendon 1982).
- [2] A. Einstein, B. Podolsky and N. Rosen, Phys. Rev. 47, 777(1935).
- [3] W. Heisenberg, Daedalus, 87, 99(1958).
- [4] M. Born, Z. Phys., 38, 803 (1926).
- [5] N. Bohr, Quantum Theory and the Description of Nature, chap II.
- [6] J.S. Bell, Physics, 1, 195 (1964).
- [7] C.S. Wu and I. Shakhov, Phys. Rev. 77, 136 (1950).
- [8] J.A. Wheeler, Ann. N.Y. Acad. Sci. 48, 219 (1946).
- [9] C. N. Yang, Phys. Rev. 77, 242 (1949).
- [10] D. Bohm, Quantum Theory, Prentice-Hall Englewood Cliffs, New Jersey (1951).
- [11] D. Bohm and Y. Aharonov, Phys. Rev., 108, 1070 (1957).
- [12] J.F. Clauser, M.A. Horne, A. Shimony, and R.A. Holt Phys. Rev. Lett. 23, 880(1969).
- [13] J.F. Clauser, M.A. Horne Phys. Rev. D 10, 526 (1974).
- [14] T. Haji-Hassan, A.J. Duncan, W. Perrie, H.J. Beyer and H. Kleinpoppen, Phys. Lett. A, 123, 110 (1987).  
T. Haji-Hassan, A.J. Duncan, W. Perrie, H. Kleinpoppen and E. Merzbacher, Phys. Rev. Lett. 62, 237 (1989).
- [15] C. A. Kocher and E. D. Commins, Phys. Rev. Lett. 18, 575(1967).
- [16] S.J. Freedman and J.F. Clauser, Phys. Rev. Lett. 28, 938(1972).
- [17] R.A. Holt and F.M. Pipkin, Harvard Univ. preprint (1974).
- [18] J.F. Clauser, Phys. Rev. Lett. 36, 1223 (1976).
- [19] J.F. Clauser, Nuovo Cimento B. 33, 740 (1976).
- [20] A. Aspect, P. Grangier and G. Roger, Phys. Rev. Lett. 47, 460(1981).
- [21] A. Aspect, P. Grangier and G.R. Roger, Phys. Rev. Lett. 49, 91(1982).
- [22] A. Aspect, Phys. Rev. D 14, 1944 (1976).
- [23] A. Aspect, J. Dalibard and G. Roger, Phys. Rev. Lett. 49, 1804 (1982).
- [24] W. Perrie, A.J. Duncan, H.J. Beyer and H. Kleinpoppen, Phys. Rev. Lett. 54, 1790 (1985) and 54, 2647(E) 1985.

- [25] P.Grangier, G.Roger and A.Aspect, *Europhys.Lett.* 1, 173 (1986).
- [26] D.C.Burnham and D.L.Weinberg, *Phys.Rev.Lett.*, 25, 841(1970).
- [27] T.D.Newton and E.P.Wigner *Rev.Mod.Phys.*21, 400 (1949).
- [28] M.D.Reid and D.F.Walls, *Phys.Rev.A* 34, 1260 (1986).
- [29] R.Ghosh and L.Mandel, *Phys.Rev.Lett.*,59, 1903 (1987)
- [30] C.K.Hong, Z.Y.Ou and L.Mandel, *Phys.Rev.Lett.*59, 2044 (1987)
- [31] Z.Y.Ou and L.Mandel, *Phys.Rev.Lett.*61, 54 (1988).
- [32] Z.Y.Ou,E.C.Gage, B.F.Majil, And L.Mandel, *Opt.Commun.*  
69, 1(1988).
- [33] P.G.Kwiat and W.A.Vareka, *Phys.Rev.A*41, 2910 (1990)
- [34] Z.Y.Ou, X.Y.Ou, L.J.Wang, and L.Mandel, *Phys.Rev.Lett*  
65, 321(1990).
- [35] J.G.Rarity, P.R.Tapster, and E.Jakeman, *Phys.Rev.Lett.* 65,1348(1990).
- [36] P.G.Kwiat and Raymond Y Chiao, *Phys.Rev.Lett.*66, 588 (1991).
- [37] L.J.Wang, X.Y.Zou,And L.Mandel, *Phys.Rev.Lett.*66, 1111 (1991).
- [38] A.M.Steinberg, P.G.Kwiat, And R.Y.Chiao, *Phys.Rev.Lett.*  
68,2421(1992).
- [39] M.A.Horne, A.Shimony, and A.Zeilinger *Phys.Rev.Lett.*  
62,2209(1989).
- [40] I.Abram, R.K.Raj, J.I.Oudar, and G.Dolique, *Phys.Rev.Lett*  
57, 2516(1986).
- [41] C.K.Hong and L.Mandel, *Phys.Rev.A* 31, 2409(1985).
- [42] S.Friberg, C.K.Hong, and L.Mandel, *Phys.Rev.Lett.*  
59, 1903(1987).
- [43] J.D.Franson, *Phys.Rev.Lett.*62, 2205 (1989).
- [44] M.V.Berry, *Proc.Roy.Soc(London)* A392, 45 (1984).
- [45] J.R.Croca, A.Giaruccio, V.L.Lapone, and R.N.Moreira (to be published).
- [46] A.J.Duncan, A.Finch and W.Sibbet, *J.Phys.B* 23,(1990)

## REFERENCES

- [47] D.O'Connell, K.J.Kollath, A.J.Duncan, and H.Kleinpoppen, *J.Phys B*, **8**, 1. 214(1975).
- [48] E.A.Hinds, J.F.Clendinin, and R.Novick, *Phys.Rev A*, **17**, 670(1978).
- [49] H.Gould and R.Marrus, *Phys.Rev A* **28**, 2001 (1983).
- [50] H.A.Bethe and E.Salpeter, *Quantum Mechanics of One and Two Electron Atoms*(Springer-Verlag, Berlin, 1957).
- [51] G.W.F.Drake, *Phy.Rev.A* **3** 908 (1971).
- [52] G.Feinberg, and J.Saucher, *Phys.Rev Lett* **26** 681 (1971)
- [53] H.Gould, and R.Marrus, *Phys Rev A* **28** 2001 (1983)
- [54] H.Gould, D.Griener, P.Lindstorm, T.J.M.Symons and H.Crawford, *Phys.Rev Lett* **52** 180 (1984).
- [55] D.I.Lin, and G.Feinberg, *Phys Rev. A* **10** 1425 (1974) .
- [56] G.W.F.Drake, *Phys Rev* **Δ2** 2799 (1974).
- [57] R.Barbieri, and J.Saucher, *Nucl Phys.B* **134** 155 (1978) .
- [58] M.Goeppert-Meyer, *Ann.Phys Lpz* **2** 273 (1931).
- [59] G.Breit and E.Teller, *Astrophys J*, **91**, 215 (1940) .
- [60] S.Klarsfeld, *Phys Lett*, **30** A 382 (1969).
- [61] G.W.F.Drake, *Phys. Rev. A* **34** 2871 (1986)
- [62] J.H.Tung, X.M.Ye, G.J.Salamo and F.T.Chun, *Phys.Rev A* **30** 1175(1984)
- [63] A.C.Costescu, I.Brandus and N.Mezincescu, *J.Phys B* **18** L11.(1985)
- [64] H.Kruger and A.Oed, *Phys.Lett* **54** A 251 (1975).
- [65] H.Gould and R.Marrus, *Phys Rev Lett* **41** 1457 (1978).
- H.Gould and R.Marrus, *Phys Rev A* **28** 2001 (1983).
- [66] S.P.Gouldman and G.W.F.Drake, *Phys Rev A* **24** 183 (1981).

- [67]. F.A.Parpia and W.R.Johnson, Phys Rev A 26 1142 (1982).
- [68]. G.W.F.Drake and S.P.Goldman, Phys.Rev. A 23 2093 (1981).
- [69]. E.Trabert, J.H.Blanke, R.Hucke and P.H.Heckmann Phys.Scripta 31 130 (1985).
- [70].M.Bacal, A.Truc, H.J.Doucet, H.Lamain and M.Chretien, Nuc.Inst.Meth. 13 407(1974).
- [71]. M.Bacal and W.Reichelt, Rev. sci.Inst 20, 769 (1974).
- [72]. G.Spiess, A. Valence and P.Prodel Phys.Rev. A, 6, 746(1972).
- [73]. P.Prodel, F.Roussel, A.S.Schlachter, G.Spiess, Phys.Rev.A.10, 797 (1974).
- [74]. F.L.Pedrotti, Introduction to Optics, Prentice-Hall, Inc, Englewood cliffs, (1987), 476-479.
- [75]. G.K.T Conn and G.K. Eaton, J.Opt soc, Am, 44, 553 (1954).
- [76]. R.Novick, Physics of the One and Two Electron Atoms, edited by F.Bopp and H.Kleinpoppen, North Holland, Amsterdam(1969).
- [77]. G.C.King, F.H.Read and R.E.Imhof, J.Phys B 8, 665 (1975).
- [78]. B.L.Donnally, I.Clapp, W.Sawyer and M.Schultz, Phys.Rev.Lett., 12, 502,- (1974).
- [79]. H.S.W.Massey, Rep.Prog.,12, 248(1949).
- [80]. P.Pradel, F.Roussel, A.S.Schlachter and G.Spiess, Phys.Rev. A, 10, 797, (1974).
- [81]. R.D.Kaul, J.Opt.Soc Am56, 1262 (1966).
- [82]. M.Popp, G.Schäfer and E.Bodenstede, Z.Phys 240, 71(1970).
- [83]. R.A.Holt and F.M.Pipkin, Phys.Rev.A 2, 581 (1974).
- [84]. G.C.King, F.H.Read and R.E.Imhof, J.Phys B, 8, 665(1975).
- [85]. Private discussion with A.J.Duncan.
- [86]. Handbook of Optics, Walter G Driscoll, edition 1978, McGraw-Hill(1978), p10-134.
- [87]. L.J.Spitzer and J.L.Greenstein, Astrophysics J, 114, 407, (1951).
- [88]. M.Born and E.Wolf, Principles of Optics, Oxford: Pergmon (1987).